

**MEASUREMENT OF THE LONGITUDINAL DOUBLE
SPIN ASYMMETRY FOR DIJET PRODUCTION IN
POLARIZED PROTON+PROTON COLLISIONS
AT $\sqrt{S} = 510$ GEV AT STAR**

A Dissertation
Submitted to
the Temple University Graduate Board

In Partial Fulfillment
of the Requirements for the Degree
DOCTOR OF PHILOSOPHY

by
Daniel L. Olvitt, Jr.
December 2017

Examining Committee Members:

Bernd Surrow, Department of Physics, Advisory Chair
Andreas Metz, Department of Physics
Nikolaos Sparveris, Department of Physics
Rosi Reed, External Member, Lehigh University

ABSTRACT

Understanding what contributes to the intrinsic angular momentum (spin) of the proton has been a major goal of the nuclear physics community. In the 1980s, it was discovered that quarks contribute $\sim 30\%$ to the spin of the proton. This information led to a search to find other contributions to the spin of the proton. At STAR, the double spin asymmetry (A_{LL}) is measured as it is sensitive to the polarized gluon distribution ($\Delta g(x)$). The STAR 2009 inclusive jet A_{LL} at $\sqrt{s} = 200$ GeV has been incorporated into two independent global fits. These fits show for the first time a statistically significant non-zero gluon contribution to the spin of the proton in the parton momentum fraction range $x > 0.05$. Dijet A_{LL} is also measured at STAR. Dijets are advantageous since the parton momentum fraction (x) of the initial partons may be reconstructed to first order from final state measurements. In 2013 STAR collected an estimated 250 pb^{-1} of data at $\sqrt{s} = 510$ GeV. The higher center of mass energy will allow STAR to probe $\Delta g(x)$ at x values as low as ~ 0.02 . The large statistics will allow a reduction in the uncertainties. Once the data is incorporated into future global fits, it will allow for a more precise determination of $\Delta g(x)$. The 2013 dijet A_{LL} results will be presented. The results show good agreement with both global fits and previous STAR results dijet measurements.

Dedication

This thesis is dedicated to my friends and family who have supported me while at Temple University.

ACKNOWLEDGMENTS

I would first like to thank and acknowledge my advisor, Dr. Bernd Surrow. His advice, support, and help throughout the process required to complete this thesis have been invaluable. While completing my research, I learned skills related to my analysis and the life skills to help me succeed in any future career. I would like to thank him for allowing me to join his group and advising me over the years.

Bernd's research group at Temple University has been a constant source of help and support. I would like to thank the members, past and present: Dr. Matt Posik, Dr. Amilkar Quintero, Dr. Devika Gunarathne, Dr. Xuan Li, Dr. Maxence Vandenbroucke, Amani Kraishan, Nick Lukow, and Jae Nam. I would like to single out Matt, Amilkar, and Nick for their help proofreading the rough draft of this document.

Lastly, I would like to acknowledge the members of RHIC and STAR: the excellent work of the Collider-Accelerator Department at BNL for delivering the proton beams that made this research possible; the members of the STAR experiment have been essential for this work to be completed; Dr. Jerome Lauret for heading up the software and computing team at STAR. Dr. Gene Van Buren for all the calibration work that made this research possible. During my time at STAR, I was lucky enough to have help from the members of the Spin Physics Working Group. I would like to acknowledge the following individuals: Dr. Elke Aschenauer and her group for hosting me for one summer at BNL, support that helped me make progress in a short time; Dr. Kevin Adkins, with whom I worked alongside

for the BEMC tower status tables; Dr. Carl Gagliardi and Dr. Zilong Chang for all their help with the trigger algorithms for 2013 analysis; and Dr. James Drachenburg for his friendship and guidance while I was beginning my research at STAR.

CONTENTS

ABSTRACT	i
DEDICATION	ii
ACKNOWLEDGMENTS	iii
LIST OF FIGURES	viii
LIST OF TABLES	xiv
1 THESIS INTRODUCTION	1
2 THEORETICAL INTRODUCTION	4
2.1 Proton Structure	4
2.2 QCD	6
2.3 Proton Spin	7
2.4 Accessing ΔG	9
3 EXPERIMENTAL SETUP	15
3.1 RHIC	16
3.1.1 Polarized Proton Source	17
3.1.2 Beam Polarization	18
3.1.2.1 Siberian Snake Magnets	19

3.1.2.2	Polarization Measurement	20
3.2	STAR	22
3.2.1	TPC	23
3.2.2	BEMC	26
3.2.3	EEMC	27
3.2.4	Relative Luminosity Detectors	28
3.2.4.1	VPD	29
3.2.4.2	ZDC	30
4	JETS	31
4.1	Jet Definition	31
4.2	Jet Algorithm	32
4.2.1	Properties of an Ideal Jet Algorithm	32
4.2.2	Anti- k_t Jet Algorithm	33
5	2013 DATA	37
5.1	Relative Luminosity	37
5.2	Polarization	42
5.3	Triggering	43
5.3.1	STAR Online Trigger	43
5.3.2	Data Triggering	45
5.4	Selection Cuts	48
5.4.1	Jet Cuts	48
5.4.2	Dijet Cuts	50
5.5	Data QA	53
5.6	Underlying Event Correction	54
6	MONTE CARLO SIMULATION	59
6.1	Event Generation	59

6.2	Data and Embedding Comparison	63
7	ASYMMETRY FORMULAE AND SYSTEMATICS	67
7.1	Asymmetry Formulae	67
7.2	Systematics	74
7.2.1	Invariant Mass Systematics	74
7.2.1.1	Invariant Mass Shift	74
7.2.1.2	Underlying Events Systematic	75
7.2.1.3	Jet Energy Scale	76
7.2.2	Trigger and Reconstruction Bias	81
7.2.3	Scale Systematics	83
7.2.3.1	Relative Luminosity Systematic	83
7.2.3.2	Polarization Systematic	86
7.2.3.3	Underlying Events Scale Systematics	86
8	RESULTS	88
9	SUMMARY	101
	BIBLIOGRAPHY	105
	APPENDIX A ADDITIONAL EMBEDDING PLOTS	113
	APPENDIX B INVARIANT MASS DERIVATION	125
	APPENDIX C 2012 EMBEDDING RUN LIST	128
	APPENDIX D 2013 RUN LIST	130

LIST OF FIGURES

2.1	In the Baryon Octet particles with constant strangeness are on the same horizontal line. Particles with constant charge lie on the same diagonal line.	5
2.2	Particles of the Standard Model of physics.	7
2.3	Schematic of the Deep Inelastic Scattering (DIS) process.	8
2.4	Parton densities from polarized DIS and polarized SIDIS data.	10
2.5	Parton densities at $Q^2 = 10 \text{ GeV}^2$.	11
2.6	Feynman diagrams showing the gluon+gluon (left) and quark+gluon subprocesses for jet production at RHIC.	12
2.7	Parton distributions from the DSSV analysis.	13
2.8	The 2009 STAR inclusive jet A_{LL} vs. p_T compared to the previous DSSV fit, and the new DSSV fit.	14
2.9	Gluon helicity distribution for the original DSSV fit, an updated fit which does not include 2009 RHIC data (DSSV*), and the latest DSSV fit (NEW FIT).	14
3.1	Overview of the RHIC complex at BNL. The STAR experiment is located at 6 o'clock with 2 spin rotators located on each side of the experiment; also shown are the siberian snake magnets used for maintaining the beam polarization.	17

3.2	Magnet layout for an arc section of the RHIC beam pipe. The DX and D0 dipole magnets are used to steer the beams to collide at the center of the interaction point (IP).	17
3.3	Diagram of the OPPIS: 1 - high brightness proton source, 2 - focusing solenoid, 3 - pulsed hydrogen neutralization cell, 4 - super conducting solenoid (30kG), 5 - pulsed He ionizer cell, 6 - optically pumped Rb cell, 7 - sona shield, 8 - Na-jet ionizer cell.	18
3.4	Diagram showing the spin flip of the proton as beam travel through a siberian snake magnet. The blue line shows the momentum direction of the beam.	20
3.5	Experimental setup of the hydrogen gas jet target.	22
3.6	Overview of the STAR experiment.	23
3.7	The STAR TPC located around the RHIC beam pipe.	24
3.8	Schematic diagram of a TPC endcap sector. The outer sector (darker region) of padrows is more densely spaced than the inner padrows. In this figure the beam line would be to the right.	25
3.9	Side view of a BEMC module.	27
3.10	Side view of the two VPD assemblies. A one-foot ruler is shown for scale.	29
4.1	Diagram of a hard scattering producing 3 jets.	32
4.2	Diagram of a jet showing the parton, particle and detector levels.	32
4.3	Two jets formed around 2 different seed particles (left), the length of the vector is proportional to energy. The addition of a low energy (soft) particle between the two jets has caused the jets to merge and become one jet centered on the soft radiation (right).	34
4.4	The two particles on the left fail to form a seed because the energy is split among several detector towers. While on the right the same amount of energy will form a jet because the particles fall within the same tower.	35

4.5	Simulated parton level event display that used the anti- k_t jet clustering algorithm.	36
5.1	R_1 as a function of run index.	40
5.2	R_2 as a function of run index.	40
5.3	R_3 as a function of run index.	40
5.4	R_4 as a function of run index.	40
5.5	R_5 as a function of run index.	41
5.6	R_6 as a function of run index.	41
5.7	Blue beam polarization as a function of run index.	43
5.8	Yellow beam polarization as a function of run index.	43
5.9	Schematic diagram of the jet patch layout for the STAR detector.	45
5.10	Highest track p_T (in GeV) per event vs. the high p_T jet p_T (in GeV). The top left plot shows the results with no track p_T cut, top right shows if all tracks above a p_T of 30 GeV are removed, and bottom left is the result of the modified track cut.	52
5.11	Underlying off-axis cones at the same η as the jet, but $\pm\frac{\pi}{2}$ away for the in ϕ	55
5.12	The invariant mass (in GeV/c^2) for the uncorrected (black), and the underlying event corrected (blue) distributions.	58
6.1	High p_T jet p_T distribution for the data (blue) and the embedding (red). The bottom of the plot shows the ratio of (data-embedding)/embedding.	65
6.2	Invariant mass distribution for the trigger combined sample for the data (blue) and the embedding (red). The bottom of the plot shows the ratio of (data-embedding)/embedding.	66
7.1	Blue beam false asymmetry vs. the dijet invariant mass. This is fitted with a constant, which is consistent with zero, signifying that there were no major helicity dependent effects.	70

7.2	Yellow beam false asymmetry vs. the dijet invariant mass. This is fitted with a constant, which is consistent with zero, signifying that there were no major helicity dependent effects.	71
7.3	Like sign false asymmetry vs. the dijet invariant mass. This is fitted with a constant, which is consistent with zero, signifying that there were no major helicity dependent effects.	72
7.4	Unlike sign false asymmetry vs. the dijet invariant mass. This is fitted with a constant, which is consistent with zero, signifying that there were no major helicity dependent effects.	73
7.5	The above figure shows the invariant mass at the parton level vs. the invariant mass at the detector level. The black line shows a 1:1 relationship.	75
7.6	Plot of the mass difference between the corrected and uncorrected vs. the corrected invariant mass for data.	77
7.7	Plot of the mass difference between the corrected and uncorrected vs. the corrected invariant mass for embedding.	78
8.1	The invariant mass distribution separated by trigger.	91
8.2	The invariant mass distribution separated by trigger for the EEWW η dependent configuration.	92
8.3	The invariant mass distribution separated by trigger for the EW η dependent configuration.	93
8.4	Dijet double spin asymmetry (A_{LL}) for 2013 (blue) compared to the 2012 result (red).	94
8.5	Dijet double spin asymmetry (A_{LL}) for 2013 (blue) compared to the 2009 published result (grey) for the EEWW topology.	95
8.6	Dijet double spin asymmetry (A_{LL}) for 2013 (blue) compared to the 2009 published result (grey) for the EW topology.	96

8.7	The reach of x at STAR as a function of η_3 and η_4 . The black dashed line shows where the released STAR results have accessed.	100
9.1	Inclusive jet double spin asymmetry (A_{LL}) for 2013 (blue) compared to the 2012 result (red).	102
9.2	Uncertainty estimates on the polarized gluon distribution: Grey shows the uncertainty without any RHIC data, blue is the current DSSV14 fit, and orange shows the expected precision with the inclusion of all RHIC data up to 2015. To the right of the vertical dashed line shows the region constrained by data.	103
9.3	Impact of the EIC in the range $1 \times 10^{-6} < x < 1 \times 10^{-3}$ for the intrinsic quark and gluon contribution (y-axis) versus the orbital angular contribution in the range $1 \times 10^{-3} < x < 1$ (x-axis).	104
A.1	High p_T jet η distribution for the data (blue) and the embedding (red). The bottom of the plot shows the ratio of (data-embedding)/embedding.	114
A.2	High p_T jet ϕ distribution for the data (blue) and the embedding (red). The bottom of the plot shows the ratio of (data-embedding)/embedding.	115
A.3	High p_T jet R_t distribution for the data (blue) and the embedding (red). The bottom of the plot shows the ratio of (data-embedding)/embedding.	116
A.4	High p_T jet track p_T distribution for the data (blue) and the embedding (red). The bottom of the plot shows the ratio of (data-embedding)/embedding.	117
A.5	High p_T jet track η distribution for the data (blue) and the embedding (red). The bottom of the plot shows the ratio of (data-embedding)/embedding.	118
A.6	High p_T jet track ϕ distribution for the data (blue) and the embedding (red). The bottom of the plot shows the ratio of (data-embedding)/embedding.	119

A.7	High p_T jet track multiplicity distribution for the data (blue) and the embedding (red). The bottom of the plot shows the ratio of (data-embedding)/embedding.	120
A.8	High p_T jet tower E_T distribution for the data (blue) and the embedding (red). The bottom of the plot shows the ratio of (data-embedding)/embedding.	121
A.9	High p_T jet tower η distribution for the data (blue) and the embedding (red). The bottom of the plot shows the ratio of (data-embedding)/embedding. . .	122
A.10	High p_T jet tower ϕ distribution for the data (blue) and the embedding (red). The bottom of the plot shows the ratio of (data-embedding)/embedding. . .	123
A.11	High p_T jet tower multiplicity distribution for the data (blue) and the embedding (red). The bottom of the plot shows the ratio of (data-embedding)/embedding.	124

LIST OF TABLES

6.1	PYTHIA subprocesses simulated	60
6.2	Embedding Statistics	62
7.1	2013 Dijet False Asymmetries	69
7.2	2013 Invariant Mass Shifted Values (in GeV/c^2)	76
7.3	2013 Invariant Mass Shifted Values (in GeV/c^2) - EEWW	77
7.4	2013 Invariant Mass Shifted Values (in GeV/c^2) - EW	78
7.5	2013 Invariant Mass Systematic Errors (in GeV/c^2)	81
7.6	2013 Invariant Mass Systematic Errors (in GeV/c^2) - EEWW	81
7.7	2013 Invariant Mass Systematic Errors (in GeV/c^2) - EW	82
7.8	2013 Dijet A_{LL} Systematic Errors	83
7.9	2013 Dijet A_{LL} Systematic Errors - EEWW	84
7.10	2013 Dijet A_{LL} Systematic Errors - EW	85
8.1	2013 Dijet A_{LL} Values	97
8.2	2013 Dijet A_{LL} Values - EEWW	98
8.3	2013 Dijet A_{LL} Values - EW	99

CHAPTER 1

THESIS INTRODUCTION

In the simplest quark model, the proton can be thought of as being composed of 3 quarks, 2 up quarks and 1 down quark. In this model, all the properties of the proton can be explained by the three valence quarks. The charge of the proton is plus 1, where each up quark has charge $+2/3$, and the down quark has charge $-1/3$. When the charges of the quarks are summed they equal the charge of the proton. The quarks also have been assumed to be the only particles that contribute to the intrinsic angular momentum (spin) of the proton. In the 1980s this was determined to be incorrect. The European Muon Collaboration (EMC) found that the quarks only account for $\sim 30\%$ of the proton's total spin [1].

Another particle that contributes to the spin structure of the proton is the gluon. There are several ways to probe the gluon's contributions to the proton; one way is through colliding polarized proton beams. At the Relativistic Heavy Ion Collider (RHIC) proton beams collide together at center of mass energies (\sqrt{s}) of up to 510 GeV. Colliding protons at high energies, allows one to analyze the internal structure. At RHIC the gluon is accessible through double spin asymmetry (A_{LL}) measurements [2]. Proton data at $\sqrt{s} = 200$ GeV and $\sqrt{s} = 510$ GeV allow RHIC to constrain the gluon's contribution over a wide range of the initial parton momentum fraction (x). Recently, two independent theoretical fits were

released. These fits that showed for the first time a non-zero value for the gluon's contribution toward the spin of the proton [3, 4]. The 2009 STAR data at $\sqrt{s} = 200$ GeV [5], were included in these fits and had a strong impact on constraining the fit.

In 2013 the STAR experiment at RHIC collected the largest amount of proton+proton data for a single year at $\sqrt{s} = 510$ GeV. The data collected helps to constrain the gluon's contribution with unprecedented precision at lower values of x . One goal of this thesis is to provide the necessary information in order to understand the measurement of the 2013 dijet double spin asymmetry (A_{LL}). The other goal is to show how this measurement helps to constrain the polarized gluon distribution. This thesis is broken into the following chapters.

- Chapter 2 gives a brief history of the scientific discoveries involving the proton, including the current understanding that the proton is a composite particle. This chapter explains how previous results have been incorporated into global fits, which help to constrain the quark and gluon contributions.
- Chapter 3 discusses how the proton beams are produced at the Relativistic Heavy Ion Collider (RHIC) and how measurements are made using the Solenoidal Tracker at RHIC (STAR).
- Chapter 4 gives a brief discussion on the definition of jets in a hadron collider. Then the anti- k_t jet finding algorithm used for the 2013 dijet A_{LL} is discussed.
- Chapter 5 presents various topics related to the data used in this analysis. This discussion includes the beam polarization and relative luminosity measurements. Also the method used to select the data and the procedure used to obtain the final run list.
- Chapter 6 discusses the embedding procedure and illustrates the comparison between data and embedding.
- Chapter 7 discusses the calculation of the systematic errors that are relevant for the 2013 dijet A_{LL} .

- Chapter 8 shows the final results. The results are presented in both plots and detailed tables. A brief discussion of probing the polarized gluon distribution at lower x is also included.
- Chapter 9 provides a brief summary.

In addition to the eight chapters described above, there are four appendices to this document. The first is a collection of additional data and embedding comparison plots. The second is a derivation of the invariant mass formula. The remaining two appendices contain the run lists used for the 2013 asymmetry analysis.

CHAPTER 2

THEORETICAL INTRODUCTION

2.1 Proton Structure

After the discovery of the electron by J. J. Thompson in 1897, there was still an open question of what besides the electron, composed the atom [6]. Several years later, in 1904, Thompson proposed the plum pudding model of the atom. In his model, the positive charge was throughout the entirety of the atom, and the negatively charged electrons were distributed in the atoms, like the plums in plum pudding [7].

Then in 1911, Ernst Rutherford performed an experiment that led to the discovery of the proton. In his experiment, Rutherford fired a beam of alpha particles at a thin gold foil. If Thompson's plum pudding model were correct, the particle beam would pass through the foil without being deflected in any way. When the experiment was performed it was seen that most alpha particles passed through the foil while being minimally deflected, but certain alpha particles were deflected at large angles. The observation of large deflections suggested that the alpha particles were hitting an object with a large mass. This object was later found to be the proton.

Over the next few decades many other particles were discovered: the neutron in 1932 by

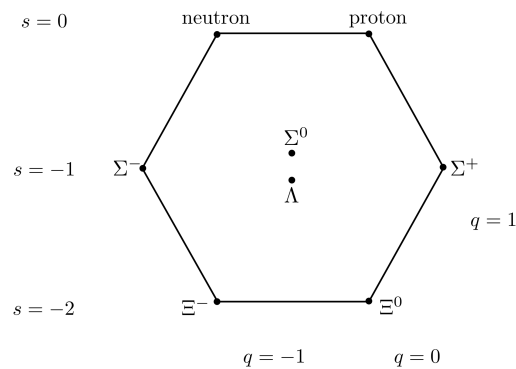


Figure 2.1: In the Baryon Octet particles with constant strangeness are on the same horizontal line. Particles with constant charge lie on the same diagonal line.

Chadwick; charged pions in 1947; and the neutral pion in 1950. A system for classifying all the newly discovered particles was proposed by Murray Gell-Mann in the 1960s. This came to known as the Eightfold Way [8]. Gell-Mann proposed a classification scheme where hadrons were classified by the particles strangeness (S) and charge in an octet. In figure 2.1, baryons with constant strangeness lie on the same horizontal, with particles that have the same charge on the same diagonal. Mesons, such as pions and kaons, can be classified in a similar manner in a meson octet.

The answer to why particles neatly fit into octets in the Eightfold Way came soon after it was introduced. Gell-Mann proposed that hadrons and mesons were composite particles; being composed of constituent particles. These particles were named quarks by Gell-Mann. Independently, Zweig proposed the same model as Gell-Mann. In both models, baryons contained three quarks (antiquarks) and mesons contained a quark-antiquark pair [9, 10]. Initially proposed were three quark flavors: up (u), down (d), and strange (s). The up quark having $S = 0$, $Q = 2/3$, down quark having $S = 0$, $Q = -1/3$, and the strange quark having $S = -1$ and $Q = -1/3$. The proton is then composed of 2 up quarks and 1 down quark. This arrangement perfectly explained the strangeness and charge of the proton. It would appear that proton containing two up quarks would violate the Pauli exclusion principle, Greenberg proposed that besides coming in different flavors, quarks had a new intrinsic

property known as color charge and contained either red, green, or blue color charge [11].

In the Quark Model the proton was made of 3 quarks being held together by the strong force, but how was the strong force mediated? Yukawa proposed in 1935 that the nucleus was bound by the exchange of a lighter particle, which came to be known as the meson [12]. Over the years many new mesons were discovered and Yukawa's theory seemed more unlikely. Ultimately, the mediator of the strong force was discovered to be the gluon; a proposal to find evidence for the gluon was suggested via hard gluon Bremsstrahlung ($e^+e^- \rightarrow q\bar{q}g$). Then in 1979, at the TASSO experiment at DESY, three jet events were discovered. These events gave clear evidence to the existence of the gluon [13].

2.2 QCD

Quantum Chromodynamics (QCD) is the theory used to describe the strong nuclear force within the Standard Model of physics. The particles of QCD are 6 quarks, with the gluon being the mediator of the strong force. A diagram showing the particles of the Standard Model can be seen in figure 2.2. Both the quarks and gluons carry color charge and are symmetric with respect to color charge described by the SU(3) Lie group [14].

There has been experimental evidence for the existence of quarks and gluons since the early 1970s, yet a free quark or gluon has never been observed in nature. This is a feature of QCD known as confinement. For example, as the distance between two quarks becomes larger, the attractive force between the quarks becomes larger. Eventually, it becomes more favorable for the quark pair to split into two quark-antiquark pairs. Another property of QCD is that the coupling strength of the gluon is inversely proportional to the energy of the gluon itself. High energy gluons couple weakly, while low energy gluons have a stronger coupling. This feature is known as asymptotic freedom [15]. The result of this is that perturbation theory is only applicable when the coupling constant is small. One way to

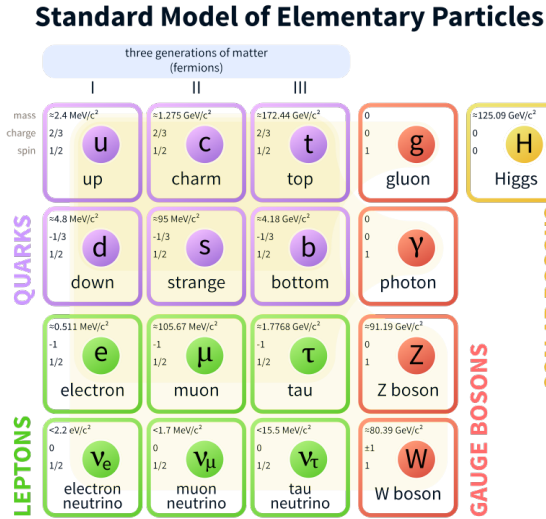


Figure 2.2: Particles of the Standard Model of physics.

overcome this problem is through factorization. Factorization is a method in which the problem is separated into a short distance piece that can be solved with perturbation theory and a long distance piece that is constrained from existing data [16].

2.3 Proton Spin

In the 1960s and 1970s, several sum rules were being tested by the polarized Deep Inelastic Scattering (DIS) data being collected. Ellis and Jaffe proposed a sum rule in 1974 that assumed that the sea quark polarization was zero and used exact SU(3) flavor symmetry [17]. The Ellis-Jaffe spin sum rule [18] (equation 2.1) could be used to decompose the spin-1/2 of the proton into contributions from the constituent quarks and gluons that composed the proton. In equation 2.1, $\Delta\Sigma$ is the contribution due to the intrinsic spin of the quarks. ΔG is the contribution from the intrinsic spin of the gluons, and L_q (L_g) is related to the orbital angular momentum from the quarks (gluons). In the simplest non-relativistic quark model, the spin of the proton is completely determined by the three valence quarks, even with the “quenching” factor applied to give a “relativistic” quark model, $\Delta\Sigma \approx 0.75$. This

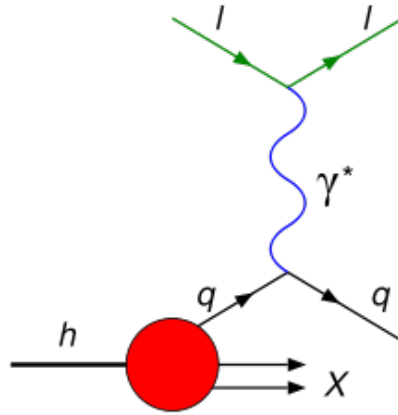


Figure 2.3: Schematic of the Deep Inelastic Scattering (DIS) process.

suggests that the intrinsic spin of the quarks is not the only contribution to the spin of the proton [19].

$$\frac{1}{2} = \frac{1}{2}\Delta\Sigma + \Delta G + L_q + L_g \quad (2.1)$$

The main tool for probing the structure of the proton has been Deep Inelastic Scattering (DIS), shown in figure 2.3. In DIS a lepton beam exchanges a virtual photon with a nearly free quark. One of the main advantages to using a lepton beam is that it has no internal structure that must be accounted for in the final state particle list. The first success of DIS was the experimental evidence of the quark at the Stanford Linear Accelerator Center (SLAC) in 1969 [20]. If the lepton beam and target were polarized, insight into the spin structure of the proton was possible. Polarized DIS (pDIS) experiments were performed by the European Muon Collaboration (EMC). The EMC collaboration measured, $\Delta\Sigma = 0.14$ [21]. This measurement was the first evidence that the simple parton model, where the spin of the proton was due to the constituent quarks, was wrong. This came to be known as the “spin crisis problem”.

2.4 Accessing ΔG

The gluon's contribution to the spin of the proton (ΔG) is accessible through the polarized gluon distribution ($\Delta g(x, Q^2)$). ΔG is simply the first moment of the polarized gluon distribution,

$$\Delta G(Q^2) = \int_0^1 \Delta g(x, Q^2) dx, \quad (2.2)$$

where Q^2 is the four momentum transfer squared.

One way to access ΔG is through polarized semi-inclusive DIS (SIDIS), where the final state hadron is identified. Unlike the polarized quark distributions, accessing the polarized gluon distribution is more difficult from SIDIS data since leptons and gluons do not interact. The gluons are only involved in some of the higher-order processes, making them less sensitive to ΔG . These processes can be found by identifying the final state hadron along with the scattered lepton. Various experiments conducted over the years have been incorporated into several global fits. In the upper right plot of figure 2.4 [22] can be seen a fit for the polarized gluon distribution. The fit shows a positive value for ΔG ; unfortunately the uncertainties are larger for ΔG compared to the polarized quark distributions. Another global fit to the data performed at next-to-leading-order (NLO) can be seen in figure 2.5 [23]. Like ref. [22], the NLO global fit shows a positive value for the polarized gluon distribution function, but with large uncertainties. Both global fits are limited in their x reach, only probing ΔG down to $x \sim 0.1$

Another way to access information on the gluon distribution is from the structure function $g_1(x, Q^2)$. The structure function contains both the quark singlet term and the gluon distribution term. These terms can be separated through Q^2 evolution, either from the

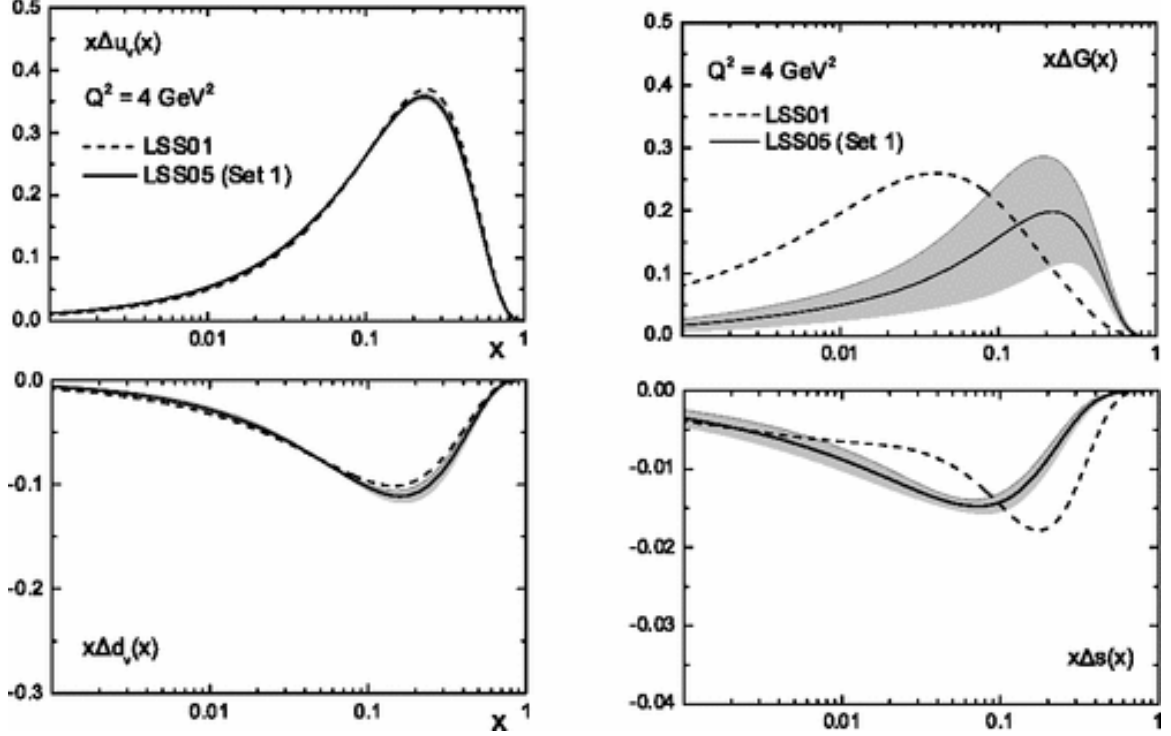


Figure 2.4: Parton densities from polarized DIS and polarized SIDIS data [22].

$\alpha_s(Q^2)$ coupling function in the coefficient terms or from the scale evolution of the parton distributions. The existing world data available before the construction of RHIC had a limited Q^2 range, which lead to large uncertainties on the extraction of ΔG [19].

At RHIC jets are produced in copious amounts at the higher center of mass energies of proton+proton collisions. These jets are directly sensitive to Δg since the subprocesses of qg and gg are dominant in the RHIC kinematic range. The Feynman diagrams showing the jet subprocesses can be seen in figure 2.6. The left side of the figure shows the gluon+gluon subprocess, while the right side shows the quark+gluon subprocess. For spin-dependent processes that take place at RHIC one measurement that can be used to access information about $\Delta g(x)$ is the double spin asymmetry (A_{LL}). A_{LL} is defined as the polarized cross section difference between parallel and anti-parallel helicity states divided by the total cross section:

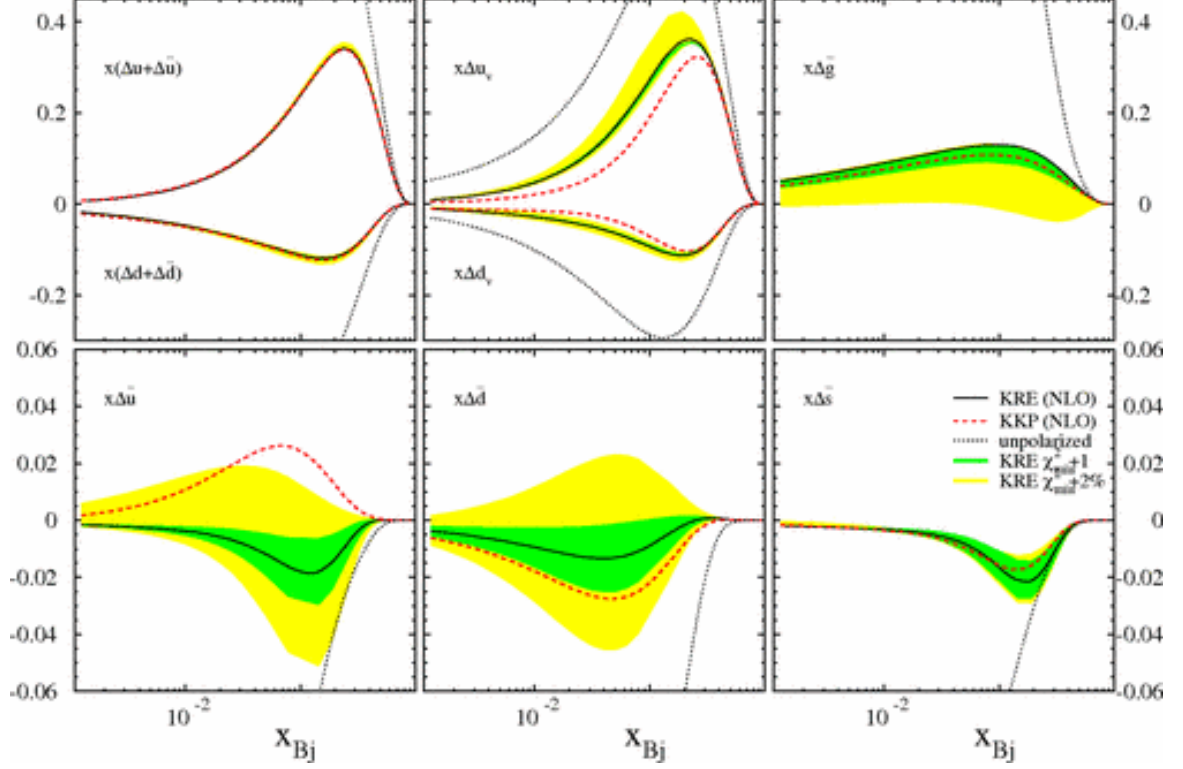


Figure 2.5: Parton densities at $Q^2 = 10 \text{ GeV}^2$ [23].

$$A_{LL} = \frac{\Delta\sigma}{\sigma} = \frac{(\sigma^{++} + \sigma^{--}) - (\sigma^{+-} + \sigma^{-+})}{(\sigma^{++} + \sigma^{--}) + (\sigma^{+-} + \sigma^{-+})} \quad (2.3)$$

The cross sections can be written in a factorized form [2],

$$A_{LL} = \sum_{ij} \frac{\int dx_1 \int dx_2 \Delta f_i(x_1, Q^2) \Delta f_j(x_2, Q^2) \Delta \hat{\sigma}^{f_1 f_2 \rightarrow f_3 f_4} \hat{a}_{LL}}{\int dx_1 \int dx_2 f_i(x_1, Q^2) f_j(x_2, Q^2) \hat{\sigma}^{f_1 f_2 \rightarrow f_3 f_4}}, \quad (2.4)$$

where i, j run over the particles involved in the jet subprocesses (quarks, gluons), and $(\Delta) f$ are the (polarized) parton distributions; $(\Delta) \hat{\sigma}^{f_1 f_2 \rightarrow f_3 f_4}$ is the (polarized) parton level cross section for incoming particles (1,2) interacting and producing outgoing particles (3,4); and \hat{a}_{LL} is the parton level double spin asymmetry.

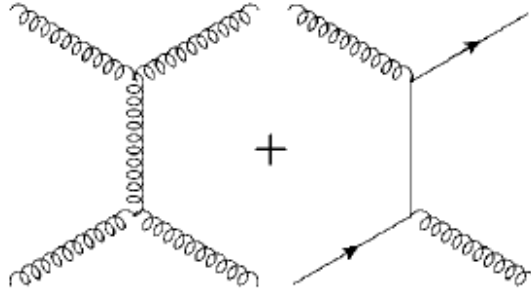


Figure 2.6: Feynman diagrams showing the gluon+gluon (left) and quark+gluon subprocesses for jet production at RHIC [2].

The unpolarized distributions are well measured and constrained from unpolarized experiments. The polarized distributions are the polarized quark and gluon distributions of interest, and the parton level cross section and double spin asymmetry can be calculated with perturbative QCD (pQCD).

One of the first global fits to include STAR data was from deFlorian, Sassot, Stratmann, and Vogelsang (DSSV). Their analysis was to NLO accuracy and was based on data from DIS and SIDIS experiments. For the first time data from polarized proton+proton collisions at RHIC [24], such as the 2005 STAR inclusive jet analysis, were included [25]. Figure 2.7 shows the polarized quark and gluon distributions compared to other fits. The DSSV group found $\Delta G = 0.013^{+0.106}_{-0.120}$ for $0.001 < x < 1$, and $\Delta\chi^2 = 1$. While the ΔG uncertainties were large compared to the polarized quark distributions, the DSSV analysis showed that using polarized proton+proton collisions was a valid method to access the polarized gluon distribution [1] and that more data would reduce the uncertainty of the fits.

A subsequent update of the original DSSV analysis was released in 2014 (DSSV14). One of the more important additions to the global fit data were the inclusion of the 2009 STAR inclusive jet A_{LL} [5]. The 2009 data used for the analysis contained an integrated luminosity of 20 pb^{-1} , which was a vast improvement from the 2005 inclusive. The 2005 jet analysis had an integrated luminosity of only 2 pb^{-1} . In figure 2.8, the 2009 inclusive jet A_{LL} is plotted in comparison to the original DSSV fit and the DSSV14 fit. The original

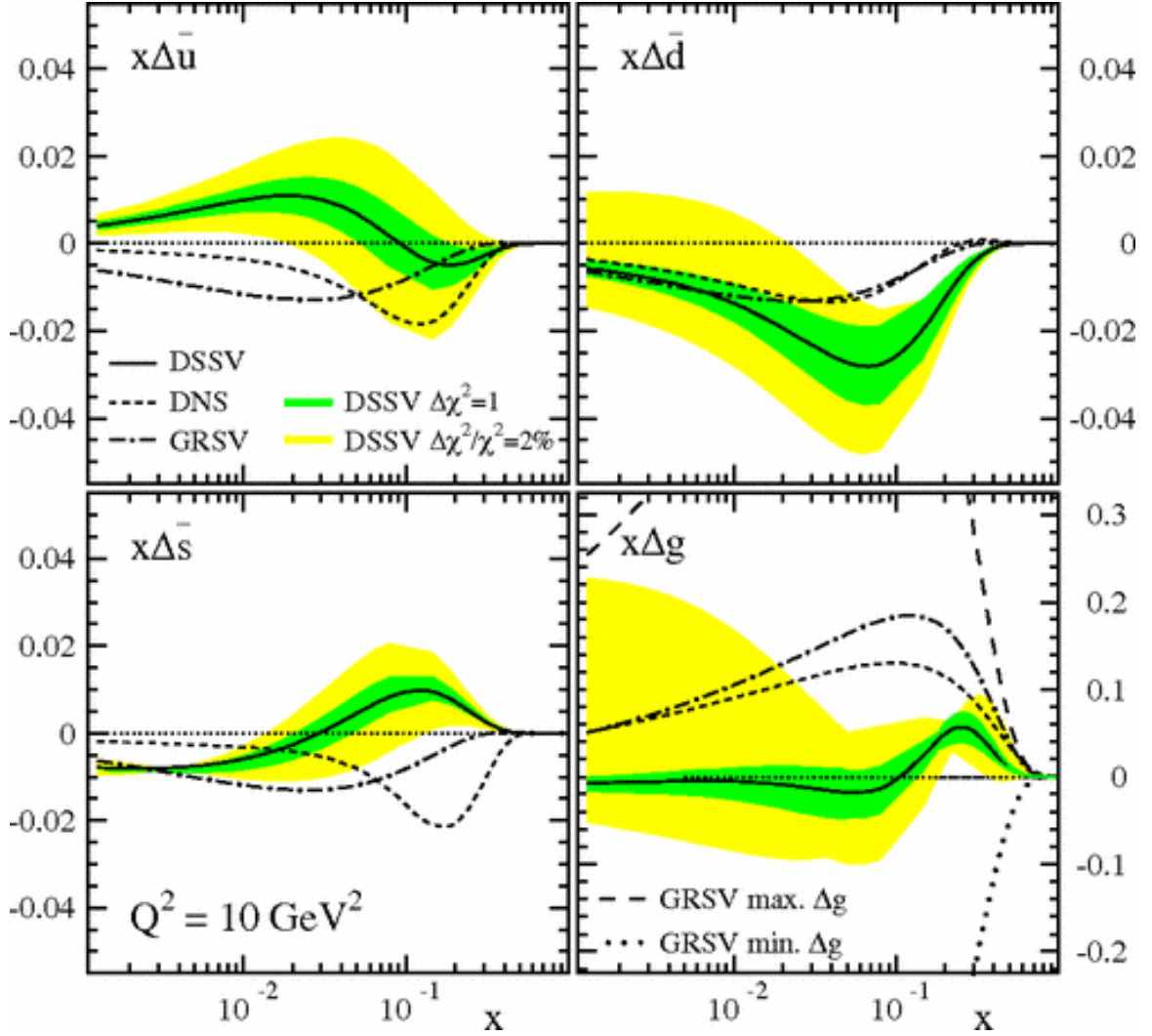


Figure 2.7: Parton Distributions Functions (PDFs) from the DSSV analysis [1].

DSSV fit sits below the 2009 inclusive jet A_{LL} , while the new fit agrees well with the data. The gluon helicity distribution is plotted in figure 2.9 for various DSSV fits. The DSSV14 analysis found $\Delta G = 0.20^{+0.06}_{-0.07}$ for $0.05 < x < 1$ [3]. Another global analysis, which also included the 2009 STAR inclusive jet A_{LL} , was performed independently by the NNPDF collaboration. The NNPDFpol1.1 analysis found $\Delta G = 0.23 \pm 0.07$ for $0.05 < x < 0.5$ [4], which is consistent with the results of DSSV14.

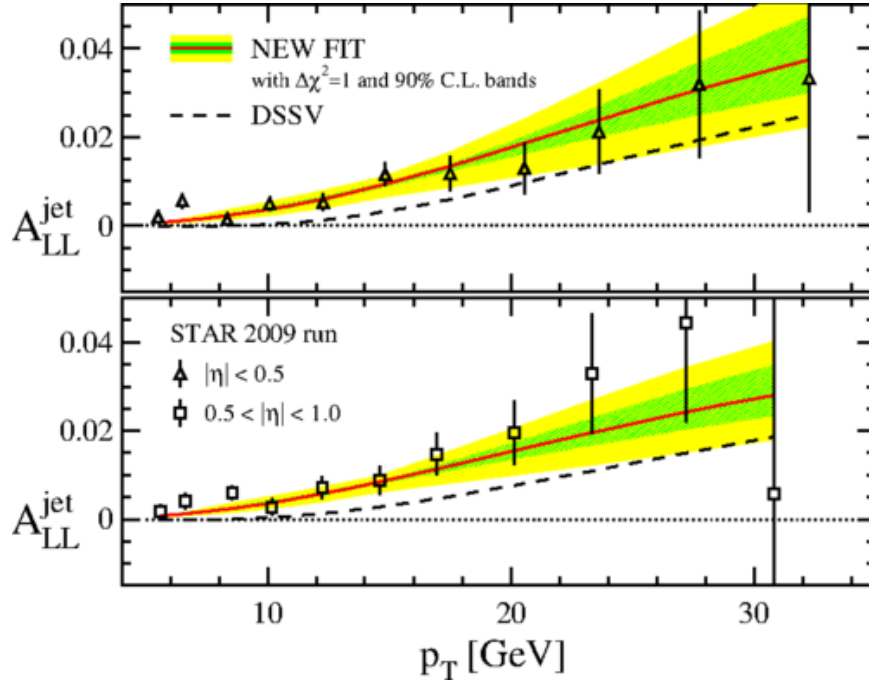


Figure 2.8: The 2009 STAR inclusive jet A_{LL}^{jet} vs. p_T compared to the previous DSSV fit, and the new DSSV fit [3].

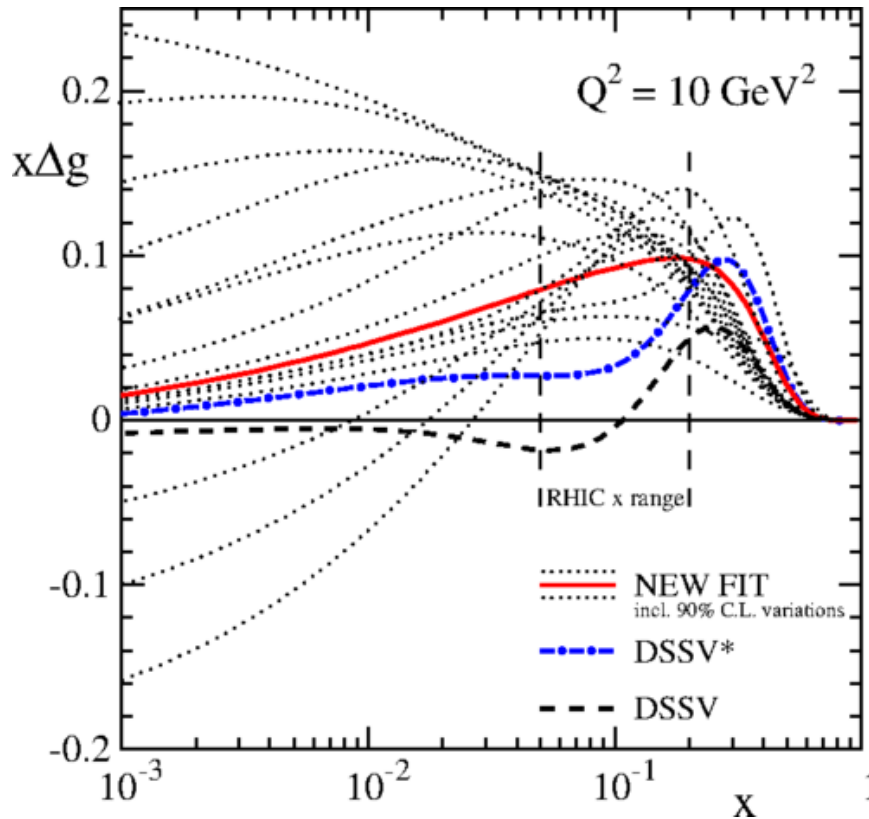


Figure 2.9: Gluon helicity distribution for the original DSSV fit, an updated fit which does not include 2009 RHIC data (DSSV*), and the latest DSSV fit (NEW FIT) [3].

CHAPTER 3

EXPERIMENTAL SETUP

Located at Brookhaven National Laboratory (BNL) on Long Island, NY, the Relativistic Heavy Ion Collider (RHIC) is the first, and the only, hadron collider capable of colliding polarized proton beams. RHIC is capable of colliding protons with a center of mass energy (\sqrt{s}) ranging from 62.4 GeV to 510 GeV, where the beams can either be polarized transversely or longitudinally with respect to the beam momentum direction. RHIC has shown performance of 50% to 60% polarization for longitudinally polarized beams. In addition to protons, RHIC collides heavy ions, such as copper, uranium, and gold ions.

The Solenoidal Tracker at RHIC (STAR) experiment was composed of various detector systems. The detectors usually measure either the energy or the momentum of outgoing particles. Other detectors were used for monitoring the luminosity of the beam and as coincidence detectors.

The first section of this chapter describes RHIC, including how the proton beams were produced and how the polarization of the beams was measured. The second half explains the relevant detectors of STAR used in the 2013 dijet A_{LL} analysis.

3.1 RHIC

The construction for RHIC was completed in 1999. The following year was the first year of operation with four active experiments: BRAHMS, PHENIX, PHOBOS, and STAR [26]. The first objective of RHIC was to study the formation and properties of the Quark-Gluon-Plasma (QGP), and for RHIC to investigate the phase transition in the QGP region. A collaboration with the RIKEN laboratory of Japan made a spin physics program possible at RHIC. The main mission of the spin physics program at RHIC was to study the spin structure of the proton.

RHIC consists of two separate beam pipes, each beam pipe with a total circumference of 3.8 kilometers. The “blue” ring runs in the clockwise direction, while the “yellow” ring runs counterclockwise. This can be seen in figure 3.1. Each beam pipe is 69 mm in diameter and consists of the following sections: six arc sections (each 356 m) and 6 insertion sections (each 277 m) [26]. The center of the insertion section is where the beams can be steered into collision with two dipole magnets (DX and D0) located approximately 10 m and 23 m from the collision point, respectively. A full layout of all magnets for an arc section can be seen in figure 3.2. The magnets in the RHIC rings are cooled to a temperature of ~ 4 K by liquid helium. [27]

When colliding protons, the beam will initially come from the Optically Pumped Polarized H^- Ion Source (OPPIS) [28]. After exiting the OPPIS, the polarized proton beam is accelerated to an energy of 200 MeV via a linear accelerator (linac). Then the beam is passed to the Booster where further acceleration takes place. Finally the beam is injected into the Alternating Gradient Synchrotron (AGS). Inside the AGS the beam is accelerated to 25 GeV. After the AGS the beam is transferred to RHIC with the AGS-to-RHIC (AtR) transfer line [29].

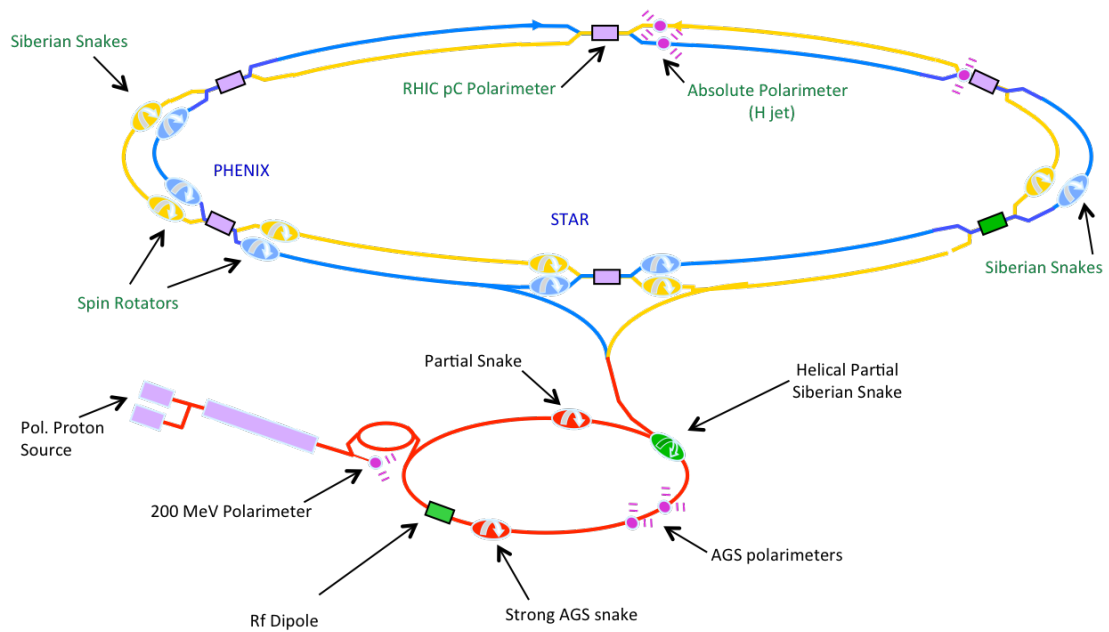


Figure 3.1: Overview of the RHIC complex at BNL. The STAR experiment is located at 6 o'clock with 2 spin rotators located on each side of the experiment; also shown are the siberian snake magnets used for maintaining the beam polarization [26].

3.1.1 Polarized Proton Source

The Optically Pumped Polarized H^- Ion Source (OPPIS) is based on the spin transfer collisions of hydrogen beams and optically pumped alkali metals. A diagram of the OPPIS can be seen in figure 3.3.

Highly polarized proton beams are produced in the following manner. After leaving

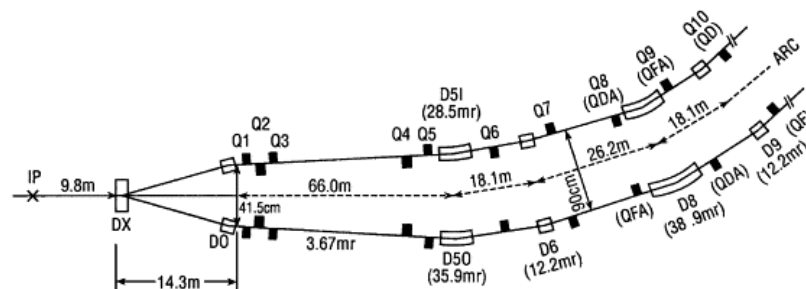


Figure 3.2: Magnet layout for an arc section of the RHIC beam pipe. The DX and D0 dipole magnets are used to steer the beams to collide at the center of the interaction point (IP) [27].

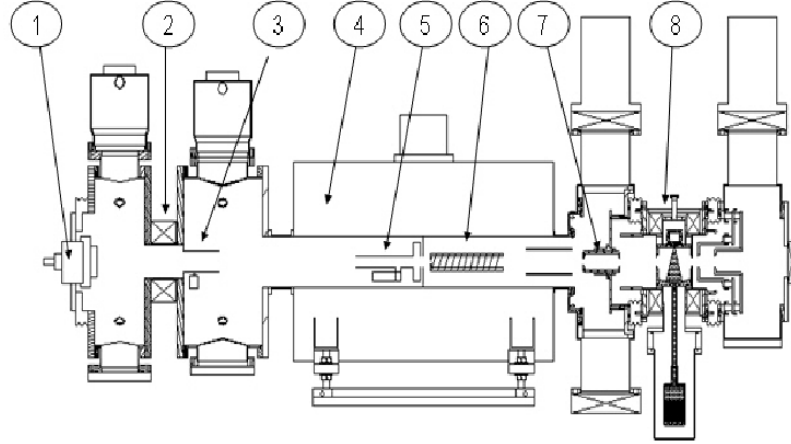


Figure 3.3: Diagram of the OPPIS: 1 - high brightness proton source, 2 - focusing solenoid, 3 - pulsed hydrogen neutralization cell, 4 - super conducting solenoid (30kG), 5 - pulsed He ionizer cell, 6 - optically pumped Rb cell, 7 - sona shield, 8 - Na-jet ionizer cell [30].

the high brightness source, the beam enters the rubidium (Rb) cell. In the Rb cell, the hydrogen in the beam interacts with the Rb atoms and acquires a polarized electron. This transforms the beam into a hydrogen beam with polarized electrons [30]. The next step is to transfer the polarization of the electrons to the protons. This is accomplished via the hyperfine interaction (sona transition), when the beam passes through a magnetic field reversal region [31]. Lastly, the polarized hydrogen atoms are negatively ionized in the sodium jet (Na-jet) ionizer cell. After being negatively ionized, the beam is accelerated to 35 keV from an applied negative bias of 32 kV.

3.1.2 Beam Polarization

The Thomas-BMT equation (equation 3.1) governs the spin direction of protons in a magnetic field [29].

$$\frac{d\vec{P}}{dt} = - \left(\frac{e}{\gamma m} \right) \left[G\gamma\vec{B}_{\perp} + (1 + G)\vec{B}_{\parallel} \right] \quad (3.1)$$

The orbital motion is described from the Lorentz force equation written in equation 3.2.

$$\frac{d\vec{v}}{dt} = - \left(\frac{e}{\gamma m} \right) \vec{B}_{\perp} \times \vec{v} \quad (3.2)$$

In equations 3.1 and 3.2, G is the anomalous magnetic moment (1.7928), and γ is the energy divided by the mass ($\gamma = E/m$). By comparing the two equations, it can be seen in a purely perpendicular magnetic field the spin of the proton will rotate by the factor $G\gamma$, which is equal to the number of spin precessions per full revolution. This term is also known as the spin tune ($\Delta\nu_{sp}$), for a RHIC energy of $\sqrt{s} = 500$ GeV the spin tune is 478 [29].

Measurements of the beam polarization are discussed in section 3.1.2.2. At RHIC this is accomplished with proton+carbon elastic scattering and a hydrogen gas jet target. The beam polarization during operation begins to decrease from depolarizing resonances, where the spin frequency is equal to the frequency of the spin perturbing magnets. These effects are overcome with the siberian snake magnets described in section 3.1.2.1.

3.1.2.1 Siberian Snake Magnets

As the beam energy increases, the depolarizing effects increase. These depolarizing resonances are caused by imperfection resonances. The condition for an imperfection resonance is when the spin tune is equal to a whole integer number. This is driven by magnet errors and misalignments. The installation of the siberian snake magnets at the 3 o'clock and 9 o'clock locations in both the blue and yellow rings of RHIC prevents these resonance conditions from being met. This is accomplished by rotating the spin of the proton by 180 degrees about the horizontal axis, as shown in figure 3.4, which produces zero net displacement of the beam. While the siberian snake magnets are in operation, the spin tune should

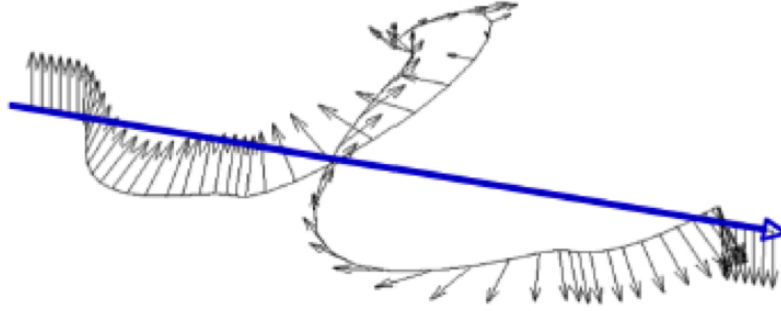


Figure 3.4: Diagram showing the spin flip of the proton as beam travel through a siberian snake magnet. The blue line shows the momentum direction of the beam [32].

always be half-integer regardless of the proton beam energy [26].

Each siberian snake magnet has an effective length of 2.4 m and contains four helical dipole magnets. Each magnet is able to produce a magnetic field of up to 4T [33]. Like the siberian snake magnets, the spin rotator magnets located on each side of STAR and PHENIX are composed of four helical magnets. The spin rotators are an essential tool for the spin program at RHIC. The spin rotator changes the orientation of the proton spin from transverse to longitudinal (with the beam direction). After the beams collide at the interaction point, the spin direction is changed from longitudinal back to transverse.

3.1.2.2 Polarization Measurement

In the Coulomb-Nuclear Interface (CNI) region where $0.005 < -t < 0.05$ (GeV/c)², $t = (P_{out} - P_{in})^2$, the transverse single spin asymmetry of elastic proton+carbon scatterings is used to monitor the beam polarization at RHIC. The advantage of using proton+carbon (pC) scattering in the CNI region to monitor polarization is that the asymmetry is significant and independent of the beam energy once above a few GeV. A non-zero asymmetry arises mainly from interference between the Coulomb flip terms, which generate the anomalous magnetic moment of the proton [34].

The polarization measurement with the pC polarimeter takes place at the 12 o'clock

interaction point at RHIC with a setup of the experiment in both the blue and yellow rings. When a polarized proton passes through an ultra-thin carbon ribbon target, carbon nuclei recoil due to CNI scattering. This will be detected in one of six silicon strip detectors. These detectors are 90 degrees with respect to the proton beam at a distance of 15 cm from the carbon ribbon target. Each silicon strip detector is divided into 12 strips parallel to the beam pipe and covers an area of $10 \times 24 \text{ mm}^2$. The readout of the detector records the energy and the time-of-flight with respect to the RHIC clock. Finally the polarization can be found using equation 3.3 [34],

$$P_{beam} = \frac{\epsilon_N}{A_N}, \quad \epsilon_N = \frac{N_L - N_R}{N_L + N_R}, \quad (3.3)$$

where $N_{L(R)}$ is the number of hits from the left (right) silicon detector and A_N is the analyzing power. The analyzing power is obtained by calibrating the pC measurements to the hydrogen gas jet absolute polarization values [35].

An absolute beam polarization measurement is possible at RHIC by using a hydrogen gas jet (h-jet) target [36]. This type of polarimetry is based on elastic proton+proton scattering in the CNI region. The polarization of the target is measured by Breit-Rabi polarimetry allows for the absolute polarization of the beam to be measured [37].

The experimental setup of the h-jet polarimeter is shown in figure 3.5. At the top is the vertically polarized atomic hydrogen beam source [37]. After exiting the 2 mm nozzle, the beam source passes through a set of sextuple magnets that focuses the beam and separates the spin. In the CNI region the recoil proton produced in elastic proton+proton scattering emerges perpendicular to the beam and is detected using silicon detectors located to the left and right of the beam at a distance of 80 cm. Each array consists of three silicon detectors segmented horizontally covering an area of $80 \times 50 \text{ mm}^2$. These detectors provide the energy, polar angle, and time of flight of the recoil proton. Finally, the polarization of

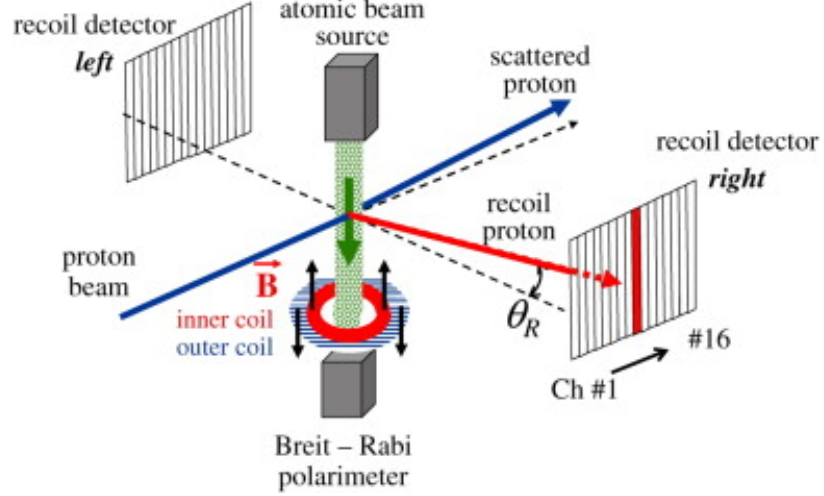


Figure 3.5: Experimental setup of the hydrogen gas jet target [37].

the target is measured by a Breit-Rabi polarimeter. With the number of hits from the left (right) detectors, the polarization of the target beam, the polarization of the proton beam can be determined with equation 3.4.

$$P_{beam} = P_{target} \frac{\epsilon_N^{beam}}{\epsilon_N^{target}} \quad (3.4)$$

3.2 STAR

The STAR experiment is a collection of detector subsystems as seen in figure 3.6. These subsystems make STAR well suited for the measurement of hadron production over the full 2π azimuthal angle, and the large acceptance allows for high precision event-by-event jet production in proton+proton collisions [38]. The main detector subsystems used in this analysis are the Time Projection Chamber (TPC) and the Barrel Electromagnetic Calorimeter (BEMC).

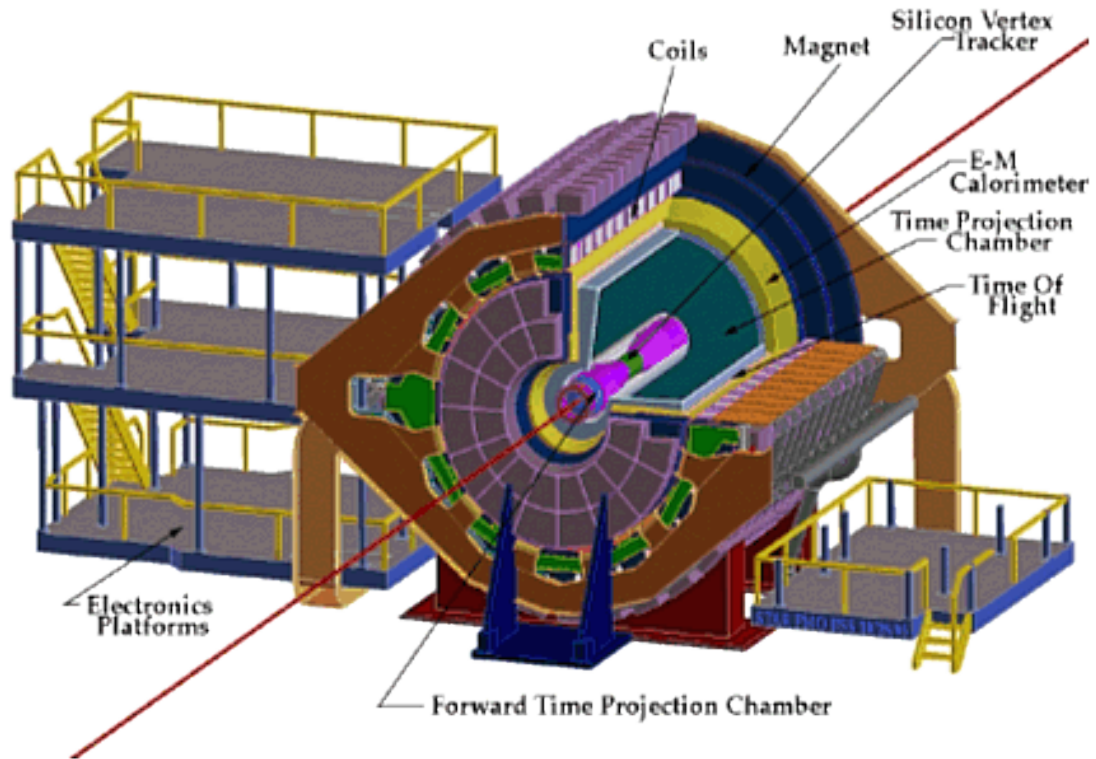


Figure 3.6: Overview of the STAR experiment [38].

3.2.1 TPC

The Time Projection Chamber (TPC) is the main tracking detector for the STAR experiment [39] shown in figure 3.7. It is used for recording the tracks, momenta of particles, and for vertex reconstruction. As can be seen in figure 3.7, the TPC is 4.2 m in length with a diameter of 4 m. The inner field cage has a radius of 50 cm and the outer field cage has a radius of 200 cm. Between the inner and outer field cages, the TPC is filled with a gas mixture of 90% argon and 10% methane (P10 gas) 2mbar above atmospheric pressure. The entire TPC sits in a 0.5 T magnetic field parallel to the beam pipe produced by a solenoidal magnet [40].

The central membrane of the TPC sits between the inner and outer field cages and acts as a cathode. The central membrane has a setting of 28 kV, while each end of the TPC acts as a grounding anode.

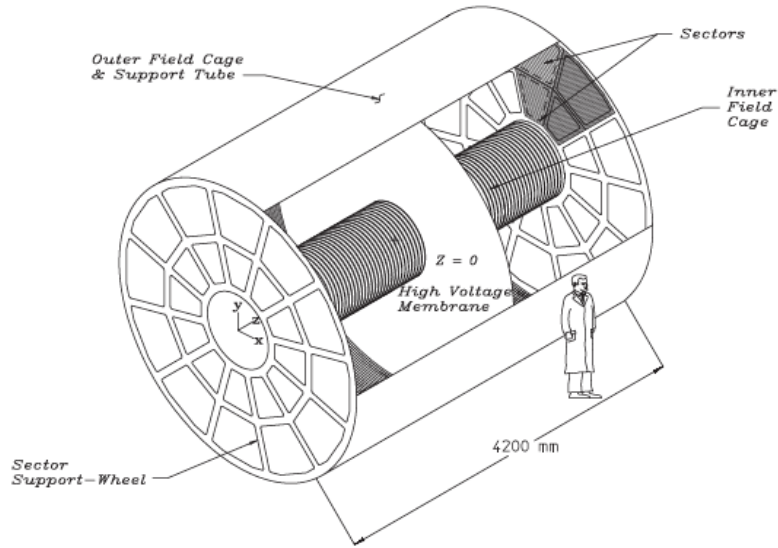


Figure 3.7: The STAR TPC located around the RHIC beam pipe [39].

When a charged particle ionizes the gas inside the TPC, it creates secondary electrons. These electrons drift to the TPC endcaps, avalanche, and are readout by multi-wire proportional chambers (MWPC). A schematic of the TPC endcap sector can be seen in figure 3.8. When the particle hits the endcap sector and avalanches, the process occurs across several padrows. A Gaussian function fits the distributions and gives the x-y position to within a few hundred microns [39]. The z position is found from the drift time of the electron and can be measured to within a few millimeters. In order to measure the z position accurately, the drift velocity of the gas must be known precisely. This is accomplished by periodically using the TPC laser system to measure the drift velocity, which can be measured to within an accuracy of approximately 0.02% [41].

Tracking software is used to fit points to form the tracks, and these points are fit with a model in order to extract the momentum of the particle. To first order, the tracks are fit with a helix. Second order effects are also considered. These include energy loss in the gas, causing the track to deviate. The tracking efficiency is dependent on the detector acceptance and the electronic detection efficiency. Acceptance inefficiencies occur for the TPC, due to the spacing between sectors and because the tracking software ignores hits in the last two

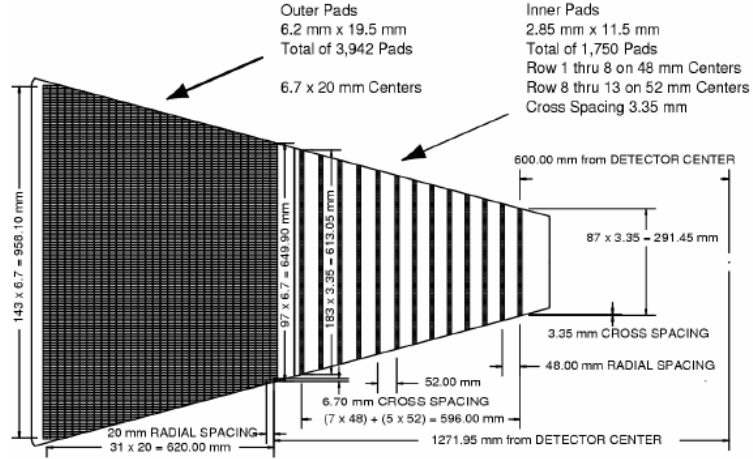


Figure 3.8: Schematic diagram of a TPC endcap sector. The outer sector (darker region) of padrows is more densely spaced than the inner padrows. In this figure the beam line would be to the right [39].

padrows. Electronic detection inefficiencies arise from dead channels and certain software cuts. The tracking efficiency for tracks above 300 GeV/c is approximately 80%, once all inefficiencies have been considered [39]. The efficiency decreases further for particles with a large pseudo-rapidity (η), defined in equation 3.5. The TPC tracking is only efficient when $|\eta| < 1.3$ [42]. Another factor to consider is the luminosity of the beam. As the luminosity increases, so will the number of events in the detector (pile-up). As the pile-up increases the tracking efficiency decreases.

$$\eta = -\ln\left(\tan\frac{\theta}{2}\right) \quad (3.5)$$

The curvature of the tracks is used to find the momentum of the particles. High momentum tracks will have a small curvature and low momentum tracks a large curvature. The TPC tracks are also used to reconstruct the event vertex. The vertex position is found by extrapolating all reconstructed tracks back to the origin. The average value of the origin is used as the z vertex position. For an event with 1000 tracks the z vertex resolution is

approximately 350 μm [39].

3.2.2 BEMC

The Barrel Electromagnetic Calorimeter (BEMC) is used for the energy measurement of particles and to trigger on high p_T processes, such as jets, dijets, and W events. The BEMC covers 60 square meters outside the STAR TPC, but the BEMC is still inside the aluminum coil of the STAR magnet. Since it surrounds the entire TPC, it has full azimuthal coverage and covers an η range from negative one to positive one ($|\eta| \leq 1$). The BEMC is constructed from lead and plastic scintillator material, which at $\eta = 0$ is 20 radiation lengths thick ($20X_0$). This gives the BEMC an energy resolution of $\delta E/E = 14\%/\sqrt{E} + 1.5\%$. The BEMC also contains a Shower Maximum Detector (SMD), which allows for precise spatial resolution. This is required for π^0 reconstruction and direct identification of gammas and electrons. The SMD sits at a depth of approximately $5.6 X_0$ at $\eta = 0$ [43].

The BEMC was constructed from a modular design; in total there are 120 modules, each containing 40 towers for a total of 4,800 towers. A schematic diagram of a module including the location of the SMD can be seen in figure 3.9. Each module is 26 cm wide, 293 cm long, and has an active depth of 23.5 cm. This allows each module to cover 6° in ϕ and a $\Delta\eta$ of 1 [43].

Each module consists of 21 scintillating layers; the first two layers closest to the TPC are 6 mm thick while all other layers are 5 mm thick. The scintillating layers are alternated with 5 millimeter thick layers of lead. Each layer of plastic scintillator is formed into a “megatile” with 40 optically isolated “tiles” in each layer. The fibers from the “tiles” are routed outside the STAR magnet to decoder boxes. Inside the decoder boxes light from the fibers is merged into a single photo-multiplier tube (PMT) for readout [43].

The electronics included for the BEMC are the readout, trigger, high voltage controls for the PMTs, data acquisition (DAQ), and slow controls. Level 0 events are selected

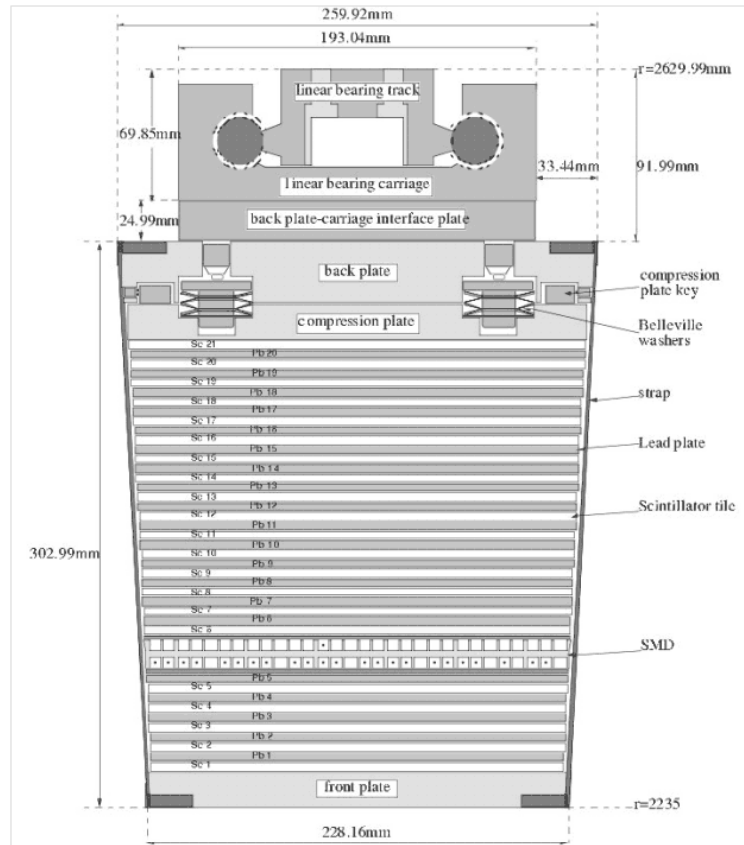


Figure 3.9: Side view of a BEMC module [43].

for processing. This is to ensure operation with little to no dead time. Because of the speed and bandwidth requirements, the BEMC relies on trigger primitives. There are two different types of trigger primitives; first there are 300 trigger patches. Each trigger patch covers a 0.2×0.2 patch in η, ϕ space. The second trigger primitive is composed of 300 tower patches; the largest tower (0.05×0.05 in η, ϕ) signal in a 0.2×0.2 patch in η, ϕ space is selected for triggering. These trigger primitives make decisions based on the amount of energy deposited into the towers [43].

3.2.3 EEMC

Located on the west side of the STAR experiment, the Endcap Electromagnetic Calorimeter (EEMC) was constructed using similar methods and technology as the BEMC. It ex-

tends the measurement of electromagnetic showers in the pseudo-rapidity range of $1.086 < \eta < 2$. The small gap in η coverage is to allow for services to exit the solenoid. The EEMC consists of 720 towers; each tower has a $\Delta\phi = 0.1$ and $0.057 \leq \Delta\eta \leq 0.099$, depending on tower location. The towers are constructed with 23 layers of lead/stainless and 24 layers of plastic scintillator. The towers are designed to measure energies as low as 0.2 GeV to as high as 150 GeV, with an energy resolution of $\delta E/E = 16\%/\sqrt{E} + 2\%$. This allows the EEMC to perform jet reconstruction with an uncertainty of 0.1 in jet η and jet ϕ [44].

Like the BEMC, the EEMC also contains a SMD located 5 radiation lengths deep. In the forward region, the fine granularity is used to distinguish single photon events from two photon pairs coming from π^0 and η^0 decays. The electronics are similar to those in the BEMC, allowing jets to be triggered by large E_T and large particle multiplicity [44].

3.2.4 Relative Luminosity Detectors

The relative luminosity is the ratio of helicity counts at RHIC. In total there are 6 relative luminosity values determined, a complete list of the definitions is given in section 5.1. For the 2013 data collection period, the Vertex Position Detectors (VPD) and Zero Degree Calorimeters (ZDC) were used in the determination of the relative luminosities. Both detectors were quick readout “scalar” detectors. The scalar board read out the bunch crossing number and the bits for an east, west, or a coincidence hit. A bit is triggered if a hit on the detector is above a predetermined ADC threshold [45].

For the ZDC, the scalar board reads out bits for east, west, coincidence hits, and the bunch crossing number. For the 2013 data collection period, the VPD only read out scalar bits for east and west hits. A coincidence state was found for the VPD when both the east and west scalar bits were readout for the same bunch crossing.

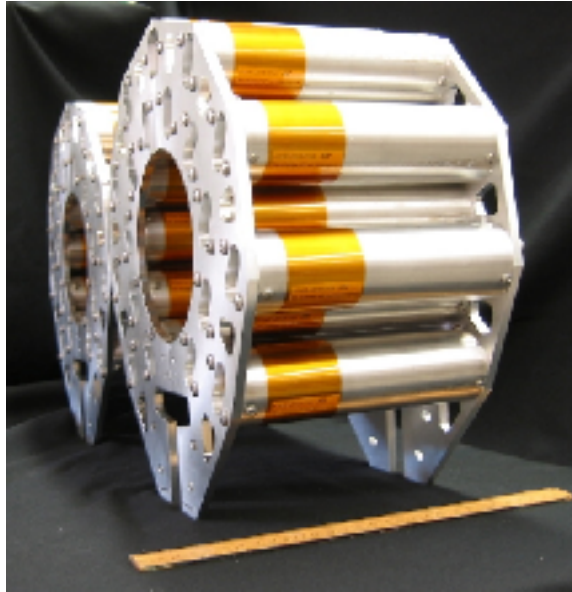


Figure 3.10: Side view of the two VPD assemblies. A one foot ruler is shown for scale [46].

3.2.4.1 VPD

The Vertex Position Detectors (VPD) are located on both sides of STAR, approximately 5.7 m from the center [46]. They are capable of measuring a large particle multiplicity. This is essential for event triggering and detecting the primary vertex. Due to the VPD's effectiveness in vertex triggering, it is one of the primary inputs for a minimum bias (minbias) trigger at STAR.

The VPD on each side of STAR consist of an assembly of 19 detectors, which are made of lead converter. After the lead converter is a one centimeter thick layer of fast scintillator, which is readout by PMTs. The 19 detectors are each housed in an aluminum cylinder with an outer diameter of two inches and a wall thickness of 0.049 inches. The assembly of detectors is held together by a 3/8 inch thick front and back cap seen in figure 3.10.

3.2.4.2 ZDC

The Zero Degree Calorimeters (ZDC) are hadron calorimeters located on both sides of the STAR, similar to the VPD [47]. Unlike the VPDs, the ZDCs are located farther down the beam pipe, past the DX dipole magnets. As a result of their location the ZDC is intended to measure the energy and multiplicity of neutrons for a narrow cone of $\theta \leq 4$ mrad. Since the ZDCs are located on each side of the STAR detector, they can be used as a coincidence detector, making the ZDCs ideal for selecting minbias events and monitoring the luminosity of the beams.

CHAPTER 4

JETS

4.1 Jet Definition

Imagine a $qg \rightarrow qg$ hard scattering as shown in figure 4.1. The outgoing quark hadronizes into a collimated stream of particles, which is called a jet. The same outgoing quark can also radiate a gluon before it hadronizes into a jet. The radiated gluon also hadronizes into a jet. Lastly, the outgoing gluon hadronizes and forms a jet. Jets can be described at three different levels: detector, particle, and parton levels. Parton level jets are composed of the outgoing partons (quarks, gluons) from a $2 \rightarrow 2$ hard scattering. The particle level consists mostly of hadrons, but may contain other particles, such as photons. The hadrons contained in the particle level jets are from hadronization or particle decay of the outgoing parton. Finally, there is the detector level, which consists of the measured energy deposition from the BEMC or EEMC, as well as the tracking information from the TPC. A diagram of the three levels can be seen in figure 4.2.

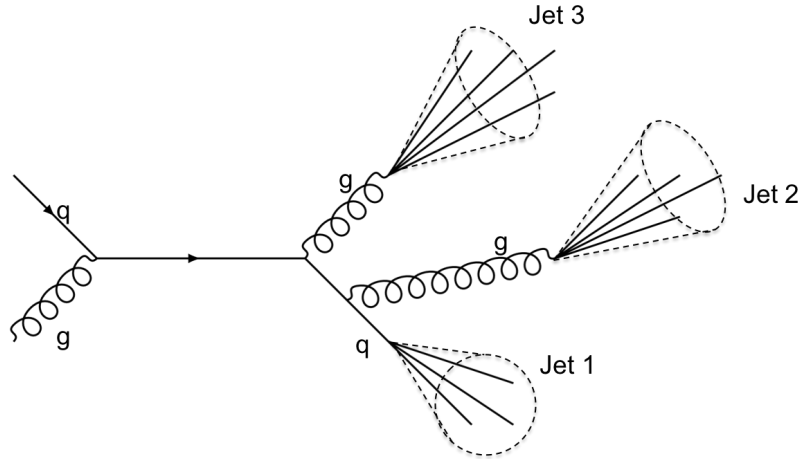


Figure 4.1: Diagram of a hard scattering producing 3 jets.

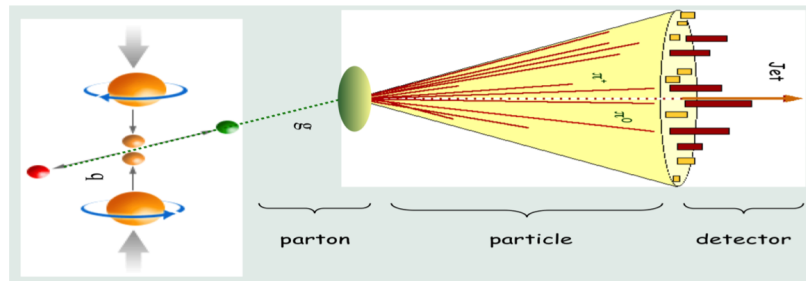


Figure 4.2: Diagram of a jet showing the parton, particle and detector levels.

4.2 Jet Algorithm

This section focuses on the properties that are important for consideration in a jet finding algorithm. The jet reconstruction algorithm that is currently being used at STAR, the anti- k_t jet clustering algorithm is described.

4.2.1 Properties of an Ideal Jet Algorithm

A jet is a stream of particles, which is found using a computer algorithm; the properties of that algorithm determine how effectively a jet is found as well as the properties of the jet. The algorithm should be infrared and collinear (IRC) safe. IRC safe jets are high energy (hard) jets that are not modified by low energy (soft) particles, such as underlying events

(UE), which may come from Multiple-Parton-Interaction (MPI). MPI is an independent $2 \rightarrow 2$ scattering. Another source of soft energy is from detector pile-up. Detector independence is important for a jet algorithm. The granularity of the detector should not affect jet finding and reconstruction. Lastly, the algorithm should work equally well at the detector, particle, and parton levels [48].

Infrared (IR) safe jets are jets that are insensitive to soft radiation. The effects of soft radiation are shown in figure 4.3. In this example the algorithm looks at an entity with a minimum amount of energy, known as a seed. On the left side of figure 4.3, two different jets have been found, each centered around a different seed. In the right plot the effect of soft particle radiation has caused the two jets merge into a single jet. The soft particle has been used as a seed, and as a result the two entities that were seeds without the soft particle have been included in the jet centered around the soft particle [48].

The next factor to consider is the collinear safety of the algorithm. Collinear safety is the condition that the entities used in the jet finding algorithm are aligned with a detector element. Ideally, the algorithm would be insensitive to the difference between a particle that deposits its energy in a single tower and a particle that deposits its energy across several towers. An example of this effect is shown in figure 4.4. On the left side of this figure, the two particles fail to form a jet. The energy is spread out among several towers none, of which is large enough to be used as a seed. On the right side of figure 4.4, the entities are within a single tower. As a result, this tower meets the energy requirement and is able to form a jet [48].

4.2.2 Anti- k_t Jet Algorithm

Beginning with the 2009 proton+proton data set, the STAR experiment adopted the anti- k_t algorithm. The first published result using this algorithm was the 2009 inclusive jet A_{LL} at $\sqrt{s} = 200$ GeV [49]. The anti- k_t algorithm is a sequential recombination algorithm.

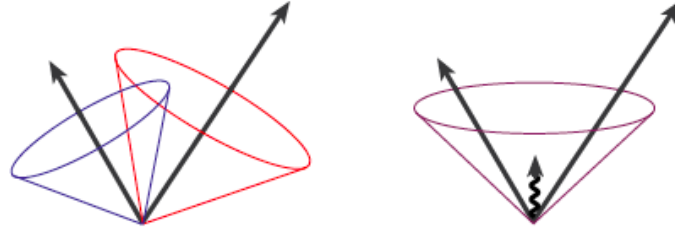


Figure 4.3: Two jets formed around 2 different seed particles (left), the length of the vector is proportional to energy. The addition of a low energy (soft) particle between the two jets has caused the jets to merge and become one jet centered on the soft radiation (right) [48].

Like all sequential recombination algorithms, the anti- k_t algorithm is IRC-safe, with jet boundaries that are insensitive to low energy particles. For the anti- k_t algorithm there are two important distances to define: the distance between entities (tracks or towers), shown in equation 4.1, and the distance between the entity and the beam, shown in equation 4.2 [50].

$$d_{ij} = \min(k_{ti}^{2p}, k_{tj}^{2p}) \frac{\Delta_{ij}^2}{R^2}, \quad (4.1)$$

$$d_{iB} = k_{ti}^{2p}, \quad (4.2)$$

$\Delta_{ij}^2 = (y_i - y_j)^2 + (\phi_i - \phi_j)^2$, and y is the rapidity and ϕ is the azimuthal angle, k_t is the transverse momentum of the entity, and R is the jet radius.

The inclusive clustering identifies the smallest distance (d_{iB} or d_{ij}). If the smallest distance is between the entities (d_{ij}), then entities i and j are combined. If the smallest distance is between entity i and the beam, then entity i is labeled as a jet. This procedure is repeated until the list of entities is exhausted [50].

Consider an event with a hard particle and many soft particles. The distance between

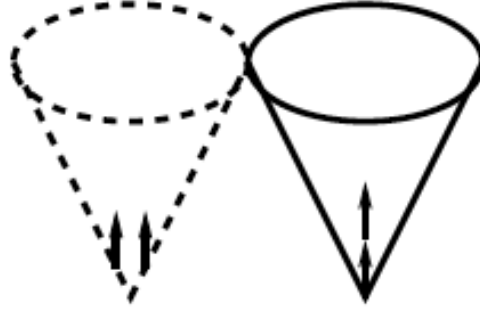


Figure 4.4: The two particles on the left fail to form a seed because the energy is split among several detector towers. While on the right the same amount of energy will form a jet because the particles fall within the same tower [48].

a hard particle (1) and soft particle (i) is d_{1i} . Now consider a pair of soft particles at the same distance as the hard and soft particle, for the anti- k_T algorithm d_{ij} is much larger than d_{1i} . This feature results in soft particles tending to cluster together, whereas hard particles do not. A hard particle with no other hard particles within a distance of two times the jet radius (R) becomes a conical jet centered around the hard particle [50].

If there are two jets around two different hard particles within a distance of $2R$, both of the jets cannot be conical. If jet 1 has a k_T much greater than jet 2, jet 1 forms a conical jet, while jet 2 forms but the overlapping region with jet 1 is removed and jet 2 is partly conical. This can be clearly seen in figure 4.5. At $y = 2$, $\phi = 5$, the hard jet (green) formed a conical jet, and the softer jet (pink) formed a partially conical jet, missing the part that overlapped with the harder (green) jet. In instances where the k_T of the two jets is comparable, the area is divided between both jets by a straight line at the center on the overlap region. For the anti- k_T algorithm, high energy particles are the only particles that influence the shape of the jet [50].

As mentioned in section 4.2.1, it is ideal for the jet clustering algorithm to be indepen-

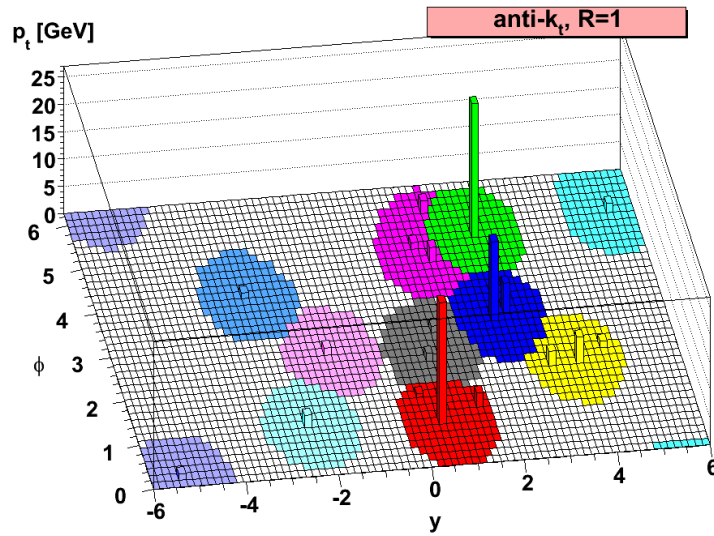


Figure 4.5: Simulated parton level event display that used the anti- k_t jet clustering algorithm [50].

dent of luminosity. Take for example a set of jets, J , that are the result of the entire jet finding procedure being performed for a given event. Now take that same event and add soft radiation coming from underlying events and pile-up due to increased luminosity, and perform jet reconstruction obtaining a set of jets, \bar{J} . For the anti- k_t algorithm, the affect of soft energy is suppressed by the transverse momentum of the jet. In other algorithms, the suppression is proportional to the amount of soft energy added to the event. This feature makes the anti- k_t jet clustering algorithm less susceptible to soft radiation from increased luminosity [50].

CHAPTER 5

2013 DATA

This chapter discusses the data being used for the 2013 dijet analysis. In order to calculate the double spin asymmetry, the polarization and relative luminosity values are required. The definition of the relative luminosity is given in section 5.1 and of polarization is given in 5.2. The definition of how an event was triggered and the selection cuts applied at the jet and dijet level are explained. Generation of the final run list is described. Finally, the underlying event subtraction scheme is presented in the last section of this chapter.

5.1 Relative Luminosity

The detectors used to calculate the relative luminosity at STAR were the Vertex Position Detectors (VPD) and Zero Degree Calorimeters (ZDC), which were explained in more detail in sections 3.2.4.1 and 3.2.4.2, respectively. The relative luminosity was used in the calculation of the double spin asymmetry as well as the false asymmetries. If the uncertainty in the calculation of relative luminosity was not to affect the uncertainty of the asymmetries, a high-rate process was needed. This was to ensure that the statistical uncertainty of the relative luminosity was negligible [51]. The calculation of the systematic

error due to the relative luminosity was discussed in detail in section 7.2.3.1, though it was important that the systematic error due to the relative luminosity be subdominant compared to the other systematic errors. The 6 relative luminosities used to calculate the asymmetries for the 2013 dijet analysis are shown below:

$$R_1 = \frac{N^{++} + N^{-+}}{N^{+-} + N^{--}}, \quad (5.1)$$

$$R_2 = \frac{N^{++} + N^{+-}}{N^{-+} + N^{--}}, \quad (5.2)$$

$$R_3 = \frac{N^{++} + N^{--}}{N^{+-} + N^{-+}}, \quad (5.3)$$

$$R_4 = \frac{N^{++}}{N^{--}}, \quad (5.4)$$

$$R_5 = \frac{N^{-+}}{N^{--}}, \quad (5.5)$$

$$R_6 = \frac{N^{+-}}{N^{--}}, \quad (5.6)$$

where N refers to the number of hits detected for each helicity state. The first superscript refers to the helicity of the blue beam and the second to the helicity of the yellow beam.

In order to sample different helicity collisions for the 2013 data, four different spin patterns were chosen for the beams. The four patterns are shown below:

- Pattern 1: + + - - + + - -
- Pattern 2: - - + + - - + +
- Pattern 3: + + - - - - + +
- Pattern 4: - - + + + + - -

Different combinations of the beam spin patterns were chosen to reduce the effect of an unequal number of spin pattern collisions. The complete list of spin pattern collisions is listed below. The first pattern listed is for the blue beam, and the second listed refers to the yellow beam.

- Pattern 1 * Pattern 3
- Pattern 1 * Pattern 4
- Pattern 2 * Pattern 3
- Pattern 2 * Pattern 4
- Pattern 3 * Pattern 1
- Pattern 3 * Pattern 2
- Pattern 4 * Pattern 1
- Pattern 4 * Pattern 2

The 6 relative luminosities are plotted as a function of run index in figures 5.1 to 5.6. Ideally, the relative luminosity would equal 1. It is rare for this to happen for a given run. The value for the 6 relative luminosities tends to fluctuate around 1, with an average close to 1.

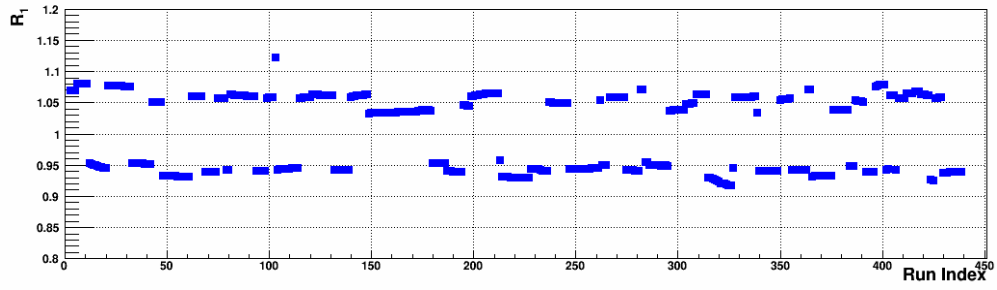


Figure 5.1: R_1 as a function of run index.

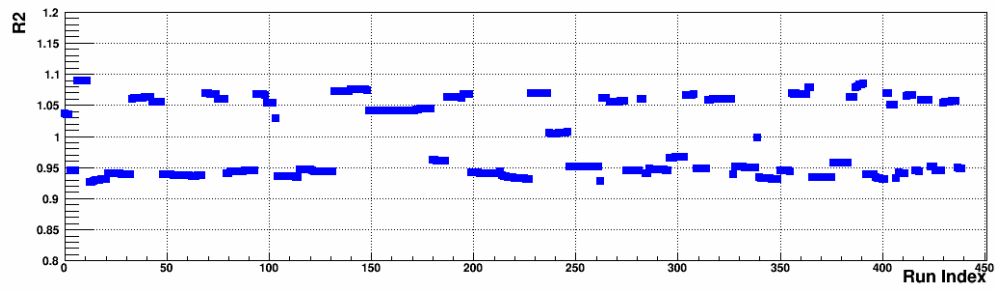


Figure 5.2: R_2 as a function of run index.

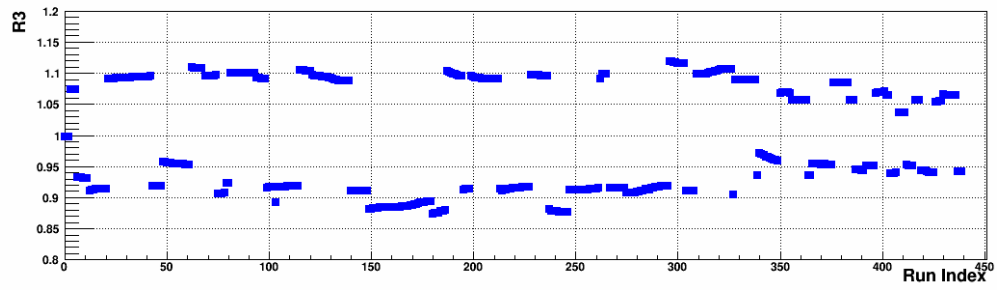


Figure 5.3: R_3 as a function of run index.

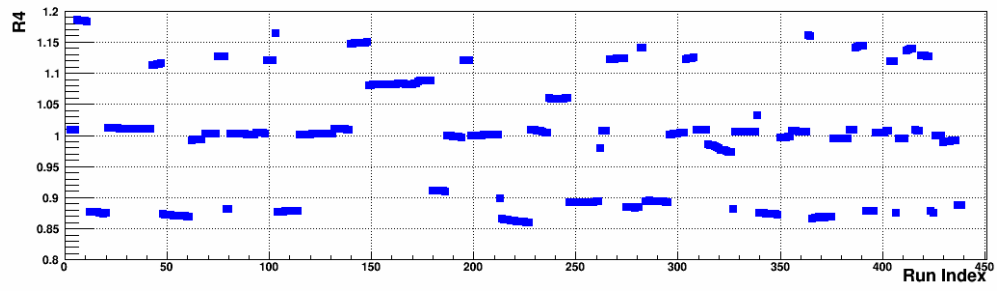


Figure 5.4: R_4 as a function of run index.

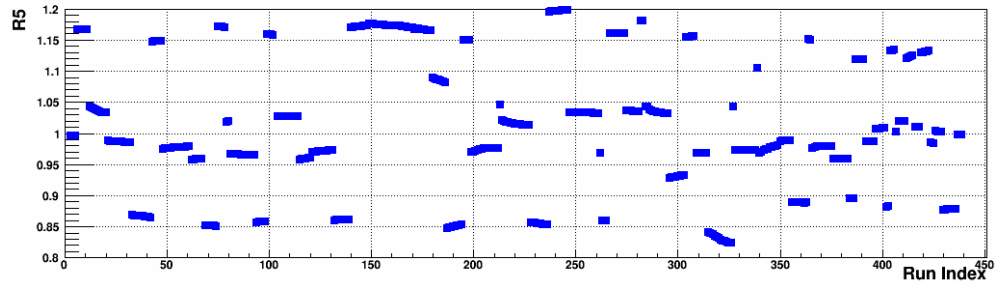


Figure 5.5: R_5 as a function of run index.

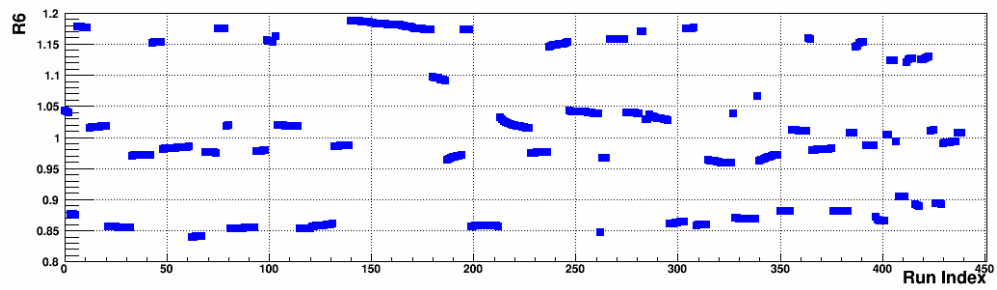


Figure 5.6: R_6 as a function of run index.

5.2 Polarization

The polarization at RHIC is measured by the proton+carbon (pC) polarimeter [34] and the hydrogen gas jet (h-jet) target [36, 37]. For more information about the details of the polarimeters, see section 3.1.2.2. The pC polarimeter is used to monitor the polarization of the beam over time for a given fill at RHIC. There are two pC polarimeters per beam, allowing for independent crosschecks of all measurements [35]. The h-jet polarimeter is used to measure the absolute polarization of the beams. If the absolute polarization is measured at the beginning of a fill, the polarization decay is monitored during the fill. The polarization can be found for a given run using an exponential fit to the polarization information as seen in equation 5.7,

$$P(t) = P_0 e^{-\frac{dP}{dt} * t}, \quad (5.7)$$

P_0 is the initial polarization measurements at the beginning of a fill, dP/dt is the polarization decay term (defined as positive), and t represents time.

With the initial polarization value at the beginning of a fill along with the decay constant, it is possible to calculate the polarization for every run in a given fill. The blue beam polarization is shown in figure 5.7, and the yellow beam polarization is shown in figure 5.8. For both beams the polarization is between 40% and 70%, with an average polarization of 53% for the blue beam and 54% for the yellow beam.

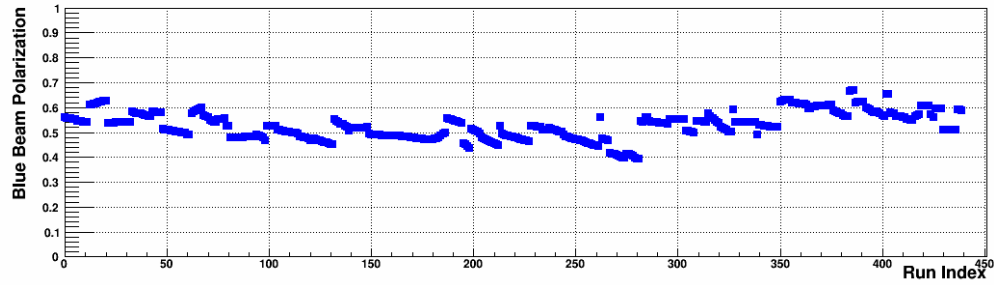


Figure 5.7: Blue beam polarization as a function of run index.

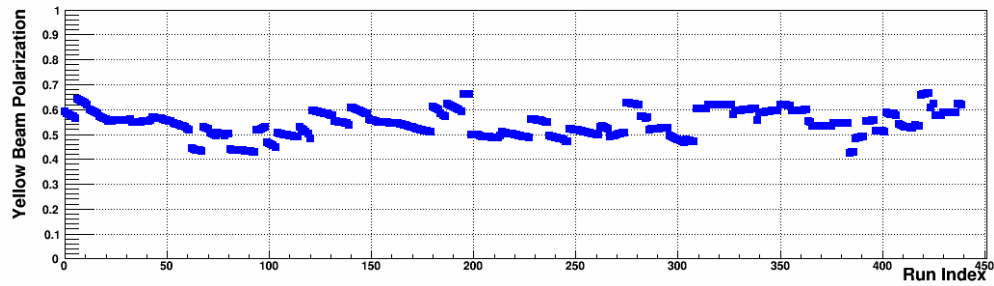


Figure 5.8: Yellow beam polarization as a function of run index.

5.3 Triggering

5.3.1 STAR Online Trigger

For the 2013 dijet analysis the triggers used are listed below:

- JP0
- JP0DiJet
- JP1
- JP1DiJet
- JP2

The detector used for jet triggering was the Barrel Electromagnetic Calorimeter (BEMC) [43]. The BEMC consists of 4,800 towers, each tower covering a region 0.05 in η and 0.05

in ϕ . A trigger patch is 4x4 towers grouped together, covering a region of 0.2x0.2 in η, ϕ space. These trigger patches get combined into the jet patches shown in figure 5.9. A jet patch was defined as an area in the BEMC that covers a region approximately 1x1 in η, ϕ space [52].

The BEMC was divided into a total of 18 jet patches. There were 6 jet patches that cover a range of $-1 < \eta < 0$, and another 6 jet patches that cover from $0 < \eta < 1$. The last 6 jet patches cover the η range spanning from -0.6 to 0.4. Each set of 6 jet patches covers the full azimuthal angle (ϕ) from 0 to 2π [52].

Each jet patch was compared to a 9-bit ADC threshold. The requirement for a trigger to be satisfied was that the jet patch must have an ADC value larger than the trigger threshold. The following ADC trigger thresholds (and corresponding energies) were used for the 2013 dijet analysis.

- JP2: 66 (14.4 GeV)
- JP1: 43 (9.0 GeV)
- JP0: 34 (6.8 GeV)
- dijet: 17 (2.8 GeV)

The conversion from ADC values to energy values in GeV was accomplished with equation 5.8. It should be noted that equation 5.8 will return a number only accurate to three significant figures at most.

$$GeV = (ADC - 5) * 0.236 \tag{5.8}$$

The last step for the online triggering was to form the JP0DiJet and JP1DiJet triggers. These triggers were a combination of two jet patches, where one jet patch was above the

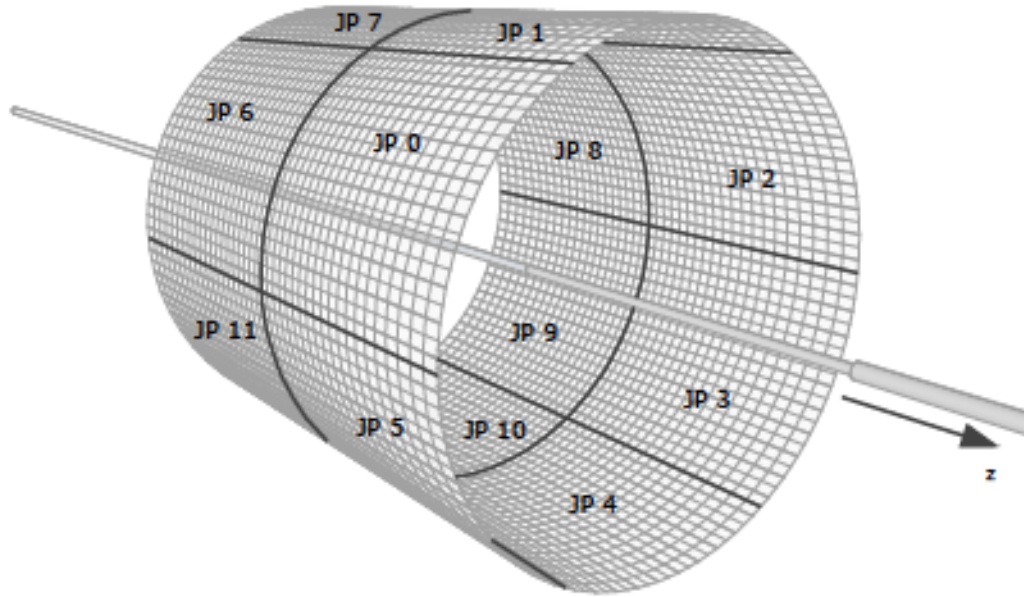


Figure 5.9: Schematic diagram of the jet patch layout for the STAR detector [53].

JP0 or JP1 threshold, and a second jet patch was above the dijet threshold. For an event to be classified as a JP1DiJet trigger the following must occur. A barrel jet patch must be above the JP1 threshold. Then a second jet patch, either in the barrel or the endcap, must be above the dijet threshold. If these two jet patches were not adjacent in ϕ , the event was classified as a JP1DiJet trigger. The same logic was used for the JP0DiJet trigger with the appropriate thresholds [52].

5.3.2 Data Triggering

To calculate the dijet double spin asymmetry, the number of dijets for each helicity state must be counted and classified by trigger. While collecting data in 2013, many of the triggers were pre-scaled in order to accommodate the limited bandwidth of the data acquisition system. The JP0 trigger was the most pre-scaled, followed in decreasing order by the JP1, JP0DiJet, and JP1DiJet trigger. The JP2 trigger was not pre-scaled in 2013. The first step

in the triggering algorithm was to check if a given trigger had “fired”, that is, the ADC requirements had been met for a jet patch. If the trigger had fired the “didFire” flag would return true; otherwise it would return a value of false. STAR also used an offline trigger emulator that mimicked the online trigger system. The trigger emulator classified events in simulation using the same logic as the data triggering, but without pre-scale factors. If the trigger emulator had fired a trigger it would return “shouldFire” true; if no trigger has fired the trigger emulator would return “shouldFire” false.

The goal of triggering was to match the data sample to the embedding Monte Carlo sample. In the Monte Carlo simulation, actual data events were embedded into the simulation in order to reflect the background conditions present during data collection. Agreement between the data and embedding was crucial for reliable calculation of the systematic errors discussed in section 7.2.

There were many advantages for using the trigger emulator when selecting data events. Requiring a data event to return “didFire” and “shouldFire” true helps to keep the event selection the same in both data and embedding. Requiring the “shouldFire” in data also had the advantage of removing bad towers that were flagged in the offline tower quality assurance (QA). This was particularly important since the “QAed” tower list was used in the embedding. Any tower given a bad “flag” was not simulated. The trigger emulator will also classify events that failed a trigger in data because of the pre-scale, but not in the embedding. For example, an event may satisfy all the conditions for a JP1 trigger, but because of the pre-scale, this event would be demoted to a JP0 trigger in the data; in the trigger emulator however, it would be classified as a JP1 trigger. This allows one to promote triggers from a heavily pre-scaled trigger to a less heavily pre-scaled trigger.

For a given event there were at least 2 reconstructed jets that would be classified in the following manner. Each jet was classified to a trigger individually. The DiJet triggers were the exception. By definition they require two jets for the trigger to fire. For a jet to be

classified, it must meet three requirements based on the jet energy, the ADC value of the jet patch, and whether the jet is geometrically matched to the “fired” jet patch. Geometric matching was the requirement that the jet must be a certain distance from the jet patch center. If the jet has an η, ϕ value within ± 0.6 of the jet patch center, it was considered geometrically matched to the jet patch. The first trigger to be classified is the JP2 trigger, since it was not pre-scaled. The JP2 trigger has an energy threshold of 14.4 GeV. This limit was raised to 15 GeV, to account for trigger turn-on effects. If a jet has at least 15 GeV of energy, and the jet is geometrically matched to a jet patch that had an ADC value greater than 66, the jet was defined as a JP2 jet. The next trigger considered was the JP1DiJet trigger, which required conditions to be placed on two jets. Jet 1 had a minimum jet energy of 9.5 GeV and be geometrically matched to a barrel jet patch with an ADC value greater than 43. Jet 2 was also geometrically matched to a barrel jet patch with an ADC value greater than 17 and minimum jet energy of 5 GeV. The last condition was that the jet patches for jet 1 and jet 2 were not allowed to be adjacent in ϕ . If a jet had failed to be classified as JP2 or JP1DiJet, it was next checked against the conditions for the JP0DiJet trigger. These conditions were the same as the JP1DiJet trigger, except the conditions for jet 1 were a minimum energy of 7.3 GeV and geometric matched to a barrel jet patch with an ADC value greater than 34. The last two triggers considered were the JP1 and JP0 triggers, respectively. They had the same requirements as the JP2 trigger, but lower energy and ADC thresholds. For the JP1 trigger the minimum energy and ADC values were 9.5 GeV and 43. For the JP0 trigger the minimum energy and ADC values were 7.3 GeV and 34.

The last step was to determine the final trigger pre-scale values. Since events were promoted from a higher pre-scaled trigger to a lower pre-scaled trigger, this would effectively lower the pre-scale value of the triggers. The JP1DiJet trigger had events promoted from the JP0DiJet trigger as well as the JP1 and JP0 triggers. Each trigger effect on the pre-scale is calculated in equation 5.9. The final pre-scale value for the JP1DiJet trigger is given by

the last line in equation 5.9.

$$\begin{aligned}
\frac{1}{PS^{JP1DiJet}_{modA}} &= \frac{1}{PS^{JP1DiJet}} + \left(1 - \frac{1}{PS^{JP1DiJet}}\right) * \left(\frac{1}{PS^{JP0DiJet}}\right) \\
\frac{1}{PS^{JP1DiJet}_{modB}} &= \frac{1}{PS^{JP1DiJet}} + \left(1 - \frac{1}{PS^{JP1DiJet}}\right) * \left(\frac{1}{PS^{JP1}}\right) \\
\frac{1}{PS^{JP1DiJet}} &= \frac{1}{PS^{JP1DiJet}} + \left(1 - \frac{1}{PS^{JP1DiJet}}\right) * \left(\frac{1}{PS^{JP0}}\right)
\end{aligned} \tag{5.9}$$

The JP0DiJet and JP1 triggers only received promotion events from the JP0 trigger. The equations for their final pre-scale values are shown in equation 5.10 for the JP0DiJet trigger and equation 5.11 for the JP1 trigger.

$$\frac{1}{PS^{JP0DiJet}} = \frac{1}{PS^{JP0DiJet}} + \left(1 - \frac{1}{PS^{JP0DiJet}}\right) * \left(\frac{1}{PS^{JP0}}\right) \tag{5.10}$$

$$\frac{1}{PS^{JP1}} = \frac{1}{PS^{JP1}} + \left(1 - \frac{1}{PS^{JP1}}\right) * \left(\frac{1}{PS^{JP0}}\right) \tag{5.11}$$

5.4 Selection Cuts

5.4.1 Jet Cuts

When using the STAR jet reconstruction software, energy deposited into the BEMC towers, EEMC towers, and charged tracks from the TPC were used as input parameters. In addition to satisfying the requirements of the anti- k_T algorithm, the individual tracks and towers had to meet certain conditions. The towers (BEMC and EEMC) were required to pass the followings cuts.

- Tower status = 1

- $\text{ADC} - \text{pedestal} > 4$
- $\text{ADC} - \text{pedestal} > 3 \cdot \text{RMS}$
- $E_T > 0.2 \text{ GeV}$

The cuts above were to ensure the tower was appropriate for use in the jet finding algorithm. After the data had been collected, a QA of all towers was performed; a good tower was given status equal to 1. The ADC minus pedestal cuts were meant to ensure that the signal was coming from an actual particle depositing energy into the tower. The last cut was meant to remove any low energy towers. In addition to the cuts listed above, a tower energy correction scheme was applied. If a track was matched to a tower, the energy of the track was subtracted from the energy of the tower. If the energy of the tower was negative after subtraction of the track energy, the energy value of the tower was set to zero.

The tracks from the TPC that were used in the jet finding algorithm must satisfy the following cuts.

- Number of hit points ≥ 12
- $\frac{\text{number of hit points}}{\text{number of possible hits}} \geq 0.51$
- Track DCA $\leq 3 \text{ cm}$
- $0.2 \text{ GeV} \leq \text{Track } p_T \leq 200 \text{ GeV}$
- $-2.5 \leq \eta \leq 2.5$
- Track last point hit radius $> 125 \text{ cm}$
- Track p_T dependent DCA cut

The first two cuts were to ensure a quality track and to minimize the reconstruction of fragmented tracks. Requiring the last hit to be at a radius of 125 cm or larger ensures the track had at least one hit in an outer TPC sector as well as hits in the inner TPC. The track p_T cut was to remove any low energy tracks, and the η cut removes most of the tracks that fall

outside the TPC. The distance of closest approach (DCA) cut removed any event where the track associated with the primary vertex was more than 3 cm from that vertex. The primary vertex was the position where the two protons collide. In 2013, STAR used the pile-up-proof-vertex (PPV) finder to find the primary vertex [54]. PPV assigned a negative rank to vertices that were likely due to pile-up. Primary vertices were assigned a positive rank with the best vertex having the highest rank. PPV can find more than one primary vertex, but the best primary vertex with the highest rank was selected. The track p_T dependent DCA cut was defined in equation 5.12. This placed different DCA cuts on the data depending on the track p_T . This cut was implemented to further reduce pile-up events.

$$DCA < \begin{cases} 2 \text{ cm, track } p_T < 0.5 \text{ GeV} \\ -1.0 \text{ cm/GeV} * \text{track } p_T + 2.5 \text{ cm, } 0.5 \text{ GeV} < \text{track } p_T < 1.5 \text{ GeV} \\ 1 \text{ cm, track } p_T > 1.5 \text{ GeV} \end{cases} \quad (5.12)$$

5.4.2 Dijet Cuts

After the triggering of the jets was completed, the events must pass a series of selection cuts to be included in the analysis. First only events from the primary vertex with a positive rank were used. In addition to requiring the vertex to have a positive rank, the following cuts were applied in the order listed below:

1. $|z\text{-vertex}| < 90 \text{ cm}$
2. Asymmetric p_T cut of 8 GeV and 6 GeV
3. Neutral energy fraction (R_t) < 0.95 (for both jets)
4. $-0.9 \leq \eta_{physics} \leq 0.9$ (for both jets)

5. $-0.7 \leq \eta_{detector} \leq 0.9$ (for both jets)

6. $\cos(\Delta\phi) < -0.5$

7. Modified track p_T cut

Detector η was the position where the particle hits the detector, while physics η was the angle of particle with respect to the event vertex. For an event at the center of STAR ($z = 0$) physics η and detector η were the same, while the neutral energy fraction was defined in equation 5.13.

$$R_t = \frac{tower E_T}{tower E_T + track p_T} \quad (5.13)$$

The first cut was a requirement that the event vertex be near the center of the detector. Ideally when two protons collide, this would happen in the center of the STAR detector ($z = 0$). At $\sqrt{s} = 510$ GeV, the spread of the z -vertex was approximately 45 cm, so many of the “real” events had a vertex passing cut 1. The asymmetric p_T cut was applied in order for the results to be compared to theoretical predictions. When calculating theoretical dijet results, an asymmetric p_T cut is required. Typically the lower energy jet is 2 GeV below the higher energy jet. For the 2013 dijet analysis the leading jet p_T had to be above 8 GeV, and the lower energy jet was required to have energy of at least 6 GeV. The neutral energy fraction cut was to ensure that not all the energy of the jet was from neutral particles; neutral jets were more likely to originate from non-collision backgrounds. The η cuts required that the analysis was performed at mid-rapidity. Dijet events from partonic hard scattering were expected to be back-to-back. Cut 6 required the jets to be separated in the azimuthal angle (ϕ) by at least 120 degrees.

The modified track p_T cut was applied to account for the lack of reliability of the TPC for tracks with a transverse momentum of 30 GeV or larger. If either jet contained a track

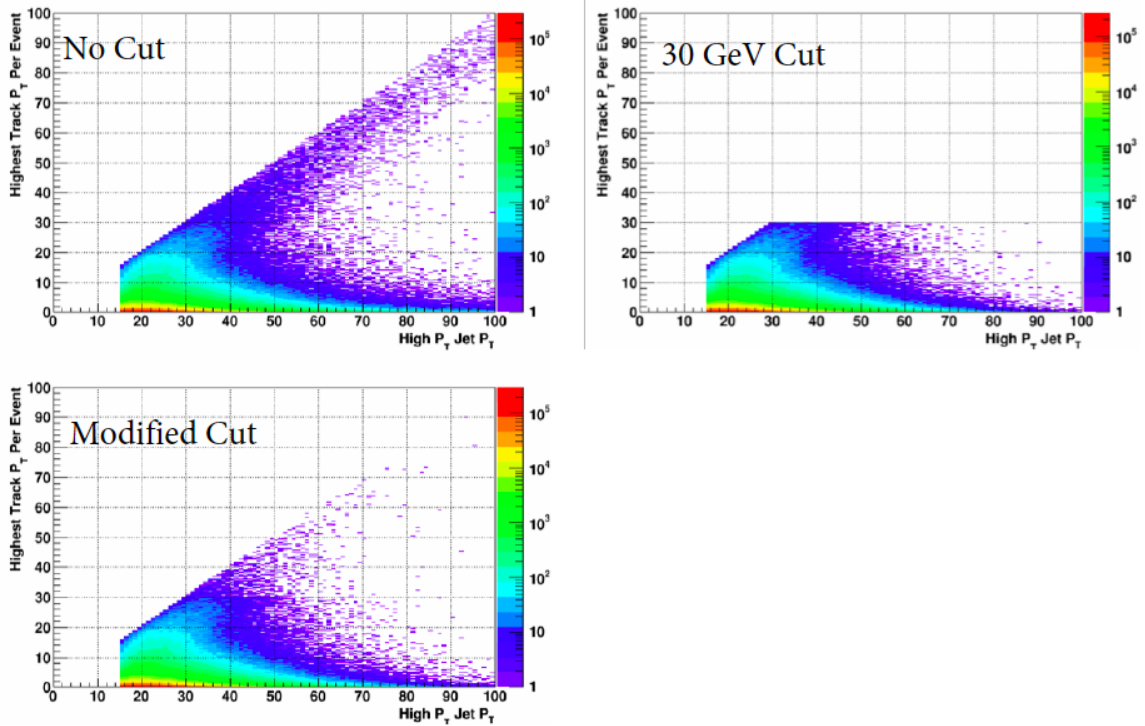


Figure 5.10: Highest track p_T (in GeV) per event vs. the high p_T jet p_T (in GeV). The top left plot shows the results with no track p_T cut, top right shows if all tracks above a p_T of 30 GeV are removed, and bottom left is the result of the modified track cut.

with a p_T of at least 30 GeV, this event was included if the ratio of the high p_T jet over the low p_T jet was between two-thirds and three-halves; otherwise the event was removed from the analysis. If no track p_T cut was applied, there were many events where energy of the jet was dominated by a single track. In an inclusive jet analysis, typically all jets with a track p_T higher than 30 GeV were removed. For the dijet analysis this would remove many real events with a high track p_T in a jet, but where the jet p_T was not dominated by a single track. The application of the modified track p_T cut removed many of the events in which a jet was dominated by a single high p_T track. The results of the above mentioned track p_T cuts can be seen in figure 5.10.

For the dijet embedding there were additional cuts placed on the events. The difference of z-vertex between the detector and particle level should be 2 cm or less. In addition the jets were required to be “matched” in η , ϕ space. Each event had to pass the condition

listed in equation 5.14 (“*det*” refers to the detector level and “*part*” to the particle [parton] level). Lastly, the 2 detector level jets could not be matched to the same (parton) level jet.

$$R = \sqrt{(\eta_{det} - \eta_{part})^2 + (\phi_{det} - \phi_{part})^2} \leq 0.5 \quad (5.14)$$

5.5 Data QA

In order to select good runs for the analysis, data QA was performed. The QA was performed for the full 2013 data set. For the initial results only a portion of the data was used, as explained in section 6.2. The barrel adjacent jet patch (BAJP) trigger was used in the QA procedure, but the trigger was ultimately dropped from the analysis.

The initial list was comprised of runs that had a relative luminosity value. Relative luminosity was one of the quantities in the asymmetry formula (section 7.1). Any run without a relative luminosity was not valid for this analysis. After the relative luminosity was determined, the next quantity investigated was the run time. If a run was not longer than 3 minutes, it was removed from the analysis. When starting a run at STAR, many files had to be loaded and the trigger pre-scales calculated. During these steps, there could be errors that resulted in the run not being usable, and usually these errors occurred in the first 3 minutes of the run.

The next step was to plot the average of a given quantity versus run index. A run was “flagged” if the average value for a given quantity fell outside of the range of the average value for the full data set of plus or minus 3 times the RMS. If a given run had 5 of 6 triggers flagged, it was removed. If 4 of 6 triggers were flagged, the run was removed only if the JP0 trigger was not one of the four bad triggers. This was done since the JP0 trigger was the highest pre-scaled trigger and had larger statistical fluctuations.

For the dijet 2013 analysis the following quantities were evaluated for both jets in the dijet pair in the QA procedure: Jet p_T , jet η , jet ϕ , and jet R_t . Track and tower quantities, such as their multiplicities was also included in the QA procedure. The track multiplicity showed a slope structure, which was due to the luminosity decreasing during a fill. As the luminosity decreased, the TPC tracking efficiency increased, and as a result the average number of tracks increased. The energy, η , and ϕ for the track and tower for both jets was also QAed as well. Finally the x, y, and z vertices were included in the QA procedure.

5.6 Underlying Event Correction

The goal of the underlying event subtraction was to correct the jet energy and jet p_T for the energy of underlying events in the detector that “leak” into the jet. The underlying event was what was seen in the detector, not coming from the collision of two protons. The method used at STAR was adopted from the ALICE experiment [55]. At ALICE the method was referred to as the perpendicular cones method, while at STAR it was referred to as the off-axis cones method. For inclusive jet measurements the p_T was corrected, and for a dijet analysis the invariant mass was corrected.

To correct the jet energy, two cones were constructed at the same η as the jet, but $\pm \frac{\pi}{2}$ away from the jet in ϕ . These cones had the same radius as the jet (as seen in Figure 5.11). The p_T of the cone ($p_{T,ue}$) was defined as the scalar sum of the particles found inside the cone.

The following information was saved for each cone:

- Cone p_T
- Cone η
- Cone ϕ

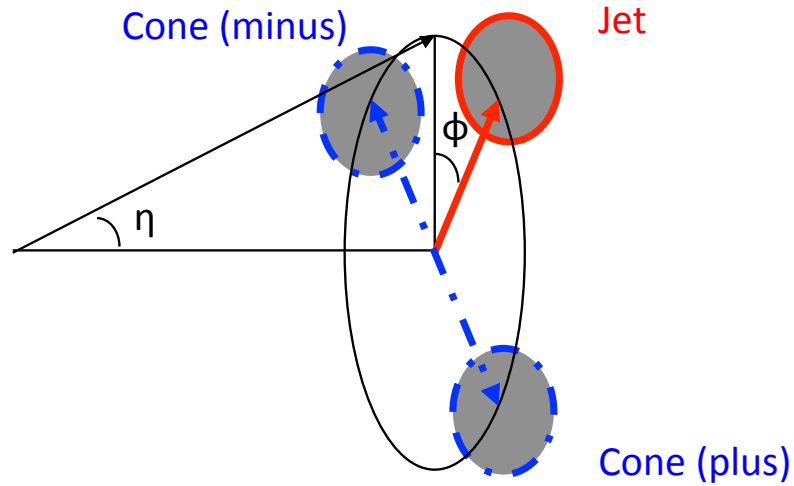


Figure 5.11: Underlying off-axis cones at the same η as the jet, but $\pm\frac{\pi}{2}$ away for the in ϕ [56].

- Cone mass

The cone mass was calculated from the tracks inside of a cone because a 4-vector in this analysis treated the towers as massless and assumed each track had the mass of a pion. The cone mass was defined as in equation 5.15.

$$\text{Cone mass} = M_{\pi} * \text{Track Multiplicity} \quad (5.15)$$

Then each cone was rotated $\pm\frac{\pi}{2}$ in ϕ so both cones were aligned with the respective jet in both η and ϕ . Once this was accomplished the mean of the cone p_T , η , ϕ , and mass was calculated.

To correct the jet p_T equation 5.16 was used. In equation 5.16 A_{jet} was the area of the reconstructed jet and A_{cone} the area of the cone defined as πR^2 , where R was the radius of the cone. For the 2013 analysis the cone radius was chosen to be 0.5.

$$p_{T,new} = p_T - p_{T,ue} * (A_{jet}/A_{cone}) \quad (5.16)$$

To correct the jet energy, first the energy of the cone was calculated.

$$E = \sqrt{P^2 + M^2}, \quad (5.17)$$

where P was the magnitude of the momentum vector.

$$p_x = p_T \cos \phi, \quad (5.18)$$

$$p_y = p_T \sin \phi, \quad (5.18)$$

$$p_z = p_T \sinh \eta, \quad (5.19)$$

Once the components of the momentum vector were determined, the magnitude of the momentum vector could be found using equation 5.20.

$$|p| = \sqrt{p_x^2 + p_y^2 + p_z^2} = p_T \cosh \eta \quad (5.20)$$

After the energy of the cone and jet were determined, the energy correction was found using equation 5.21.

$$E_{new} = E - E_{ue} * (A_{jet}/A_{cone}) \quad (5.21)$$

Finally, the corrected jet energy was found using equation 5.17. Lastly, the corrected invariant mass of the dijet event was calculated using equation 5.22. Here the subscripts 3 and 4 refer to the outgoing particles. The corrected invariant mass spectrum can be seen in Figure 5.12.

$$M_{inv} = \left(m_3^2 + m_4^2 + 2 \left[\sqrt{m_3^2 + p_{T3}^2} \sqrt{m_4^2 + p_{T4}^2} + \cosh(\eta_3 - \eta_4) - p_{T3} p_{T4} \cos(\phi_3 - \phi_4) \right] \right)^{\frac{1}{2}} \quad (5.22)$$

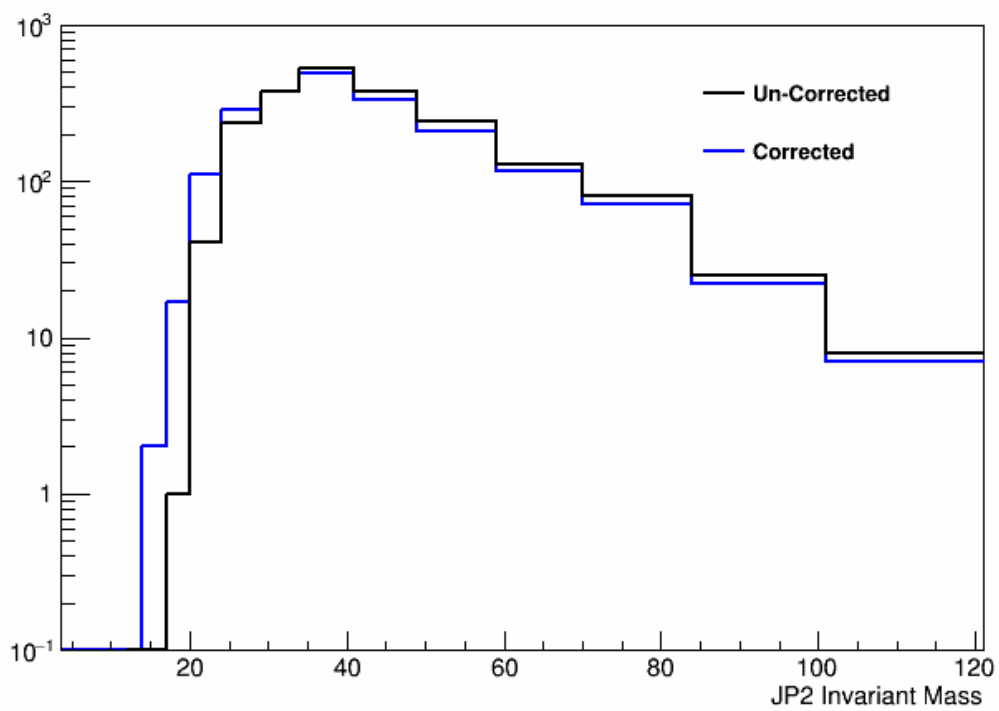


Figure 5.12: The invariant mass (in GeV/c^2) for the uncorrected (black), and the underlying event corrected (blue) distributions.

CHAPTER 6

MONTE CARLO SIMULATION

One of the most important things to do for any experimental observable is to estimate detector responses and the effects of UE and hadronization. In order to perform such estimates a reliable Monte Carlo (MC) simulation of the experiment is required. The simulation will be used to calculate systematic errors by comparing the detector response in data with the simulated detector response. The simulation is also needed to correct the invariant mass from the detector level to the parton level. This allows comparisons of experimental results to theory. A full discussion on systematic errors is presented in section 7.2.

This chapter focuses on the details of how the simulation was produced from event generation to detector simulation. Lastly, a comparison between the collected data and the MC simulation is shown.

6.1 Event Generation

The event generation was performed with PYTHIA 6.4.28 [57], a MC event generator that simulates high energy physics events, including $2 \rightarrow 2$ hard scattering processes. PYTHIA is based on analytical tools and QCD models. PYTHIA also incorporates aspects

of the standard model, with a focus on strong interactions. In addition to the basic $2 \rightarrow 2$ hard scattering, PYTHIA includes initial and final state radiation, parton showers, UE, and beam remnants. For this analysis the subprocesses simulated were those coming from the incoming parton combinations of qq , qg , and gg . For a full list see table 6.1.

Table 6.1: PYTHIA subprocesses simulated

PYTHIA ID	Subprocess
11	$q_i q_j \rightarrow q_i q_j$
12	$q_i \bar{q}_i \rightarrow q_k \bar{q}_k$
13	$q_i \bar{q}_i \rightarrow gg$
28	$q_i g \rightarrow q_i g$
53	$gg \rightarrow q_k \bar{q}_k$
68	$gg \rightarrow gg$
96	Semi-hard QCD $2 \rightarrow 2$

The parameters that control the simulation were chosen from the Perugia 2012 tune [58]. The data used to tune Perugia 2012 includes hadronic Z^0 decays from the Large Electron-Positron (LEP) collider, minimum bias Tevatron data collected at $\sqrt{s} = 630$ GeV, 1800 GeV, and 1960 GeV, Tevatron Drell-Yan data at $\sqrt{s} = 1800$ GeV, and 1960 GeV, and minimum bias data at $\sqrt{s} = 200$ GeV, 546 GeV, and 900 GeV from the Super Proton Synchrotron (SPS).

The prerequisites for perturbative collider observables are factorization and infrared (IR) safety. This allows the relation from theory to detector level observables. Factorization allows the problem to be separated into a perturbative “short distance” part and a “long distance” part, which can be constrained by data. Observables that are insensitive to the details of “long distance” physics are IR safe. Jets are one example of IR safe observables [58].

The Perugia 2012 tune was compared to STAR π^\pm results [59, 60]. Following the comparison, the Perugia 2012 tune was found to overestimate the UE. After the disagreement was discovered the exponential parameter that controlled the UE was modified to better

match the STAR environment [56].

After event generation was performed by PYTHIA, the next step was to simulate the STAR detector environment by using GEANT3 [61]. At STAR the software used for production was known as the Big Full Chain (BFC), a version of which was available for data and simulation production. An improvement in recent jet analyses was the implementation of a trigger filter. A significant amount of CPU time was required for energy response and TPC tracking in simulation. In order to save time the trigger filter would only pass events to GEANT that satisfied the trigger conditions [32]. Also at this stage of simulation production data events were “embedded” into the simulation. This was done in order to match the background of the detector, such as pile-up. Since the pile-up was affected by the luminosity, it was crucial that the luminosity of the events used for embedding be representative of the luminosity used in the analysis of the data.

For this analysis the 2012 embedding was used, since the 2013 embedding was not yet complete. The 2012 embedding events were required to satisfy at minimum the JP0 trigger energy of ~ 5.6 GeV, which corresponded to an ADC value of 29. The JP0 trigger was the lowest energy threshold. All the events that were selected for detector response had to have energy of at least 5.6 GeV. As a result this did not remove any event that satisfied a trigger with a higher energy threshold. The 2012 embedding was able to be used for the 2013 data since the energy thresholds for 2012 were below the 2013 values. This feature meant that any event that was removed for the 2012 analysis would be removed from the 2013 analysis. A full comparison between the 2012 embedding and the 2013 data is shown in section 6.2.

The embedding was produced in discrete p_T bins, this was done to compensate for the steeply falling jet cross section. If the embedding sample were produced in one large p_T bin from 5 GeV to 100 GeV, for example, there would be a large number of events at the lower energy values, but very few events in comparison at mid to high energy values. In order

to have a smooth jet p_T spectra, each bin was weighted then added together. The weight was calculated separately for each bin using equation 6.1, where σ_i is the cross section for a given bin i , and N_i is number of events produced in bin i .

$$w_i = \frac{\sigma_i}{N_i} \quad (6.1)$$

Lastly, the ‘‘fudge factors’’ were calculated to help compensate for the fact that the partonic cross section was over-estimated in the low partonic p_T bins. The ‘‘fudge factor’’ was calculated by fitting each partonic p_T bin with an exponential decay function containing a quadratic polynomial in the exponent. The yield of the exponent from each end of the bin was calculated, and the average used as the fudge factor for the bin. The fudge factors were calculated starting from the highest p_T bins working toward the lowest p_T bin. This was done since PYTHIA gave a reliable cross section at higher p_T bins [56]. The fudge factors for each p_T bin can be seen in table 6.2, along with the cross section and number of events produced.

Table 6.2: Embedding Statistics

Partonic p_T (GeV)	$\sigma(\text{mb}^{-1})$	Number of Events	Fudge Factor
4-5	1.69	297264	0.95
5-7	0.859	504580	0.97
7-9	0.178	336350	1.0
9-11	0.0509	318115	0.99
11-15	0.0251	523236	0.99
15-20	0.00532	366573	0.99
20-25	0.00106	238804	1.0
25-35	0.000371	269903	1.0
35-45	4.58×10^{-5}	113973	1.0
45-55	8.31×10^{-6}	69696	0.99
55- ∞	2.59×10^{-6}	65343	1.0

Besides the nominal embedding sample there was also a 7% track loss sample produced.

This was in order to calculate systematic errors described in section 7.2. The 7% track loss was produced in the same manner as the nominal sample, except that before the jet reconstruction was performed 7% of the tracks were randomly removed from each event.

6.2 Data and Embedding Comparison

For a reliable calculation of the systematic errors for the 2013 dijet A_{LL} , it was necessary to have good agreement between the data and the embedding samples. If there was poor agreement between the two samples, any systematic errors obtained using the embedding could not be trusted. The data and embedding sample were both required to satisfy the triggering conditions, which are explained in section 5.3.

Since the 2012 embedding sample was being compared to the 2013 data, a cut on the luminosity range of the sample had to be imposed. This was done so that the luminosity of the embedding would reflect the luminosity of the data used in the analysis. For the 2013 data set, the ZDC coincidence (ZDCX) rate ranged from as low as ~ 150 kHz to as high as 500 kHz. For the 2012 embedding sample, no runs were produced with luminosity larger than 300 kHz. The luminosity of a given run had an impact of certain quantities of interest, especially tracking related quantities. For a comparison of similar samples a luminosity range of $100 \text{ kHz} < \text{ZDCX} < 300 \text{ kHz}$ was imposed on the 2013 data and the 2012 embedding. During the 2013 data taking period, the Heavy Flavor Tracker (HFT) was partially installed on the east side ($\eta < 0$) of STAR. The addition of the HFT introduced extra material on the east side of the detector, which affected the tracking. Any runs after the partial installation of the HFT were not used for the comparison between 2013 data and 2012 embedding and removed from the analysis.

Figures 6.1, A.1, A.2, and A.3, show the jet p_T , η , ϕ , and R_t distributions for the high p_T jet of the dijet pair for the JP2 trigger. In the mentioned figures the agreement between

data and embedding was good; for the jet p_T , the agreement is near a perfect value of zero for the ratio of (data-embedding)/embedding until 80 GeV, when statistics became more limited. The overall shape comparison for both η and ϕ showed good agreement, and the R_t distribution showed agreement between data and embedding.

The disagreement in the jet quantities can be explained by the disagreement in the track and tower quantities. For example the jet p_T is the summation of all track and tower energy. In figures A.4 and A.8, the track p_T and tower E_T show good agreement between data and embedding. The track and tower multiplicities shown in figures A.7 and A.11, do not agree as well as the track p_T and tower E_T . This disagreement in multiplicities is one of the main reasons there is a disagreement in the jet p_T .

The above discussion has focused on JP2 triggered events and the jet from the dijet pair with the higher energy. The same quantities were looked at for the low energy jet in the pair, as well as the JP0, JP0DiJet, JP1, and JP1DiJet triggers. For both jets and all triggers good agreement was found between the 2012 embedding and the 2013 data.

Good agreement between data and embedding for the invariant mass distribution for the trigger combined sample was important. When calculating systematic errors, the better the agreement in the invariant mass distribution for data and embedding, the more reliable the systematic error calculation. The invariant mass for the trigger combined sample can be seen in figure 6.2. It should be noted that the underlying event correction has been applied. There was good agreement between data and embedding after 24 GeV, when trigger turn on effects were no longer relevant and the ratio was flat at $\sim 15\%$. This allowed for the calculation of reliable systematic errors.

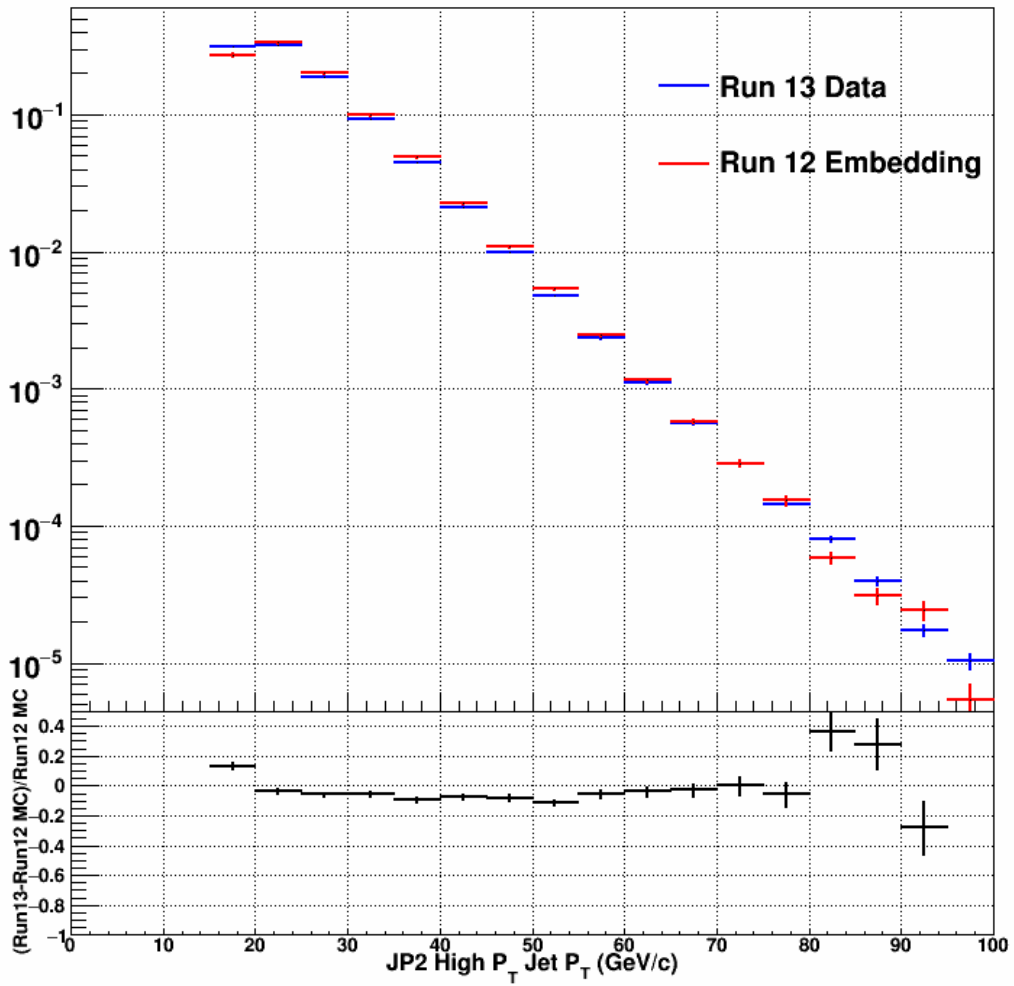


Figure 6.1: High p_T jet p_T distribution for the data (blue) and the embedding (red). The bottom of the plot shows the ratio of (data-embedding)/embedding.

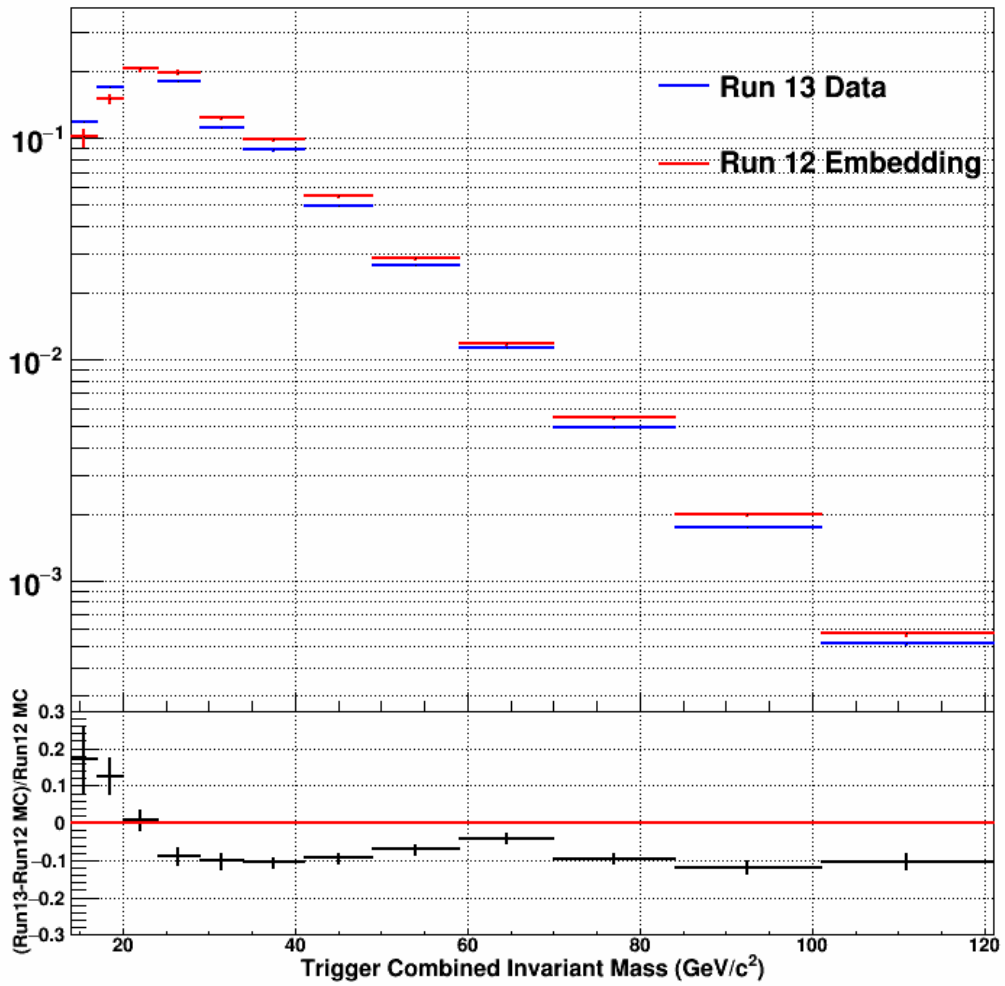


Figure 6.2: Invariant mass distribution for the trigger combined sample for the data (blue) and the embedding (red). The bottom of the plot shows the ratio of (data-embedding)/embedding.

CHAPTER 7

ASYMMETRY FORMULAE AND SYSTEMATICS

7.1 Asymmetry Formulae

The asymmetries are simply the combination of the helicity sorted yields of triggered data and the relative luminosities discussed in section 5.1. The double spin asymmetry is the helicity difference in the cross section over the sum of the cross section. STAR has the advantage that both proton beams can be polarized allowing one to obtain 4 distinct longitudinal collision patterns. The longitudinal double spin asymmetry for data is defined in equation 7.1.

$$A_{LL} = \frac{(\sigma^{++} + \sigma^{--}) - (\sigma^{+-} + \sigma^{-+})}{(\sigma^{++} + \sigma^{--}) + (\sigma^{+-} + \sigma^{-+})} \quad (7.1)$$

As in the relative luminosity definitions, the first superscript is the helicity of the blue beam and the second superscript is the helicity of the yellow beam. The cross section may

be defined as:

$$\sigma = \frac{N}{L},$$

N is the count for a given helicity state, and L is the luminosity for the same helicity state.

The asymmetry can now be written in terms of measured quantities at STAR.

$$A_{LL} = \sum_i \frac{1}{P_{B,i}P_{Y,i}} \frac{(N_i^{++} + N_i^{--}) - R_{3,i}(N_i^{+-} + N_i^{-+})}{(N_i^{++} + N_i^{--}) + R_{3,i}(N_i^{+-} + N_i^{-+})}, \quad (7.2)$$

P_B and P_Y are the polarization of the blue and yellow beam, respectively. R_3 is one of the six relative luminosities, and i runs over the final run list.

In addition to the double spin asymmetry, there were 4 other asymmetries constructed. Known as the false asymmetries, these were constructed in order to see if there were helicity dependent effects. There was the blue beam and yellow beam single spin asymmetries shown equations 7.3 and 7.4. The double spin asymmetry, when the helicity of the protons for a given collision were the same, this was known as the “like sign” asymmetry shown in equation 7.5. When the helicity of the protons for a given collision were opposite, this was called “unlike sign” asymmetry shown in equation 7.6. In equations 7.3 to 7.6, i runs over the final run list as in equation 7.2.

The false asymmetries were plotted against the parton level dijet invariant mass in the same binning as the final dijet double spin asymmetry plot. A constant function was then fitted. If the constant fit was consistent with zero for all of the false asymmetries. It implied that there were no polarization or helicity dependent effects. The plots for the mid-rapidity range ($|\eta| < 0.9$) for the four false asymmetries are shown in figures 7.1 to 7.4. Like the

double spin asymmetry, the false asymmetries were plotted in two different η dependent binnings. In the ‘‘EastEast-WestWest (EEWW)’’ configuration both jets of the dijet pair were on the same side of the detector ($|\eta_{1,2}| > 0$). The other configuration was the ‘‘East-West (EW)’’, where the jets were on opposite sides of the STAR detector ($\eta_1 > 0, \eta_2 < 0$). The fit values for the four false asymmetries for both the η dependent configurations, and the full mid-rapidity, are shown in table 7.1.

$$A_L^B = \frac{\sigma_B^+ - \sigma_B^-}{\sigma_B^+ + \sigma_B^-} \Rightarrow \sum_i \frac{1}{P_{B,i}} \frac{(N_i^{++} + N_i^{+-}) - R_{2,i}(N_i^{--} + N_i^{-+})}{(N_i^{++} + N_i^{+-}) + R_{2,i}(N_i^{--} + N_i^{-+})} \quad (7.3)$$

$$A_L^Y = \frac{\sigma_Y^+ - \sigma_Y^-}{\sigma_Y^+ + \sigma_Y^-} \Rightarrow \sum_i \frac{1}{P_{Y,i}} \frac{(N_i^{++} + N_i^{+-}) - R_{1,i}(N_i^{--} + N_i^{-+})}{(N_i^{++} + N_i^{+-}) + R_{1,i}(N_i^{--} + N_i^{-+})} \quad (7.4)$$

$$A_{LL}^{LS} = \frac{\sigma^{++} - \sigma^{--}}{\sigma^{++} + \sigma^{--}} \Rightarrow \sum_i \frac{1}{P_{B,i}P_{Y,i}} \frac{N_i^{++} - R_{4,i}N_i^{--}}{N_i^{++} + R_{4,i}N_i^{--}} \quad (7.5)$$

$$A_{LL}^{US} = \frac{\sigma^{+-} - \sigma^{-+}}{\sigma^{+-} + \sigma^{-+}} \Rightarrow \sum_i \frac{1}{P_{B,i}P_{Y,i}} \frac{N_i^{+-} - (R_{6,i}/R_{5,i})N_i^{-+}}{N_i^{+-} + (R_{6,i}/R_{5,i})N_i^{-+}} \quad (7.6)$$

Table 7.1: 2013 Dijet False Asymmetries

False Asymmetry	Full ($\times 10^{-4}$)	EEWW ($\times 10^{-4}$)	EW ($\times 10^{-4}$)
Blue	1.1 ± 3.7	6.6 ± 5.2	-4.5 ± 5.2
Yellow	-1.7 ± 3.7	-7.6 ± 5.2	4.1 ± 5.2
Like Sign	-2.9 ± 9.9	-3.1 ± 14.0	-2.8 ± 14.0
Unlike Sign	4.9 ± 9.9	24.0 ± 14.0	-14.3 ± 14.0

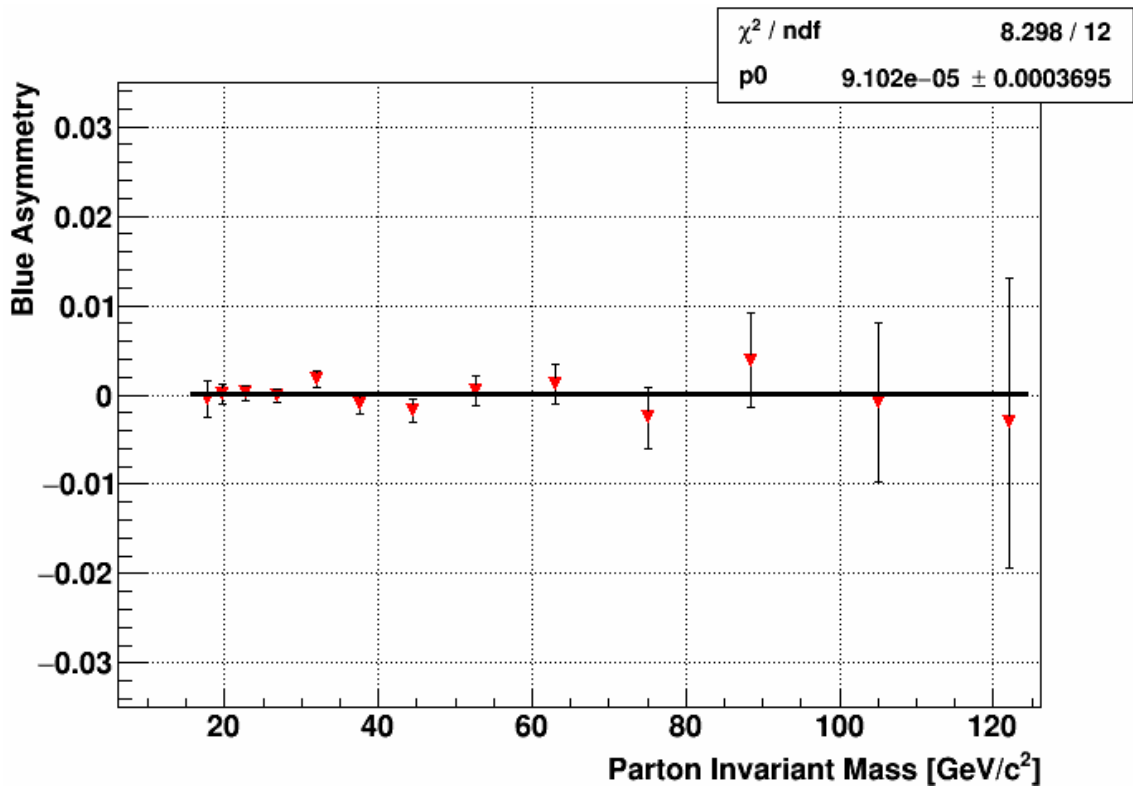


Figure 7.1: Blue beam false asymmetry vs. the dijet invariant mass. This is fitted with a constant, which is consistent with zero, signifying that there were no major helicity dependent effects.

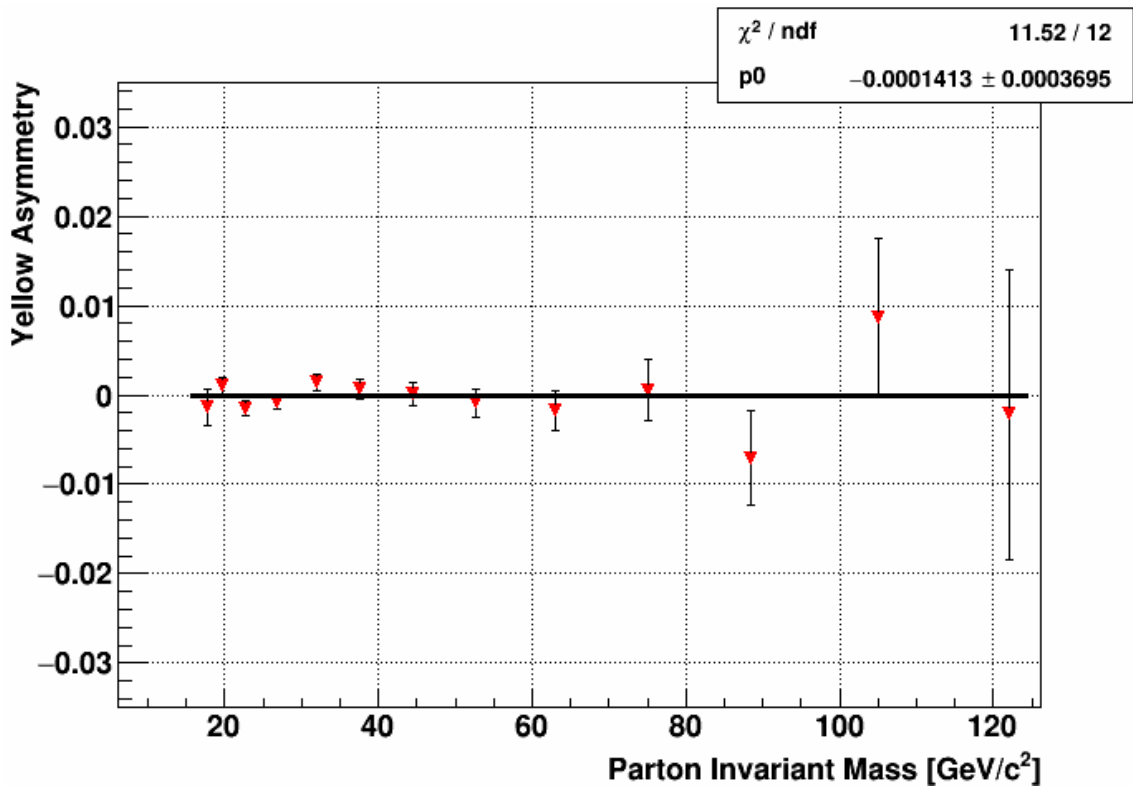


Figure 7.2: Yellow beam false asymmetry vs. the dijet invariant mass. This is fitted with a constant, which is consistent with zero, signifying that there were no major helicity dependent effects.

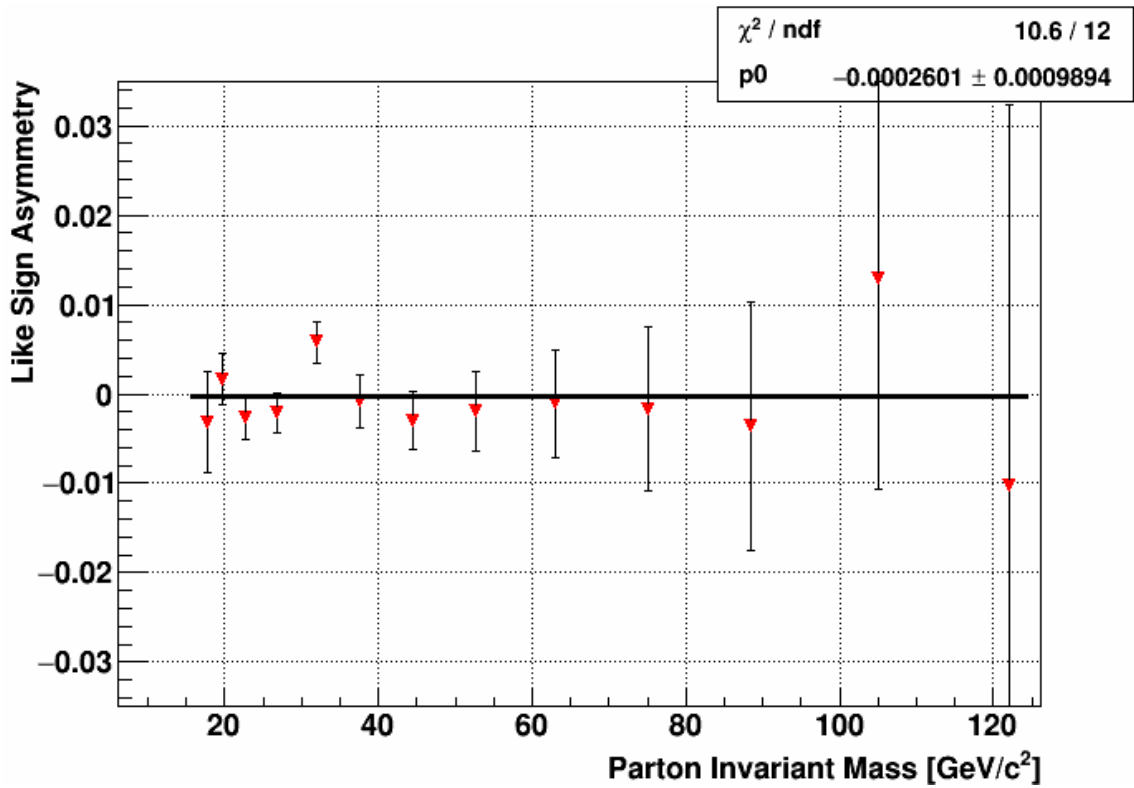


Figure 7.3: Like sign false asymmetry vs. the dijet invariant mass. This is fitted with a constant, which is consistent with zero, signifying that there were no major helicity dependent effects.

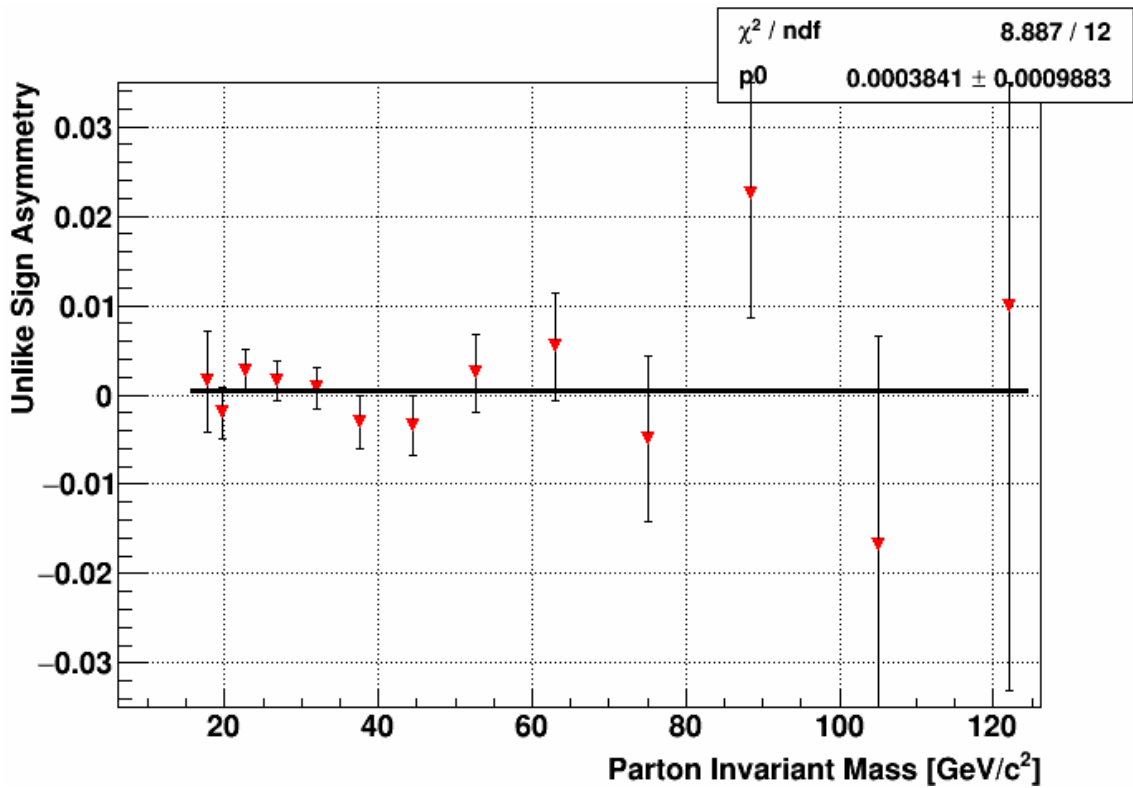


Figure 7.4: Unlike sign false asymmetry vs. the dijet invariant mass. This is fitted with a constant, which is consistent with zero, signifying that there were no major helicity dependent effects.

7.2 Systematics

This section discusses the relevant systematic errors for the 2013 dijet double spin asymmetry. It is divided into 3 subsections. The first involves all the systematic errors that are associated with the invariant mass. These include the invariant mass shift, underlying events systematic, and the Jet Energy Scale (JES). The second subsection discusses the trigger and reconstruction bias, which is the systematic error associated with the value of the double spin asymmetry. The last subsection is a description of the scale systematic errors. These errors affect the asymmetry values equally across all bins, whereas the trigger and reconstruction bias differs from bin to bin.

7.2.1 Invariant Mass Systematics

7.2.1.1 Invariant Mass Shift

The invariant mass shift procedure corrected the detector level invariant mass to the parton level invariant mass. This was accomplished by comparing the invariant mass at the detector level from the embedding sample to the parton level invariant mass. This correction was calculated because the detector level includes energy from the hard scattering process of interest as well as from underlying events, multiple parton interactions, and beam remnants. At the parton level these additional energies were not included. The correction was also done so that comparisons to theory can be made. All theoretical dijet quantities are calculated at the parton level, which does not take into account all detector responses.

The correction for the invariant mass was performed as follows. A histogram (figure 7.5) was created in which the x-axis plotted the detector level invariant mass after the underlying event subtraction had been performed, using the same detector binning as the double spin

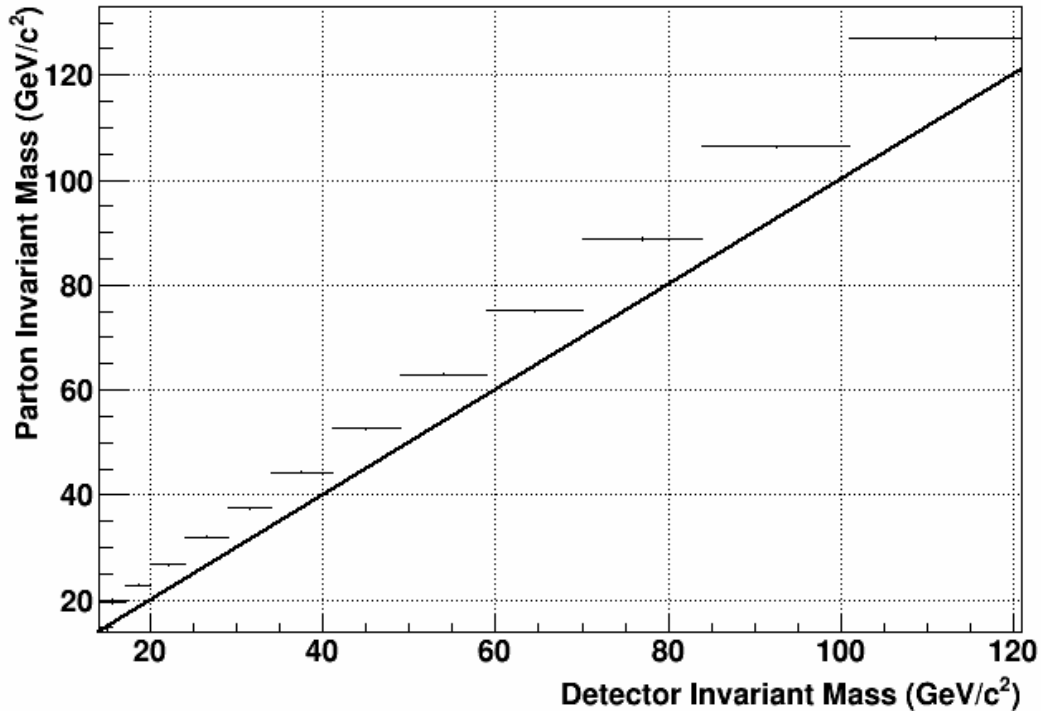


Figure 7.5: The above figure shows the invariant mass at the parton level vs. the invariant mass at the detector level. The black line shows a 1:1 relationship.

asymmetry plots. On the y-axis the average partonic invariant mass for a given detector bin was plotted. This average parton invariant mass was the invariant mass value at which the double spin asymmetry was plotted. This calculation was done separately for the three different η dependent binnings. The corrected mass values for the 3 different binnings are shown in table 7.2 for mid-rapidity ($|\eta| < 0.9$) and tables 7.3 and 7.4 for the EEWW and EW binnings, respectively.

7.2.1.2 Underlying Events Systematic

The underlying event mass systematic was the uncertainty on the invariant mass shift when the underlying event subtraction was performed. The difference in the invariant mass for the uncorrected invariant mass and the underlying event corrected invariant mass (equation 7.7) was compared against the corrected invariant mass, which was defined in the same

Table 7.2: 2013 Invariant Mass Shifted Values (in GeV/c²)

Bin #	Detector Mass Range	Parton Mass	Parton Mass Error	Parton Mass (7%)
1	14-17	19.77	0.518	20.06
2	17-20	22.89	0.271	23.38
3	20-24	26.85	0.170	27.59
4	24-29	32.03	0.143	32.76
5	29-34	37.61	0.152	38.58
6	34-41	44.38	0.119	45.38
7	41-49	52.68	0.121	54.24
8	49-59	62.97	0.131	64.92
9	59-70	75.10	0.178	77.48
10	70-84	88.78	0.208	90.95
11	84-101	106.34	0.268	108.47
12	101-121	127.04	0.384	129.53

detector binning used for the double spin asymmetry results, see figures (7.6 and 7.7). Then the average for each corrected invariant mass bin was found. These averages were used to calculate the underlying event invariant mass systematic error defined in equation 7.8.

$$\delta mass = mass_{uncorrected} - mass_{corrected} \quad (7.7)$$

$$\Delta Mass_{unc}^{UE} = \delta mass_{data} - \delta mass_{embedding} \quad (7.8)$$

7.2.1.3 Jet Energy Scale

The Jet Energy Scale (JES) systematic error was applied due to uncertainties in the BEMC towers, including gain and efficiency uncertainties. Also included was the uncertainty that charged hadrons are measured in the STAR detector, known as the track uncertainty. The final quantity measured that contributed to the JES was the uncertainty from

Table 7.3: 2013 Invariant Mass Shifted Values (in GeV/c^2) - EEW

Bin #	Detector Mass Range	Parton Mass	Parton Mass Error	Parton Mass (7%)
1	14-17	19.68	0.578	19.19
2	17-20	22.85	0.334	23.32
3	20-24	26.80	0.218	27.49
4	24-29	31.92	0.191	32.63
5	29-34	37.49	0.175	38.46
6	34-41	44.33	0.150	45.42
7	41-49	52.46	0.155	54.19
8	49-59	62.86	0.180	64.87
9	59-70	75.13	0.239	77.58
10	70-84	88.89	0.285	90.99
11	84-101	106.30	0.363	108.25
12	101-121	126.28	0.584	128.69

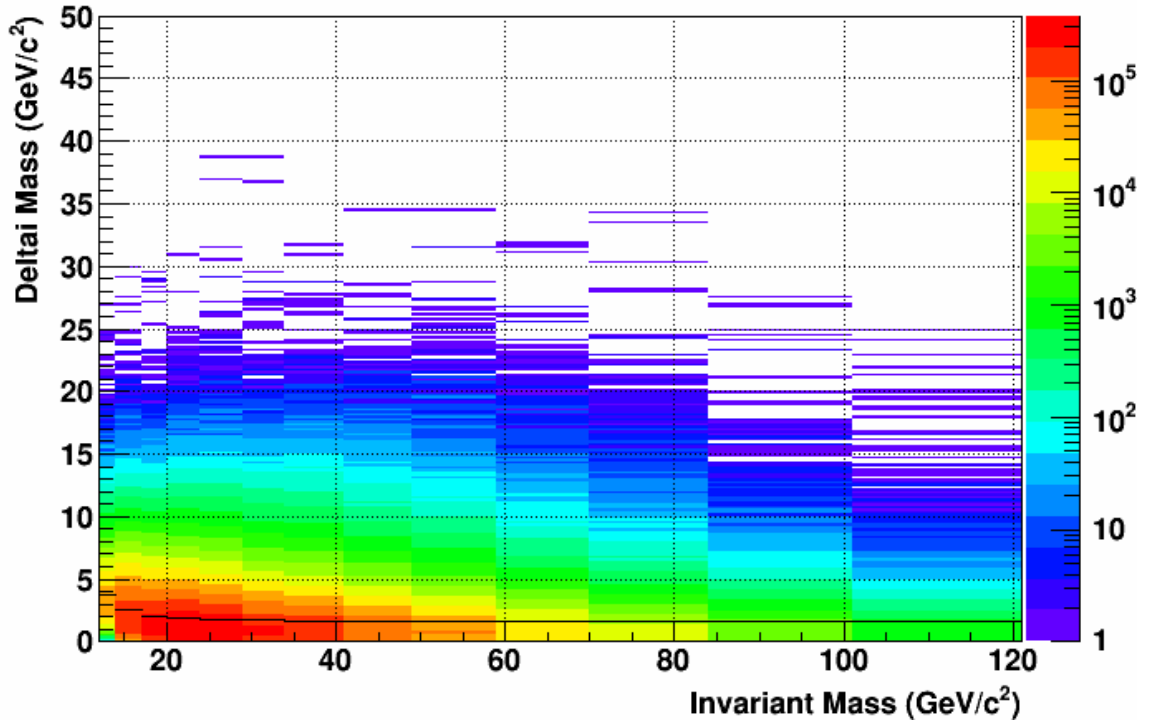


Figure 7.6: Plot of the mass difference between the corrected and uncorrected vs. the corrected invariant mass for data.

correcting the invariant mass from the detector level to the parton level.

The BEMC tower uncertainty is defined in equation 7.9.

Table 7.4: 2013 Invariant Mass Shifted Values (in GeV/c^2) - EW

Bin #	Detector Mass Range	Parton Mass	Parton Mass Error	Parton Mass (7%)
1	14-17	19.93	1.031	21.71
2	17-20	22.95	0.445	23.46
3	20-24	26.91	0.264	27.91
4	24-29	32.13	0.212	32.89
5	29-34	37.72	0.264	38.70
6	34-41	44.43	0.182	45.35
7	41-49	52.86	0.181	54.28
8	49-59	63.06	0.185	64.95
9	59-70	75.09	0.253	77.41
10	70-84	88.71	0.286	90.93
11	84-101	106.36	0.366	108.59
12	101-121	127.41	0.502	129.93

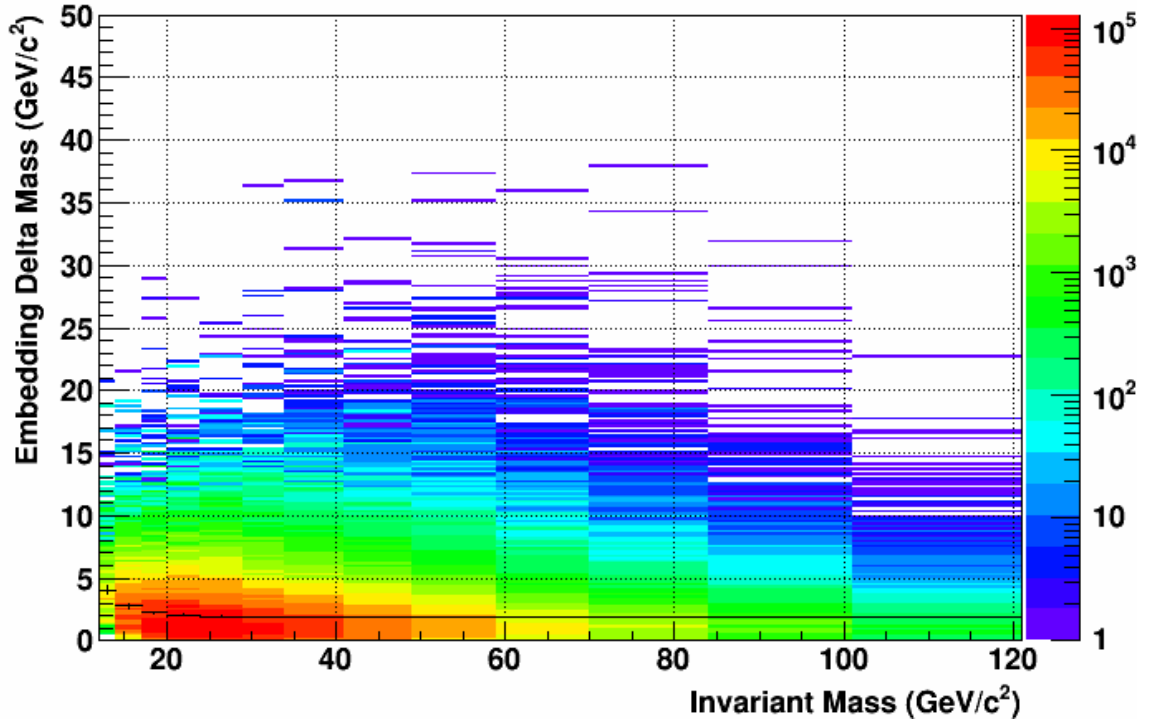


Figure 7.7: Plot of the mass difference between the corrected and uncorrected vs. the corrected invariant mass for embedding.

$$\Delta f_{Tower} = \text{Mass}_{\text{avg}} * R_t * \Delta f_{BEMC}, \quad (7.9)$$

where Δf_{BEMC} is defined in equation 7.10.

$$\Delta f_{BEMC} = \sqrt{\text{gain}^2 + \text{efficiency}^2} \quad (7.10)$$

For the 2013 data, the BEMC tower gain was estimated at 8%. This number was determined by adding the 2013 BEMC calibration value (3%) linearly with the difference between the 2012 BEMC calibration and the 2013 BEMC calibration for the period before the HFT was installed (5%). This was done because the 2013 result used the 2012 embedding. It was shown that the 2013 data from the period before the HFT was installed in STAR matched the 2012 embedding at similar level to the agreement seen between the 2012 data and embedding. For 2013 the efficiency was estimated at 2%, a slightly more conservative value compared to an efficiency of 1% used in previous analyses.

The track uncertainty was an estimate of how well charged hadrons are measured in the STAR detector and is defined in equation 7.11.

$$\Delta f_{Track} = Mass_{avg} \left([(1 - R_t) * \Delta f_{TPC}]^2 + \right. \\ \left. Max(1 - R_t, 0.5) * \Delta f_{BEMC, hadron} \right)^{\frac{1}{2}} \quad (7.11)$$

The track momentum uncertainty (Δf_{TPC}) was estimated at 1% from the TPC calibration. The “function” $Max(1 - R_t, 0.5)$ either took the values of $1 - R_t$ or if this value was below 0.5, the value 0.5 was used instead. The $\Delta f_{BEMC, hadron}$ term was the BEMC response to charged particles and is defined in equation 7.12.

$$\Delta f_{BEMC,hadron} = \frac{S_{hadron} - f_{Track,eff} * f_{Track,dep} * f_{BEMC,resp} * f_{BEMC,unc}}{f_{Track,eff}}, \quad (7.12)$$

S_{hadron} was the scale up value for neutral hadrons (1.1628), $f_{Track,eff}$ was the track efficiency estimated to be 55% for the high luminosity data taken in 2013. At STAR a track energy subtraction scheme was applied to the BEMC, as explained in section 5.4. This was performed before any jet reconstruction took place, $f_{Track,dep}$ was conservatively estimated at 50%. Finally, the last two undefined terms in equation 7.12 were the BEMC response to hadrons ($f_{BEMC,resp}$) and its uncertainty ($f_{BEMC,unc}$). These values were estimated to be 30% and 9%, respectively for the 2013 release [62].

The last quantity that contributed to the jet energy scale was the invariant mass shift uncertainty from the detector level to the parton level defined in equation 7.13.

$$\Delta Mass_{unc} = \sqrt{(Mass_{stat})^2 + (\Delta Mass_{nom-7\%})^2}, \quad (7.13)$$

$Mass_{stat}$ was the statistical uncertainty from the nominal (no track loss) embedding sample and $\Delta Mass_{nom-7\%}$ was the difference in the invariant mass between the nominal embedding sample and the 7% track loss sample. The total systematic error for the invariant mass can be found in tables 7.5, 7.6, and 7.7. The tables show the contribution from the BEMC uncertainty to track and neutral energy particle, mass shift uncertainty, and the uncertainty due to the underlying event correction.

The total systematic error on the invariant mass was the quadrature sum of columns 3 to 6. The dominant contribution is from Δf_{Tower} . Since the 2012 embedding sample was used, a conservative BEMC tower gain of 8% was chosen. Once the 2013 embedding sample is produced, the 2013 BEMC gain value of 3% can be used. This will lead to a reduced

systematic error. The higher statistics of the 2013 embedding sample might also help to reduce the mass shift uncertainty.

Table 7.5: 2013 Invariant Mass Systematic Errors (in GeV/c^2)

Bin #	R_t	Mass Shift Unc.	Δf_{Tower}	Δf_{Track}	UE Sys.	Total
1	0.568	0.594	0.719	0.386	0.182	1.03
2	0.563	0.560	0.838	0.450	0.191	1.12
3	0.536	0.759	0.946	0.509	0.218	1.33
4	0.514	0.744	1.092	0.590	0.198	1.46
5	0.499	0.982	1.263	0.689	0.212	1.75
6	0.489	1.007	1.472	0.818	0.211	1.97
7	0.479	1.565	1.734	0.983	0.263	2.55
8	0.468	1.954	2.030	1.178	0.260	3.06
9	0.459	2.387	2.386	1.416	0.280	3.67
10	0.454	2.180	2.803	1.686	0.259	3.94
11	0.454	2.147	3.364	2.024	0.295	4.48
12	0.456	2.520	4.059	2.429	0.286	5.37

Table 7.6: 2013 Invariant Mass Systematic Errors (in GeV/c^2) - EEW

Bin #	R_t	Mass Shift Unc.	Δf_{Tower}	Δf_{Track}	UE Sys.	Total
1	0.566	0.758	0.717	0.385	0.132	1.12
2	0.553	0.577	0.844	0.453	0.193	1.13
3	0.531	0.724	1.000	0.536	0.209	1.36
4	0.510	0.735	1.204	0.646	0.201	1.56
5	0.497	0.986	1.438	0.771	0.234	1.92
6	0.488	1.100	1.708	0.916	0.233	2.24
7	0.476	1.737	2.052	1.101	0.254	2.92
8	0.465	2.018	2.459	1.319	0.267	3.45
9	0.457	2.462	2.944	1.579	0.289	4.16
10	0.454	2.119	3.505	1.880	0.283	4.52
11	0.453	1.984	4.204	2.255	0.295	5.17
12	0.457	2.480	5.046	2.706	0.337	6.25

7.2.2 Trigger and Reconstruction Bias

The goal of the trigger and reconstruction bias was to correct the double spin asymmetry from the detector level to the parton level and to assign a total systematic error due to the

Table 7.7: 2013 Invariant Mass Systematic Errors (in GeV/c²) - EW

Bin #	R_t	Mass Shift Unc.	Δf_{Tower}	Δf_{Track}	UE Sys.	Total
1	0.572	2.057	0.722	0.387	0.327	2.24
2	0.561	0.677	0.848	0.451	0.191	1.19
3	0.540	0.842	1.003	0.510	0.232	1.43
4	0.518	0.789	1.206	0.590	0.199	1.57
5	0.501	1.010	1.439	0.689	0.196	1.90
6	0.491	0.938	1.711	0.819	0.195	2.12
7	0.481	1.432	2.055	0.984	0.278	2.71
8	0.469	1.899	2.462	1.178	0.258	3.34
9	0.461	2.334	2.948	1.417	0.276	4.03
10	0.455	2.238	3.510	1.687	0.243	4.50
11	0.454	2.260	4.213	2.025	0.297	5.20
12	0.456	2.570	5.054	2.430	0.264	6.17

effects of triggering data and jet reconstruction. To accomplish these goals detector and parton level asymmetries were compared using the NNPDFpol1.1 [4] parton distribution function. An advantage of NNPDFpol1.1 was that there was access to both the central curve from NNPDFpol1.1 (best fit) as well as 100 different replicas.

The correction from the detector level to parton level for A_{LL} was done as follows. The parton level replicas which were finely binned (2 GeV) were fitted with a 3rd order polynomial. This fit was then used to obtain the parton level asymmetry for a given invariant mass bin by using the parton mass values in tables 7.2 to 7.4 as input. This was done individually for each of the 100 replicas. Then the average difference between the detector and parton level asymmetries was calculated for the 100 replicas. The average of these 100 differences was the applied correction to the asymmetry value.

The systematic error on A_{LL} had 3 contributions: the NNPDF statistical error, correlated error, and a contribution from the 2012 embedding sample. The total systematic error was the quadrature sum of the 3 contributions. The NNPDF statistical error was due to the statistics produced in the embedding sample and determined from the best fit curve. The NNPDFpol1.1 best fit could be used since the statistics of the NNPDFpol1.1 best fit and

the replicas were approximately the same. The correlated error was simply the RMS of the difference between the detector and parton level for the 100 replicas. The last contribution was determined by calculating the average A_{LL} for the 100 replicas at the detector level. This was done for the nominal and 7% track loss embedding sample. The difference was the uncertainty contribution from using the 2012 embedding sample for 2013 data. A summary of the A_{LL} systematic errors can be seen in tables 7.8, 7.9, and 7.10. Currently the NNPDFpol1.1 statistical error and contribution from using the 2012 embedding sample are the dominant errors. Once the high statistics 2013 embedding sample is produced, the contribution from using the 2012 embedding sample can be removed. The statistical uncertainty from NNPDFpol1.1 should be slightly reduced when calculated from the 2013 embedding sample.

Table 7.8: 2013 Dijet A_{LL} Systematic Errors

Bin #	A_{LL} Correction	Correlated Error	Statistical Error	Nominal - 7%	Total
1	2.44×10^{-3}	6.70×10^{-5}	2.91×10^{-4}	-2.80×10^{-4}	4.09×10^{-4}
2	2.13×10^{-3}	7.10×10^{-5}	2.70×10^{-4}	-1.68×10^{-4}	3.26×10^{-4}
3	2.14×10^{-3}	6.10×10^{-5}	1.75×10^{-4}	-3.82×10^{-4}	4.25×10^{-4}
4	1.81×10^{-3}	6.00×10^{-5}	2.55×10^{-4}	-5.60×10^{-4}	2.68×10^{-4}
5	1.66×10^{-3}	6.70×10^{-5}	2.90×10^{-4}	-1.96×10^{-4}	3.56×10^{-4}
6	2.34×10^{-3}	6.90×10^{-5}	2.73×10^{-4}	2.20×10^{-5}	2.82×10^{-4}
7	1.71×10^{-3}	6.60×10^{-5}	5.01×10^{-4}	-9.25×10^{-4}	1.05×10^{-3}
8	1.34×10^{-3}	9.30×10^{-5}	2.19×10^{-3}	-1.19×10^{-3}	2.49×10^{-3}
9	3.49×10^{-3}	1.60×10^{-4}	5.90×10^{-4}	-9.43×10^{-4}	1.12×10^{-3}
10	3.30×10^{-3}	1.68×10^{-4}	1.96×10^{-3}	5.81×10^{-4}	2.05×10^{-3}
11	1.61×10^{-3}	8.40×10^{-5}	1.10×10^{-3}	-1.18×10^{-3}	1.61×10^{-3}
12	4.04×10^{-3}	1.38×10^{-4}	1.85×10^{-3}	-7.32×10^{-4}	1.96×10^{-3}

7.2.3 Scale Systematics

7.2.3.1 Relative Luminosity Systematic

The double spin asymmetry formula can be seen in equation 7.2 and rewritten in the form seen in equation 7.14.

Table 7.9: 2013 Dijet A_{LL} Systematic Errors - EEWW

Bin #	A_{LL} Correction	Correlated Error	Statistical Error	Nominal - 7%	Total
1	2.02×10^{-3}	6.70×10^{-5}	3.33×10^{-4}	-6.83×10^{-4}	7.63×10^{-4}
2	1.84×10^{-3}	7.40×10^{-5}	3.00×10^{-4}	-5.01×10^{-4}	5.89×10^{-4}
3	2.13×10^{-3}	6.10×10^{-5}	2.07×10^{-4}	-3.02×10^{-4}	3.71×10^{-4}
4	1.87×10^{-3}	6.50×10^{-5}	2.94×10^{-4}	1.09×10^{-4}	3.20×10^{-4}
5	1.39×10^{-3}	6.70×10^{-5}	3.47×10^{-4}	-3.63×10^{-4}	5.07×10^{-4}
6	2.23×10^{-3}	6.70×10^{-5}	2.21×10^{-4}	-5.52×10^{-4}	5.98×10^{-4}
7	1.71×10^{-3}	6.40×10^{-5}	4.17×10^{-4}	-8.62×10^{-4}	9.60×10^{-4}
8	1.36×10^{-3}	8.00×10^{-5}	5.20×10^{-4}	-1.43×10^{-4}	1.52×10^{-3}
9	3.71×10^{-3}	1.69×10^{-4}	5.16×10^{-4}	-8.20×10^{-4}	9.83×10^{-4}
10	3.56×10^{-3}	1.53×10^{-4}	2.34×10^{-3}	2.39×10^{-4}	2.36×10^{-3}
11	1.13×10^{-3}	1.04×10^{-4}	1.06×10^{-3}	-2.65×10^{-4}	1.10×10^{-3}
12	6.78×10^{-4}	2.68×10^{-4}	1.62×10^{-3}	-4.64×10^{-3}	4.92×10^{-3}

$$A_{LL} = \frac{1}{P_B P_Y} \frac{A - R_3}{A + R_3}, \quad (7.14)$$

where A is defined in equation 7.15.

$$A = \frac{N^{++} + N^{--}}{N^{+-} + N^{-+}} \quad (7.15)$$

The uncertainty on A_{LL} due to relative luminosity can be derived from equation 7.16.

$$\Delta A_{LL} = \left| \frac{\partial A_{LL}}{\partial R_3} \right| \Delta R_3 = \frac{2A}{P_B P_Y} \frac{\Delta R_3}{(A + R_3)^2}, \quad (7.16)$$

ΔR_3 was defined as the difference in R_3 measurements between the Vertex Position Detectors (VPD) and the Zero Degree Calorimeters (ZDC) shown in equation 7.17

Table 7.10: 2013 Dijet A_{LL} Systematic Errors - EW

Bin #	A_{LL} Correction	Correlated Error	Statistical Error	Nominal - 7%	Total
1	3.17×10^{-3}	7.10×10^{-5}	4.09×10^{-4}	5.13×10^{-4}	6.60×10^{-4}
2	2.52×10^{-3}	7.50×10^{-5}	3.61×10^{-4}	3.53×10^{-4}	5.10×10^{-4}
3	2.05×10^{-3}	6.40×10^{-5}	1.80×10^{-4}	-5.07×10^{-4}	5.42×10^{-4}
4	1.65×10^{-3}	5.60×10^{-5}	2.53×10^{-4}	-2.61×10^{-4}	3.68×10^{-4}
5	1.86×10^{-3}	6.90×10^{-5}	2.99×10^{-4}	-1.30×10^{-5}	3.07×10^{-4}
6	2.34×10^{-3}	7.10×10^{-5}	1.97×10^{-4}	6.10×10^{-4}	6.45×10^{-4}
7	1.59×10^{-3}	6.90×10^{-5}	3.79×10^{-4}	-1.00×10^{-3}	1.07×10^{-3}
8	1.22×10^{-3}	1.23×10^{-4}	1.92×10^{-3}	-9.58×10^{-4}	2.15×10^{-3}
9	3.06×10^{-3}	1.58×10^{-4}	4.85×10^{-4}	-1.03×10^{-3}	1.15×10^{-3}
10	2.83×10^{-4}	2.28×10^{-4}	9.84×10^{-4}	8.27×10^{-4}	1.31×10^{-3}
11	1.67×10^{-3}	7.50×10^{-5}	1.11×10^{-4}	-1.83×10^{-3}	2.14×10^{-3}
12	2.57×10^{-3}	1.05×10^{-4}	1.45×10^{-3}	1.20×10^{-3}	1.88×10^{-3}

$$\Delta R_3 = R_3^{VPD} - R_3^{ZDC} \quad (7.17)$$

By rearranging equation 7.14, A could be solved for in terms of A_{LL} .

$$A = \frac{1 + P_B P_Y A_{LL}}{1 - P_B P_Y A_{LL}} R_3 \quad (7.18)$$

Then by plugging equation 7.18 into 7.16 the error can be found. This is shown in equation 7.19.

$$\Delta A_{LL} = \frac{1}{P_B P_Y} \frac{\Delta R_3}{2R_3} 1 - (P_B P_Y A_{LL})^2 \quad (7.19)$$

The A_{LL}^2 term could be neglected, since A_{LL} is of order 10^{-2} at most. Neglecting the

A_{LL}^2 term further reduced equation 7.19.

$$\Delta A_{LL} = \frac{1}{P_B P_Y} \frac{\Delta R_3}{2R_3} \quad (7.20)$$

Using the simplified ΔA_{LL} form defined in equation 7.20, ΔA_{LL} due to relative luminosity was determined to be 5.60×10^{-4} for the 2013 dijet analysis.

7.2.3.2 Polarization Systematic

The uncertainty in the polarization measurement at RHIC was due to the uncertainties in the measurement from the hydrogen gas jet (h-jet) polarimeter and the proton+carbon (pC) polarimeter. For the h-jet polarimeter there were two sources of error. The first was the scale uncertainty from the Breit-Rabi polarization measurement. For the 2013 double spin asymmetry this value was 6%. The second contribution was the background for the h-jet polarimeter. The background error was the upper limit of the uncertainty on the h-jet polarimeter. For the 2013 double spin asymmetry this error was 2%. The last contribution was the uncertainty on the pC measurement. For the data used in 2013 dijet analysis, this uncertainty was $\sim 1\%$. The total polarization systematic error was 6.4%. This number was obtained by adding in quadrature the three contributions described above [35].

7.2.3.3 Underlying Events Scale Systematics

After the underlying event technique was applied to the data, some events were shifted from higher invariant mass bins into lower invariant mass bins. This process had an effect on the asymmetry itself. To estimate this systematic uncertainty, an underlying event asymmetry (A_{LL}^{UE}) was calculated as defined in equation 7.21.

$$A_{LL}^{UE} = \frac{1}{P_B P_Y} \frac{\langle \delta M^{++} + \delta M^{--} \rangle - \langle \delta M^{+-} + \delta M^{-+} \rangle}{\langle \delta M^{++} + \delta M^{--} \rangle + \langle \delta M^{+-} + \delta M^{-+} \rangle}, \quad (7.21)$$

δM is the difference between the corrected and uncorrected invariant mass defined in equation 7.7 for each spin state. For the 2013 dijet A_{LL} the underlying event systematic was determined to be 4.14×10^{-5} ; this was added in quadrature with the contribution from equation 7.20.

CHAPTER 8

RESULTS

The dijet A_{LL} was calculated from the JP0, JP0DiJet, JP1, JP1DiJet, and JP2 triggered events. As shown in figure 8.1, the JP0DiJet and JP1DiJet triggers were statistically dominant in the lower mass bins. For bins above 40 GeV, JP2 was the statistically dominant trigger. The distribution of events when trigger separated was similar for the EEWW η configuration (figure 8.2) and EW η configuration (figure 8.3) as for the full mid-rapidity results.

The 2013 STAR dijet A_{LL} results were shown in three different η dependent configurations. The first shown in 8.4 was the dijet A_{LL} that covered the region $|\eta| < 0.9$. The other two configurations were the “EastEast-WestWest” (EEWW) and “East-West” (EW). The EEWW dijet double spin asymmetry was shown in figure 8.5. The jets had the same sign in η , both jets either had η positive or negative. This was advantageous since one of the jets had a low momentum fraction that was of interest since data were limited in this region. Lastly there was the EW configuration shown in figure 8.6, where one jet was on the east side of the detector ($\eta < 0$) and the other jet on the west side of the detector ($\eta > 0$). The dijet A_{LL} was plotted against the invariant mass, which was equal to $\sqrt{x_1 x_2} \cdot \sqrt{s}$ as derived in equation B.7. For the EW configuration the jets had similar values of x , if

the invariant mass was divided by the center-of-mass energy, as in figure 8.6, the x-axis is approximately x^2 .

The asymmetry was plotted against the parton invariant mass as calculated in section 7.2.1.1. This allowed the results to be compared to theoretical calculations. The asymmetry values had also been corrected for the trigger and reconstruction bias. The systematic errors for the invariant mass and asymmetry are shown by the boxes around the data points, including all the contributions discussed in section 7.2. The grey box from 0 GeV to 10 GeV represents the quadrature sum of the relative luminosity and UE systematic errors. Not shown on any of the asymmetry plots is the uncertainty of the polarization measurement, which was 6.4% for double spin asymmetry. All values for the plots are listed in tables 8.1, 8.2, and 8.3.

The asymmetries were compared to two different theoretical models, DSSV14 [3] and NNPDFpol1.1 [4]. These models were obtained independently by fitting to the world data available, which included the 2009 STAR inclusive jet A_{LL} [5]. The asymmetries for the three different η configurations agreed with the global fits, but the 2013 data seemed to prefer the NNPDFpol1.1 fit over the DSSV14 fit.

The 2013 A_{LL} was also shown in comparison to previous STAR results. For the mid-rapidity results (figure 8.4), the comparison was between the 2012 [63] and 2013 results. Across the full invariant mass range the two data sets were in statistical agreement. This lent further confidence to both results, as they were calculated independently from different data sets. The A_{LL} systematic uncertainties were reduced in 2013, due to the using NNPDFpol1.1 to calculate the trigger and reconstruction bias. This was not possible for the 2012 results since NNPDFpol1.1 was not released in time for the release of the 2012 dijet double spin asymmetry. For the EEWW and EW configuration the 2013 results were compared to the 2009 published results [64]. At the time of the 2013 release, the 2012 data were not yet calculated for anything other than the full mid-rapidity binning. Since

the 2009 data collected at $\sqrt{s} = 200$ GeV, and the 2013 data was collected at $\sqrt{s} = 510$ GeV, the invariant mass for 2009 and 2013 were divided by their respective center of mass energy. Overall the 2009 and the 2013 data agreed with each other, with the 2013 dijet A_{LL} having 5 data points below the 2009 results. This allowed STAR to probe to lower values in x .

The data from this analysis probed a limited range in x , from 0.02 to 0.2. If the analysis were extended into the EEMC ($\eta < 2$), it will allow STAR to probe even lower in x , where data are limited. Recently a procedure to extend the dijet results into EEMC was completed and the 2009 dijet A_{LL} was released [65]. If the 2013 dijet A_{LL} was extended into the EEMC region it will allow STAR to probe down to 1×10^{-2} in x as seen in figure 8.7. If a forward tracking and calorimeter ($2 < \eta < 4$) upgrade were installed [66], STAR dijet measurements could access $x \sim 5 \times 10^{-3}$. These measurements would provide new insight before the construction of an Electron-Ion Collider (EIC).

The jet and dijet program at RHIC has continued to take advantage of high precision proton data being collected at RHIC. Once the 2009 inclusive jet asymmetry was included into DSSV14 and NNPDFpol1.1, it showed for the first time a non-zero polarized gluon contribution toward the spin of the proton. The 2013 dijet asymmetry continues to help constrain Δg . Dijet measurements at $\sqrt{s} = 510$ GeV not only probe lower in x , but also help to constrain the shape of Δg .

Improvements to the measurement can be achieved once the 2013 embedding sample is produced. As discussed in chapter 6, a portion of the data set was not included in the release since the 2012 embedding sample was used. Once all the data are included, the 2013 results will have statistical error bars ~ 3 times smaller than the 2012 results. The use of a dedicated 2013 embedding sample would also reduce the systematic error on both the invariant mass and double spin asymmetry values. The reduction in statistical and systematic errors could lead the measurement of the double spin asymmetry at mid-rapidity to be systematically

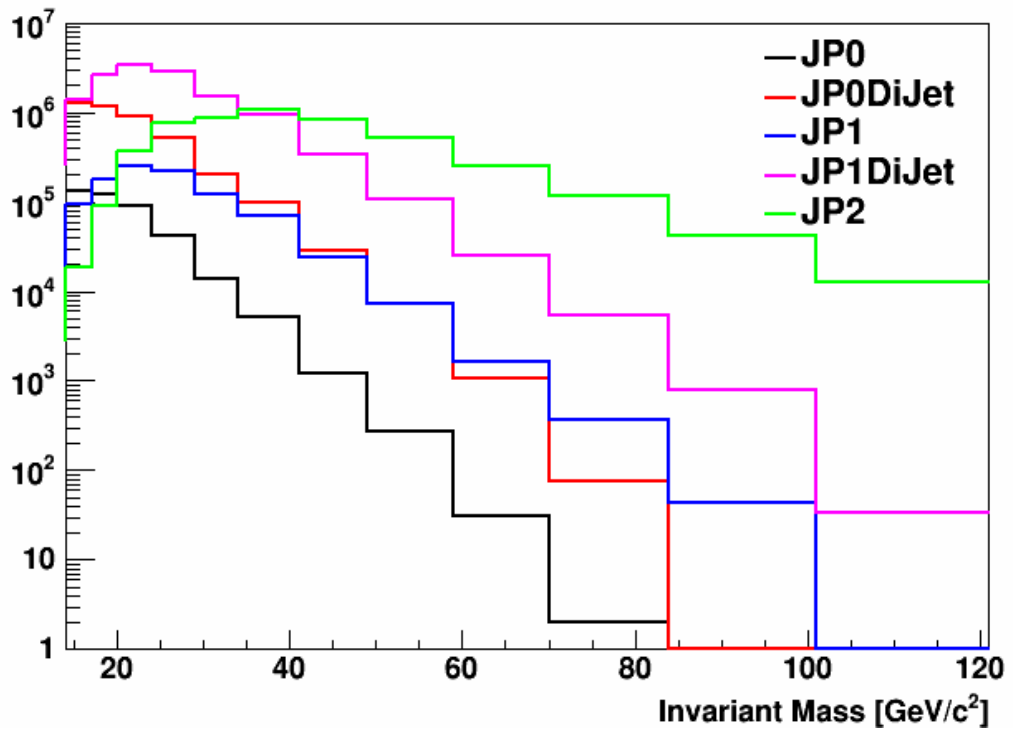


Figure 8.1: The invariant mass distribution separated by trigger.

limited at STAR.

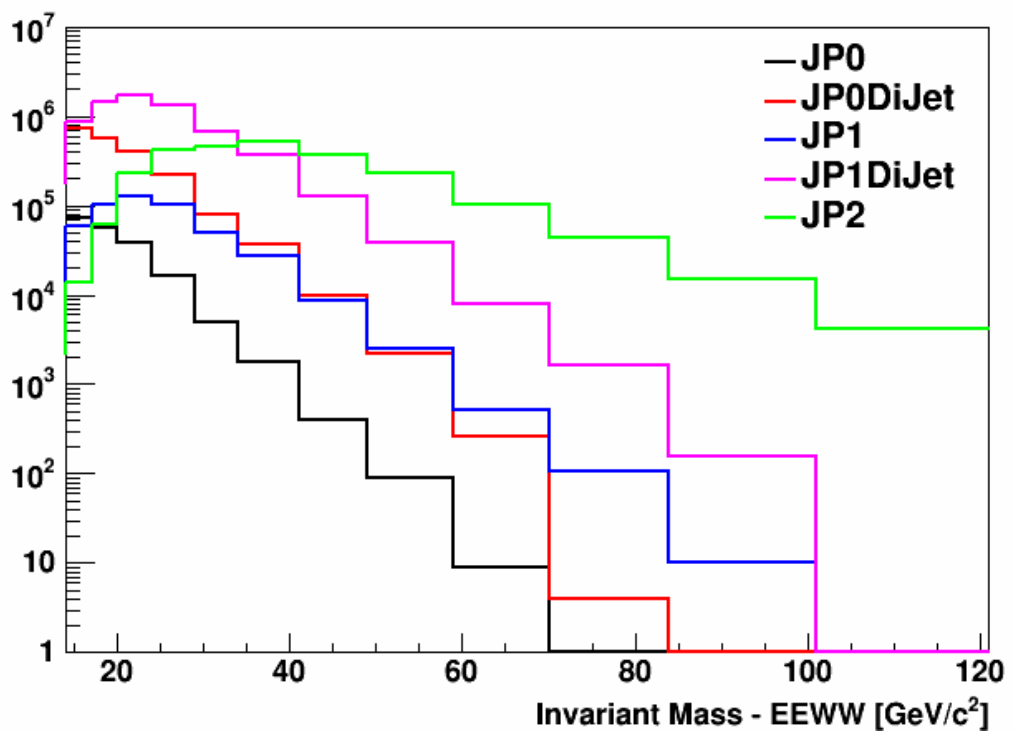


Figure 8.2: The invariant mass distribution separated by trigger for the EEW η dependent configuration.

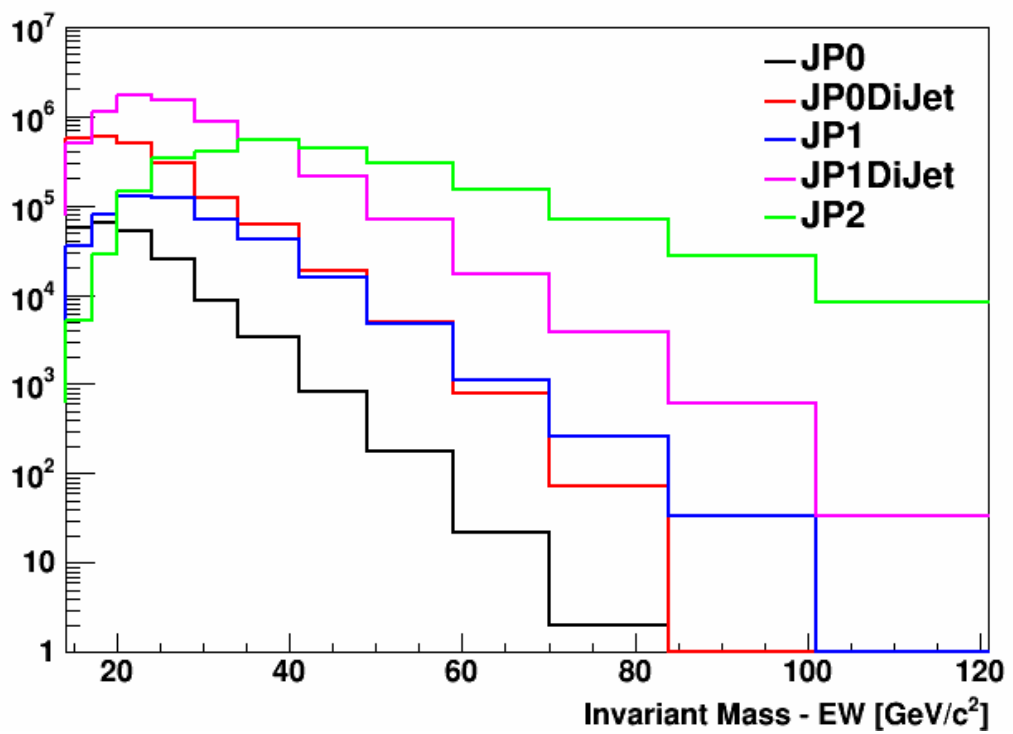


Figure 8.3: The invariant mass distribution separated by trigger for the EW η dependent configuration.

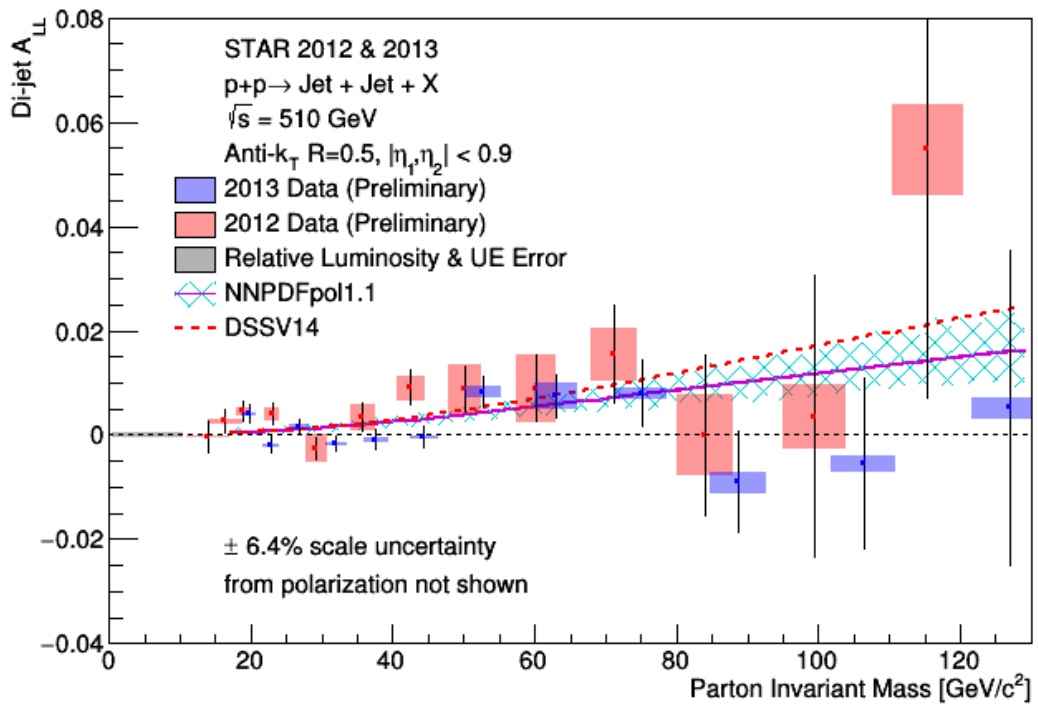


Figure 8.4: Dijet double spin asymmetry (A_{LL}) for 2013 (blue) compared to the 2012 result (red).

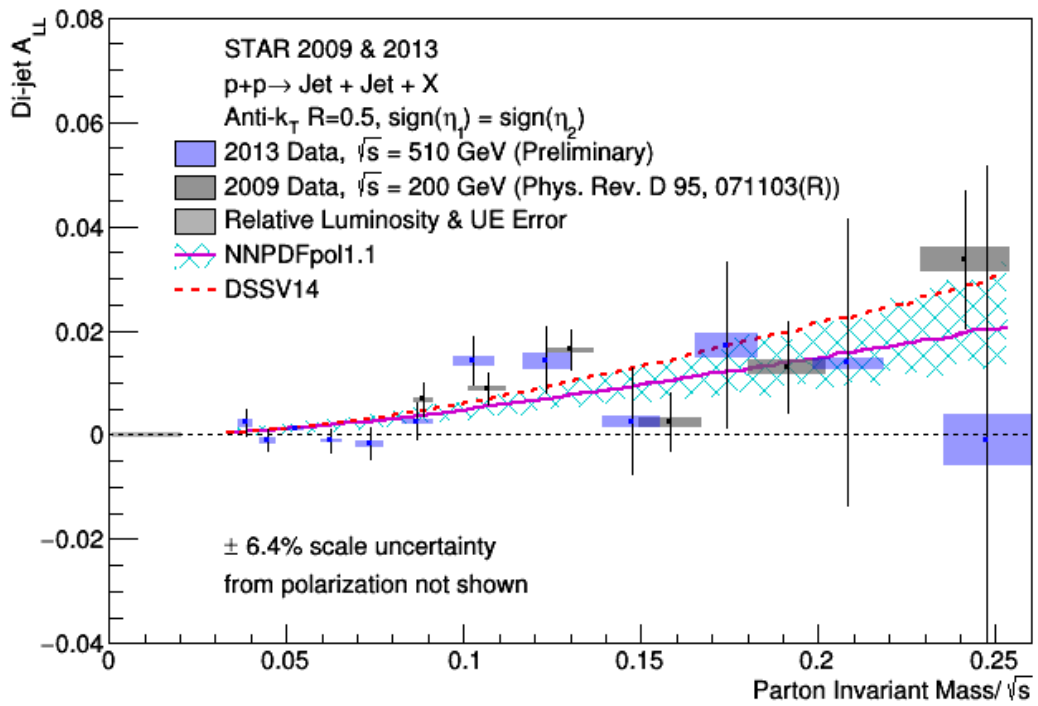


Figure 8.5: Dijet double spin asymmetry (A_{LL}) for 2013 (blue) compared to the 2009 published result (grey) for the EEWW topology.

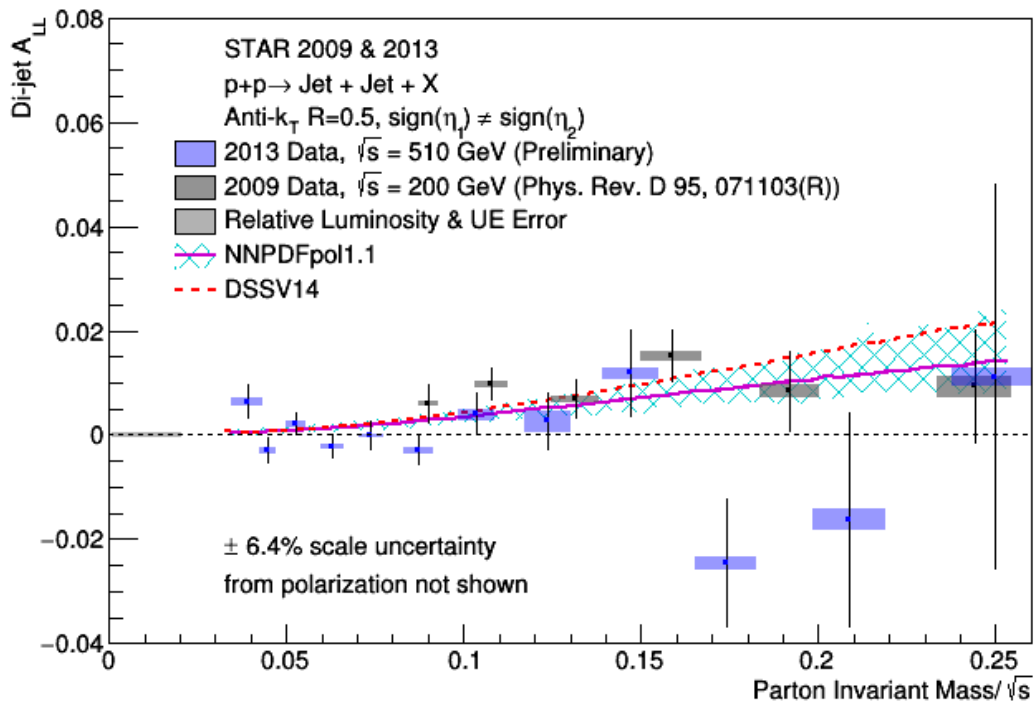


Figure 8.6: Dijet double spin asymmetry (A_{LL}) for 2013 (blue) compared to the 2009 published result (grey) for the EW topology.

Table 8.1: 2013 Dijet A_{LL} Values

Bin #	Plotted Mass	Mass Sys.	Raw A_{LL}	A_{LL} Correction	Plotted A_{LL}	A_{LL} Stat.	A_{LL} Sys.
1	19.77	1.03	6.38×10^{-3}	2.44×10^{-3}	3.95×10^{-3}	2.04×10^{-3}	4.09×10^{-4}
2	22.89	1.12	1.69×10^{-4}	2.14×10^{-3}	-1.97×10^{-3}	1.70×10^{-3}	3.26×10^{-4}
3	26.85	1.33	3.67×10^{-3}	2.14×10^{-3}	1.54×10^{-3}	1.54×10^{-3}	4.25×10^{-4}
4	32.03	1.46	-2.10×10^{-5}	1.81×10^{-e}	-1.83×10^{-3}	1.64×10^{-3}	2.68×10^{-4}
5	37.61	1.75	6.70×10^{-4}	1.66×10^{-3}	-9.85×10^{-4}	2.09×10^{-3}	3.56×10^{-4}
6	44.38	1.97	1.81×10^{-3}	2.34×10^{-3}	-5.22×10^{-4}	2.34×10^{-3}	2.82×10^{-4}
7	52.68	2.55	9.95×10^{-3}	1.71×10^{-3}	8.24×10^{-3}	3.12×10^{-3}	1.05×10^{-3}
8	62.97	3.06	8.69×10^{-3}	1.34×10^{-3}	7.36×10^{-3}	4.24×10^{-3}	2.49×10^{-3}
9	75.10	3.67	1.14×10^{-2}	3.49×10^{-3}	7.92×10^{-3}	6.51×10^{-3}	1.12×10^{-3}
10	88.78	3.94	-5.82×10^{-3}	1.61×10^{-3}	-9.12×10^{-3}	9.83×10^{-3}	2.05×10^{-3}
11	106.34	4.48	-4.02×10^{-3}	1.61×10^{-3}	-5.62×10^{-3}	1.66×10^{-2}	1.61×10^{-3}
12	127.04	5.37	9.13×10^{-3}	4.04×10^{-3}	5.09×10^{-3}	3.03×10^{-2}	1.99×10^{-3}

Table 8.2: 2013 Dijet A_{LL} Values - EEW

Bin #	Plotted Mass	Mass Sys.	Raw A_{LL}	A_{LL} Correction	Plotted A_{LL}	A_{LL} Stat.	A_{LL} Sys.
1	19.68	1.12	4.28×10^{-3}	2.02×10^{-3}	2.26×10^{-3}	2.64×10^{-3}	7.63×10^{-4}
2	22.85	1.13	7.39×10^{-4}	1.84×10^{-3}	-1.10×10^{-3}	2.32×10^{-3}	5.89×10^{-4}
3	26.80	1.36	3.31×10^{-3}	2.13×10^{-3}	1.18×10^{-3}	2.18×10^{-3}	3.71×10^{-4}
4	31.92	1.56	6.21×10^{-4}	1.87×10^{-3}	-1.25×10^{-3}	2.39×10^{-3}	3.20×10^{-4}
5	37.49	1.92	-3.59×10^{-4}	1.39×10^{-3}	-1.75×10^{-3}	3.08×10^{-3}	5.07×10^{-4}
6	44.33	2.24	4.75×10^{-3}	2.23×10^{-3}	2.52×10^{-3}	3.50×10^{-3}	5.98×10^{-4}
7	52.46	2.92	1.58×10^{-2}	1.71×10^{-3}	1.41×10^{-3}	4.74×10^{-3}	9.60×10^{-4}
8	62.86	3.45	1.56×10^{-2}	1.36×10^{-3}	1.42×10^{-2}	6.58×10^{-3}	1.52×10^{-3}
9	75.13	4.16	6.21×10^{-3}	3.71×10^{-3}	2.50×10^{-3}	1.03×10^{-2}	9.83×10^{-4}
10	88.89	4.52	2.06×10^{-2}	3.56×10^{-3}	1.71×10^{-2}	1.60×10^{-2}	2.36×10^{-3}
11	106.30	5.17	1.48×10^{-2}	1.13×10^{-3}	1.37×10^{-2}	2.77×10^{-2}	1.10×10^{-3}
12	126.28	6.25	-3.47×10^{-4}	6.78×10^{-4}	-1.03×10^{-3}	5.26×10^{-2}	4.92×10^{-3}

Table 8.3: 2013 Dijet A_{LL} Values - EW

Bin #	Plotted Mass	Mass Sys.	Raw A_{LL}	A_{LL} Correction	Plotted A_{LL}	A_{LL} Stat.	A_{LL} Sys.
1	19.93	2.24	9.48×10^{-3}	3.17×10^{03}	6.32×10^{-3}	3.21×10^{-3}	6.60×10^{-4}
2	22.95	1.19	-5.00×10^{-4}	2.52×10^{-3}	-3.02×10^{-3}	2.51×10^{-3}	5.10×10^{-4}
3	26.91	1.43	4.03×10^{-3}	2.05×10^{-3}	1.98×10^{-3}	2.17×10^{-3}	5.42×10^{-4}
4	32.14	1.57	-5.98×10^{-4}	1.65×10^{-3}	-2.25×10^{-3}	2.26×10^{-3}	3.68×10^{-4}
5	37.32	1.90	1.55×10^{-3}	1.86×10^{-3}	-3.18×10^{-4}	2.84×10^{-3}	3.07×10^{-4}
6	44.43	2.12	-5.63×10^{-4}	2.34×10^{-3}	-2.90×10^{-3}	3.15×10^{-3}	6.45×10^{-4}
7	52.86	2.71	5.49×10^{-3}	1.59×10^{-3}	3.90×10^{-3}	4.13×10^{-3}	1.07×10^{-3}
8	63.06	3.34	3.79×10^{-3}	1.22×10^{-3}	2.57×10^{-3}	5.53×10^{-3}	2.15×10^{-3}
9	75.09	4.03	1.48×10^{-2}	3.06×10^{-3}	1.18×10^{-2}	8.38×10^{-3}	1.15×10^{-3}
10	88.71	4.50	-2.19×10^{-2}	2.83×10^{-3}	-2.47×10^{-2}	1.25×10^{-2}	1.31×10^{-3}
11	106.36	5.20	-1.47×10^{-2}	1.67×10^{-3}	-1.63×10^{-2}	2.07×10^{-2}	2.14×10^{-3}
12	127.41	6.17	1.37×10^{-2}	2.57×10^{-3}	1.11×10^{-2}	3.71×10^{-2}	1.88×10^{-3}

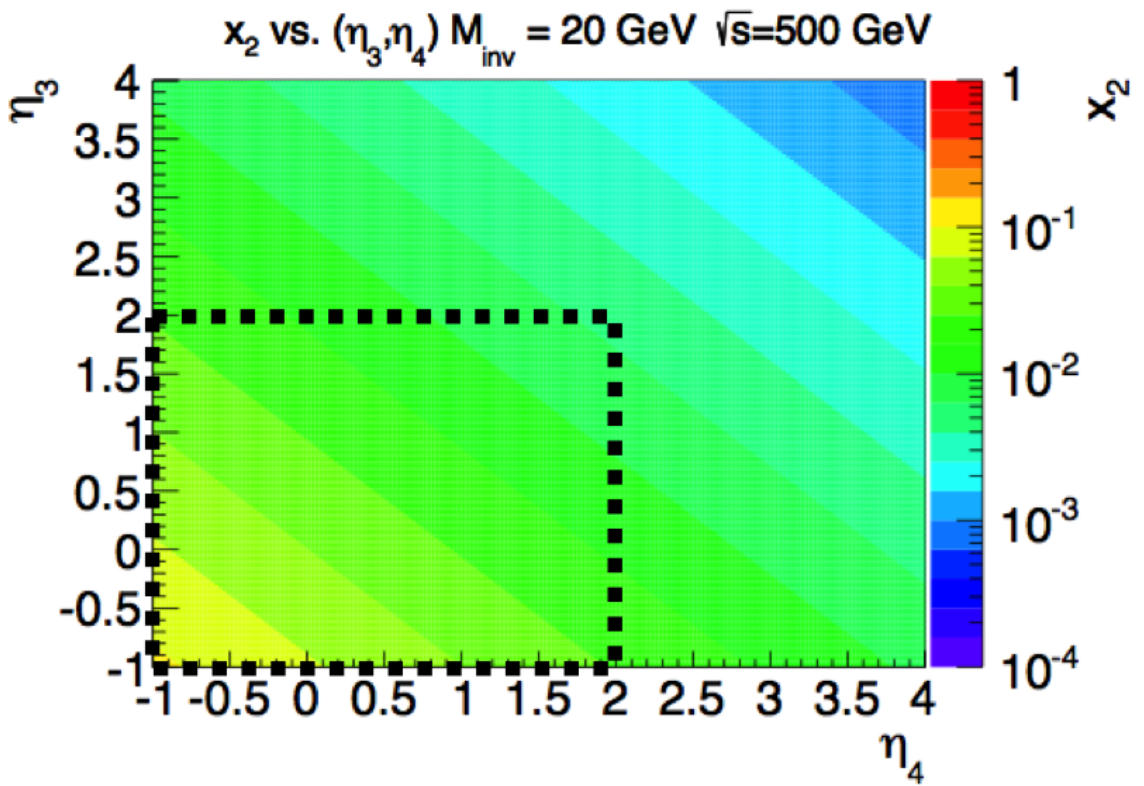


Figure 8.7: The reach of x at STAR as a function of η_3 and η_4 . The black dashed line shows where the released STAR results have accessed.

CHAPTER 9

SUMMARY

Recent theoretical models from the DSSV group [3] and the NNPDF collaboration [4] show for the first time a statistically significant non-zero gluon contribution to the spin of the proton. At present there are sizeable uncertainties on the intrinsic gluon's contribution to the total spin of the proton at lower values of Bjorken x ($x < 0.05$). The inclusion of the STAR dijet double spin asymmetry results at $\sqrt{s} = 510$ GeV, would be one way to reduce the uncertainties in Bjorken x range of 0.01 to 0.05. The latest fits from DSSV and NNPDF only include RHIC data at $\sqrt{s} = 200$ GeV, and the only STAR measurements included are the inclusive jet measurements. The inclusion of the dijet A_{LL} from years 2009, 2012, and 2013 would help reduce the uncertainty of ΔG and to constrain the shape of the polarized gluon distribution.

The 2009 inclusive jet A_{LL} [5] is a key measurement that reduced the uncertainty for the polarized gluon distribution for Bjorken x in the range 0.05 to 0.2 when included in DSSV14 and NNPDFpol1.1. Like the dijet A_{LL} , the inclusive jet A_{LL} was determined from data collected at $\sqrt{s} = 510$ GeV in order to reduce the uncertainty at smaller values of Bjorken x .

Figure 9.1 shows the 2013 inclusive jet preliminary results (blue) compared to the 2012

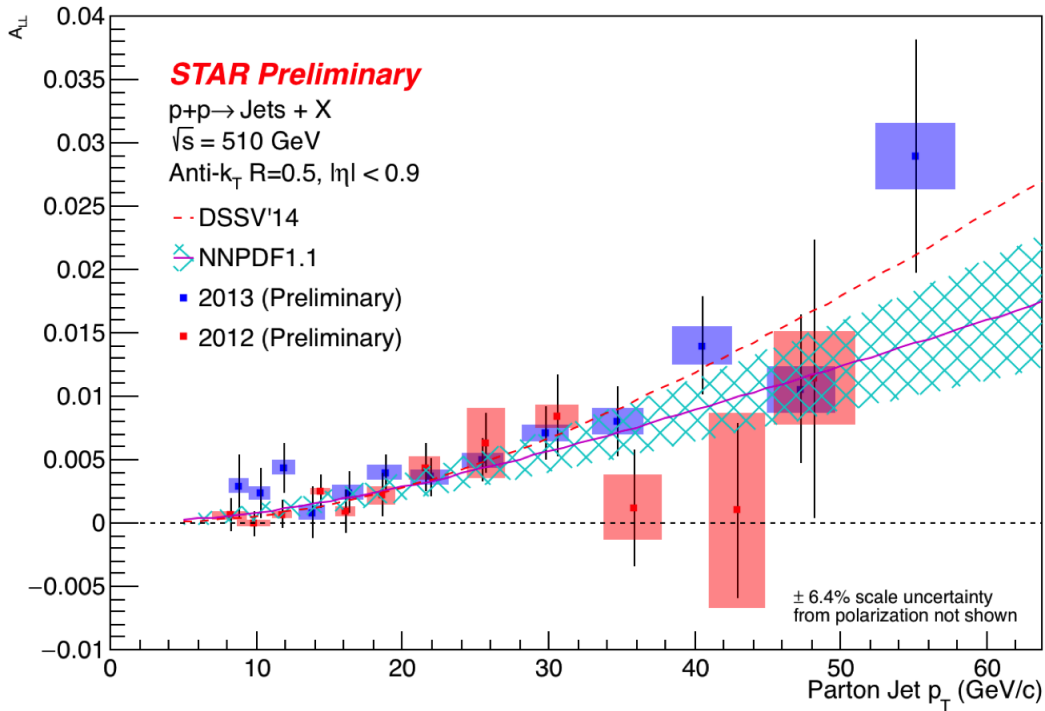


Figure 9.1: Inclusive jet double spin asymmetry (A_{LL}) for 2013 (blue) compared to the 2012 result (red).

preliminary results (red) [67]. The 2013 results are consistent with the 2012 results. The 2012 and 2013 measurements are in agreement with the Next to Leading Order (NLO) calculations from DSSV14 and NNPDFp01.1. Similar to the dijet A_{LL} results, the trigger and reconstruction bias systematic has been reduced for the 2013 results compared to the 2012 results. In addition to inclusive jet and dijet measurements, one could perform a prompt photon jet measurement, where a photon is produced in the reaction, $qg \rightarrow \gamma q$. At STAR this could be measured on an event-by-event basis by the observation of a photon plus a jet [2].

Currently, RHIC is capable of measurements that are sensitive down to $x \sim 1 \times 10^{-2}$ as can be seen in figure 8.7. Uncertainty estimates utilizing all the longitudinally polarized data collected at RHIC can be seen in figure 9.2. The latest release from the DSSV group is shown in blue and uncertainties can be reduced with the inclusion of more data, but this

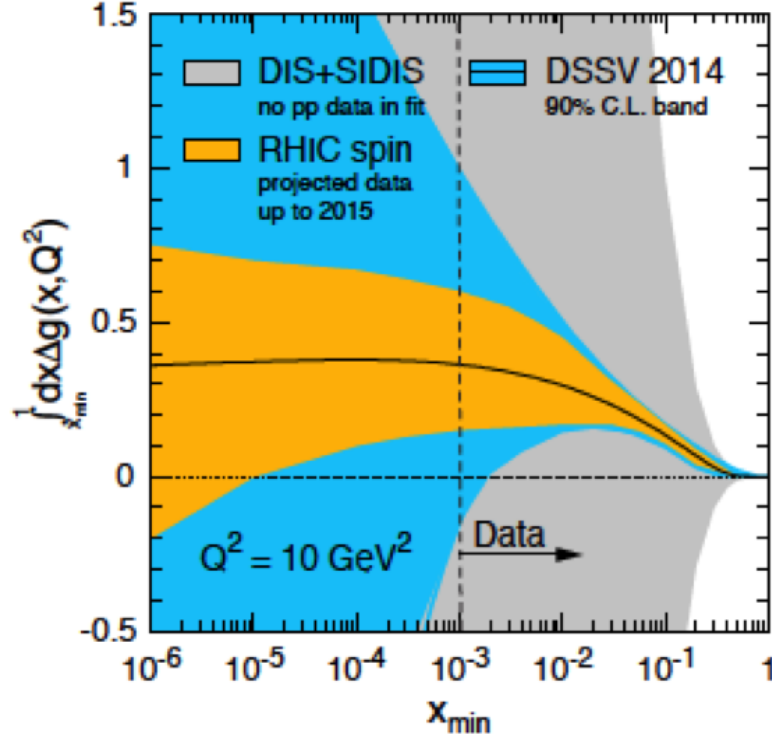


Figure 9.2: Uncertainty estimates on the polarized gluon distribution: Grey shows the uncertainty without any RHIC data, blue is the current DSSV14 fit, and orange shows the expected precision with the inclusion of all RHIC data up to 2015. To the right of the vertical dashed line shows the region constrained by data [68].

is limited to a Bjorken x value of $\sim 1 \times 10^{-3}$.

Ultimately, if measurements are to be made to reduce the uncertainty of the spin structure of the proton at lower values of Bjorken x an Electron Ion Collider (EIC) is needed. If an EIC is constructed with a maximum center of mass energy of 141 GeV, it would be capable of accessing Bjorken x values below 1×10^{-4} . This is more than an order of magnitude smaller than currently available polarized data. The EIC would make high precision measurements, and begin to constrain the spin structure of the proton at Bjorken x values not accessible at RHIC [68].

If the uncertainty on the contribution to the spin of the proton from the intrinsic quarks and gluons is precise enough, it would allow for the orbital angular momentum contribution to be constrained. At present there are no measurements where the orbital angular momen-

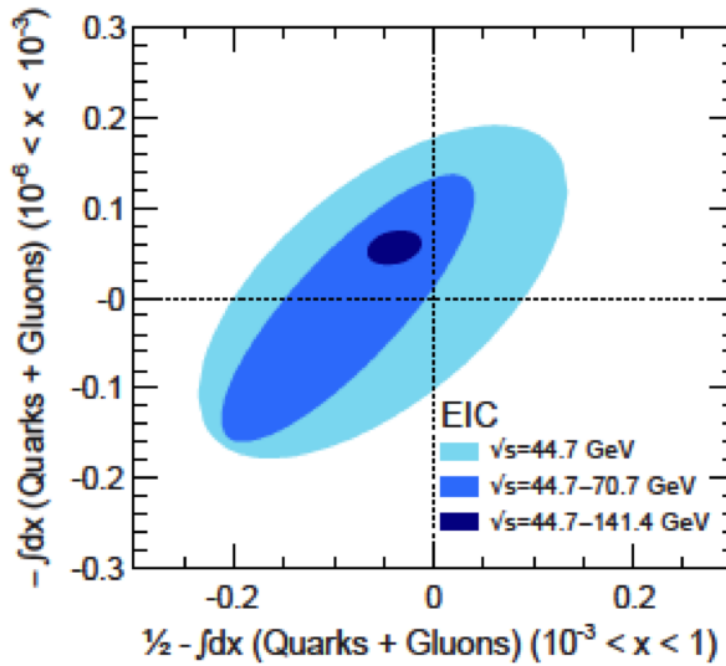


Figure 9.3: Impact of the EIC in the range $1 \times 10^{-6} < x < 1 \times 10^{-3}$ for the intrinsic quark and gluon contributions (y-axis) versus the orbital angular contribution in the range $1 \times 10^{-3} < x < 1$ (x-axis) [68].

tum of the quark or gluon is directly accessible. Figure 9.3 shows expected precision for the intrinsic quark and gluon contributions on the y-axis. The total orbital angular contribution is found by subtracting the intrinsic quark and gluon contribution from the total spin of the proton. Figure 9.3 also shows the importance of an EIC having a high center of mass energy, in order to make the precision measurements at low Bjorken x values not accessible with current facilities [68].

BIBLIOGRAPHY

- [1] Daniel de Florian, Rodolfo Sassot, Marco Stratmann, and Werner Vogelsang. Global analysis of helicity parton densities and their uncertainties. *Phys. Rev. Lett.*, 101:072001, Aug 2008.
- [2] Gerry Bunce, Naohito Saito, Jacques Soffer, and Werner Vogelsang. Prospects for spin physics at RHIC. *Ann. Rev. Nucl. Part. Sci.*, 50:525–575, 2000.
- [3] Daniel de Florian, Rodolfo Sassot, Marco Stratmann, and Werner Vogelsang. Evidence for polarization of gluons in the proton. *Phys. Rev. Lett.*, 113(1):012001, 2014.
- [4] Emanuele R. Nocera, Richard D. Ball, Stefano Forte, Giovanni Ridolfi, and Juan Rojo. A first unbiased global determination of polarized PDFs and their uncertainties. *Nucl. Phys.*, B887:276–308, 2014.
- [5] L. Adamczyk et al. Precision measurement of the longitudinal double-spin asymmetry for inclusive jet production in polarized proton collisions at $\sqrt{s} = 200$ GeV. *Phys. Rev. Lett.*, 115:092002, Aug 2015.
- [6] J. J. Thomson. Cathode rays. *Philosophical Magazine*, 44, 1897.
- [7] J.J. Thomson F.R.S. Xxiv. on the structure of the atom: an investigation of the stability and periods of oscillation of a number of corpuscles arranged at equal intervals around the circumference of a circle; with application of the results to the theory of atomic structure. *Philosophical Magazine*, 7(39):237–265, 1904.

- [8] M. Gell-Mann. *THE EIGHTFOLD WAY: A THEORY OF STRONG INTERACTION SYMMETRY*. Mar 1961.
- [9] M. Gell-Mann. A schematic model of baryons and mesons. *Physics Letters*, 8(3):214–215, 1964.
- [10] G. Zweig. An SU(3) model for strong interaction symmetry and its breaking. 1964.
- [11] O. W. Greenberg. Spin and unitary-spin independence in a paraquark model of baryons and mesons. *Phys. Rev. Lett.*, 13:598–602, Nov 1964.
- [12] Hideki Yukawa. On the Interaction of Elementary Particles I. *Proc. Phys. Math. Soc. Jap.*, 17:48–57, 1935. [Prog. Theor. Phys. Suppl.1,1(1935)].
- [13] P. Söding. On the discovery of the gluon. *The European Physical Journal H*, 35(1):3–28, Jul 2010.
- [14] Frank Wilczek. QCD made simple. *Phys. Today*, 53N8:22–28, 2000.
- [15] D. J. Gross and Frank Wilczek. ASYMPTOTICALLY FREE GAUGE THEORIES. 2. *Phys. Rev.*, D9:980–993, 1974.
- [16] John C. Collins. Hard scattering in QCD with polarized beams. *Nucl. Phys.*, B394:169–199, 1993.
- [17] John R. Ellis and Robert L. Jaffe. A Sum Rule for Deep Inelastic Electroproduction from Polarized Protons. *Phys. Rev.*, D9:1444, 1974. [Erratum: *Phys. Rev.*D10,1669(1974)].
- [18] R. L. Jaffe and Aneesh Manohar. The G(1) Problem: Fact and Fantasy on the Spin of the Proton. *Nucl. Phys.*, B337:509–546, 1990.
- [19] B. W. Filippone and Xiang-Dong Ji. The Spin structure of the nucleon. *Adv. Nucl. Phys.*, 26:1, 2001.

- [20] M. Breidenbach, J. I. Friedman, H. W. Kendall, E. D. Bloom, D. H. Coward, H. DeStaebler, J. Drees, L. W. Mo, and R. E. Taylor. Observed behavior of highly inelastic electron-proton scattering. *Phys. Rev. Lett.*, 23:935–939, Oct 1969.
- [21] J. Ashman et al. A measurement of the spin asymmetry and determination of the structure function g_1 in deep inelastic muon-proton scattering. *Physics Letters B*, 206(2):364 – 370, 1988.
- [22] Elliot Leader, Aleksander V. Sidorov, and Dimiter B. Stamenov. Longitudinal polarized parton densities updated. *Phys. Rev. D*, 73:034023, Feb 2006.
- [23] D. de Florian, G. A. Navarro, and R. Sassot. Sea quark and gluon polarization in the nucleon at nlo accuracy. *Phys. Rev. D*, 71:094018, May 2005.
- [24] Daniel de Florian, Rodolfo Sassot, Marco Stratmann, and Werner Vogelsang. Extraction of Spin-Dependent Parton Densities and Their Uncertainties. *Phys. Rev.*, D80:034030, 2009.
- [25] B. I. Abelev et al. Longitudinal double-spin asymmetry for inclusive jet production in $\vec{p} + \vec{p}$ collisions at $\sqrt{s} = 200$ GeV. *Phys. Rev. Lett.*, 100:232003, Jun 2008.
- [26] M. Harrison et al. RHIC project overview. *Nucl. Instrum. Meth.*, A499:235–244, 2003.
- [27] H. Hahn et al. The RHIC design overview. *Nucl. Instrum. Meth.*, A499:245–263, 2003.
- [28] A. Zelenski et al. Optically pumped polarized H- ion source for RHIC spin physics. *Rev. Sci. Instrum.*, 73:888–891, 2002.
- [29] Alekseev et al. Polarized proton collider at RhIC. *Nucl. Instrum. Meth.*, A499:392–414, 2003.

- [30] A. Zelenski. Review of Polarized Ion Sources. *Int. J. Mod. Phys. Conf. Ser.*, 40(01):1660100, 2016.
- [31] A. Zelenski et al. High-Intensity Polarized H- (Proton), Deuteron and 3He^{++} Ion Source Development at BNL. *Conf. Proc.*, C0806233:TUOBM03, 2008.
- [32] Matthew Walker. *Dijet production in polarized proton-proton collisions at $\sqrt{s} = 200$ GeV*. PhD thesis, MASSACHUSETTS INSTITUTE OF TECHNOLOGY, 2011.
- [33] M. Okamura et al. Half-length model of a Siberian Snake magnet for RHIC. *Nucl. Instrum. Meth.*, A452:53–60, 2000.
- [34] O. Jinnouchi et al. Measurement of the analyzing power of proton-carbon elastic scattering in the CNI region at RHIC. In *Spin physics. Polarized electron sources and polarimeters. Proceedings, 16th International Symposium, SPIN 2004, Trieste, Italy, October 10-16, 2004, and Workshop, PESP 2004, Mainz, Germany, October 7-9, 2004*, pages 515–518, 2004.
- [35] The Polarimetry Group. Rhic polarization for runs 9-15. https://wiki.bnl.gov/rhicspin/upload/e/e4/Pol_resultsMay2016.pdf. Accessed: 2017-07-11.
- [36] A. Zelenski and others. Absolute polarized H-jet polarimeter development, for RHIC. *Nucl. Instrum. Meth.*, A536:248–254, 2005.
- [37] H. Okada et al. Measurement of the analyzing power in pp elastic scattering in the peak CNI region at RHIC. *Phys. Lett.*, B638:450–454, 2006.
- [38] K. H. Ackermann et al. STAR detector overview. *Nucl. Instrum. Meth.*, A499:624–632, 2003.
- [39] M. Anderson et al. The Star time projection chamber: A Unique tool for studying high multiplicity events at RHIC. *Nucl. Instrum. Meth.*, A499:659–678, 2003.

- [40] F. Bergsma et al. The STAR detector magnet subsystem. *Nucl. Instrum. Meth.*, A499:633–639, 2003.
- [41] J. Abele et al. The laser system for the STAR time projection chamber. *Nucl. Instrum. Meth.*, A499:692–702, 2003.
- [42] Yichun Xu, Olga Barannikova, Hans Bichsel, Xin Dong, Patricia Fachini, Yuri Fisyak, Adam Kocoloski, Bedanga Mohanty, Pawan Netrakanti, Lijuan Ruan, Maria Cristina Suarez, Zebo Tang, Gene van Buren, and Zhangbu Xu. Improving the de/dx calibration of the star tpc for the high-pt hadron identification. *Nuclear Instruments and Methods in Physics Research Section A: Accelerators, Spectrometers, Detectors and Associated Equipment*, 614(1):28 – 33, 2010.
- [43] F. Bergsma et al. The STAR detector magnet subsystem. *Nucl. Instrum. Meth.*, A499:633–639, 2003.
- [44] C. E. Allgower et al. The STAR endcap electromagnetic calorimeter. *Nucl. Instrum. Meth.*, A499:740–750, 2003.
- [45] Christopher Dilks. Forward $a_{LL}^{\pi^0}$ in the fms at $\sqrt{s} = 510$ gev pp collisions during rhic runs 12 and 13.
- [46] W. J. Llope et al. The STAR Vertex Position Detector. *Nucl. Instrum. Meth.*, A759:23–28, 2014.
- [47] C. Adler et al. The RHIC zero-degree calorimeters. *Nucl. Instrum. Meth.*, A499:433–436, 2003.
- [48] Gerald C. Blazey et al. Run II jet physics. In *QCD and weak boson physics in Run II. Proceedings, Batavia, USA, March 4-6, June 3-4, November 4-6, 1999*, pages 47–77, 2000.

- [49] L. Adamczyk et al. Precision Measurement of the Longitudinal Double-spin Asymmetry for Inclusive Jet Production in Polarized Proton Collisions at $\sqrt{s} = 200$ GeV. *Phys. Rev. Lett.*, 115(9):092002, 2015.
- [50] Matteo Cacciari, Gavin P. Salam, and Gregory Soyez. The Anti-k(t) jet clustering algorithm. *JHEP*, 04:063, 2008.
- [51] James Hays-Wehle Joe Seele Hal Spinka Bernd Sorrow. Relative luminosity analysis for run9 pp 200 gev running. <https://drupal.star.bnl.gov/STAR/system/files/rellumi4.pdf>. Accessed: 2017-10-06.
- [52] E.G. Judd J.M. Engelage, C. Gagliardi. The cabling scheme and dsm algorithms for the emc trigger. http://www.star.bnl.gov/public/trg/TSL/Software/EMC_032213.pdf. Accessed: 2017-07-24.
- [53] Tai Sakuma. *Inclusive Jet and Dijet Production in Polarized Proton-Proton Collisions at $\sqrt{s} = 200$ GeV at RHIC*. PhD thesis, MASSACHUSETTS INSTITUTE OF TECHNOLOGY, 2010.
- [54] R. Reed, J. Balewski, L. S. Barnby, A. Ogawa, J. Lauret, and M. van Leeuwen. Vertex finding in pile-up rich events for p+p and d+Au collisions at STAR. *J. Phys. Conf. Ser.*, 219:032020, 2010.
- [55] Betty Bezverkhny Abelev et al. Charged jet cross sections and properties in proton-proton collisions at $\sqrt{s} = 7$ TeV. *Phys. Rev.*, D91(11):112012, 2015.
- [56] Zilong Chang. *INCLUSIVE JET LONGITUDINAL DOUBLE-SPIN ASYMMETRY ALL MEASUREMENTS IN 510 GeV POLARIZED pp COLLISIONS AT STAR*. PhD thesis, Texas A&M University, 2016.
- [57] Torbjorn Sjostrand, Stephen Mrenna, and Peter Z. Skands. PYTHIA 6.4 Physics and Manual. *JHEP*, 05:026, 2006.

- [58] Peter Zeiler Skands. Tuning Monte Carlo Generators: The Perugia Tunes. *Phys. Rev.*, D82:074018, 2010.
- [59] J. Adams et al. Identified hadron spectra at large transverse momentum in p+p and d+Au collisions at $\sqrt{s_{NN}} = 200$ -GeV. *Phys. Lett.*, B637:161–169, 2006.
- [60] G. Agakishiev et al. Identified hadron compositions in p+p and Au+Au collisions at high transverse momenta at $\sqrt{s_{NN}} = 200$ GeV. *Phys. Rev. Lett.*, 108:072302, 2012.
- [61] R Brun, F Bruyant, M Maire, A C McPherson, and P Zancarini. *GEANT 3: user's guide Geant 3.10, Geant 3.11; rev. version*. CERN, Geneva, 1987.
- [62] J. Adams et al. Measurements of transverse energy distributions in Au + Au collisions at $\sqrt{s_{NN}} = 200$ -GeV. *Phys. Rev.*, C70:054907, 2004.
- [63] Suvarna Ramachandran. Probing Gluon Helicity with Dijets from $\sqrt{s} = 510$ GeV Polarized Proton Collisions at STAR. *PoS*, DIS2016:231, 2016.
- [64] L. Adamczyk et al. Measurement of the cross section and longitudinal double-spin asymmetry for di-jet production in polarized pp collisions at $\sqrt{s} = 200$ GeV. *Phys. Rev.*, D95(7):071103, 2017.
- [65] Ting Lin. Longitudinal Double-Spin Asymmetries for Forward Di-jet Production in Polarized pp Collisions at $\sqrt{s} = 200$ GeV. In *22nd International Symposium on Spin Physics (SPIN 2016) Urbana, IL, USA, September 25-30, 2016*, 2017.
- [66] Bernd Surrow. Future prospects of di-jet production constraining $\Delta g(x)$ at low x at STAR at RHIC. *PoS*, DIS2014:241, 2014.
- [67] Zilong Chang. Gluon Polarization in Longitudinally Polarized pp Collisions at STAR. *Int. J. Mod. Phys. Conf. Ser.*, 40:1660021, 2016.

- [68] E. C. Aschenauer, S. Fazio, J. H. Lee, H. Mntysaari, B. S. Page, B. Schenke, T. Ullrich, R. Venugopalan, and P. Zurita. The electron-ion collider: Assessing the energy dependence of key measurements, 2017.

APPENDIX A

ADDITIONAL EMBEDDING PLOTS

This appendix includes additional comparison plots between the 2012 embedding and the 2013 data from Chapter 6.

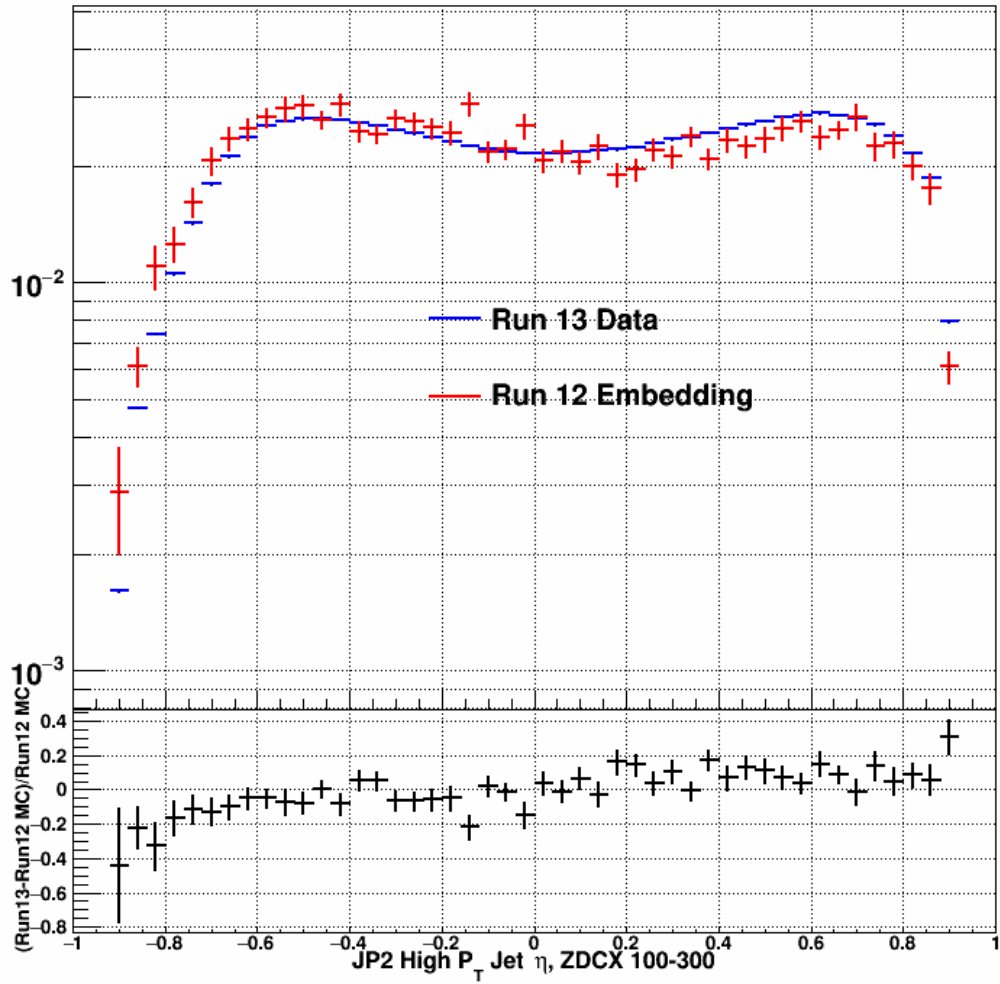


Figure A.1: High p_T jet η distribution for the data (blue) and the embedding (red). The bottom of the plot shows the ratio of (data-embedding)/embedding.

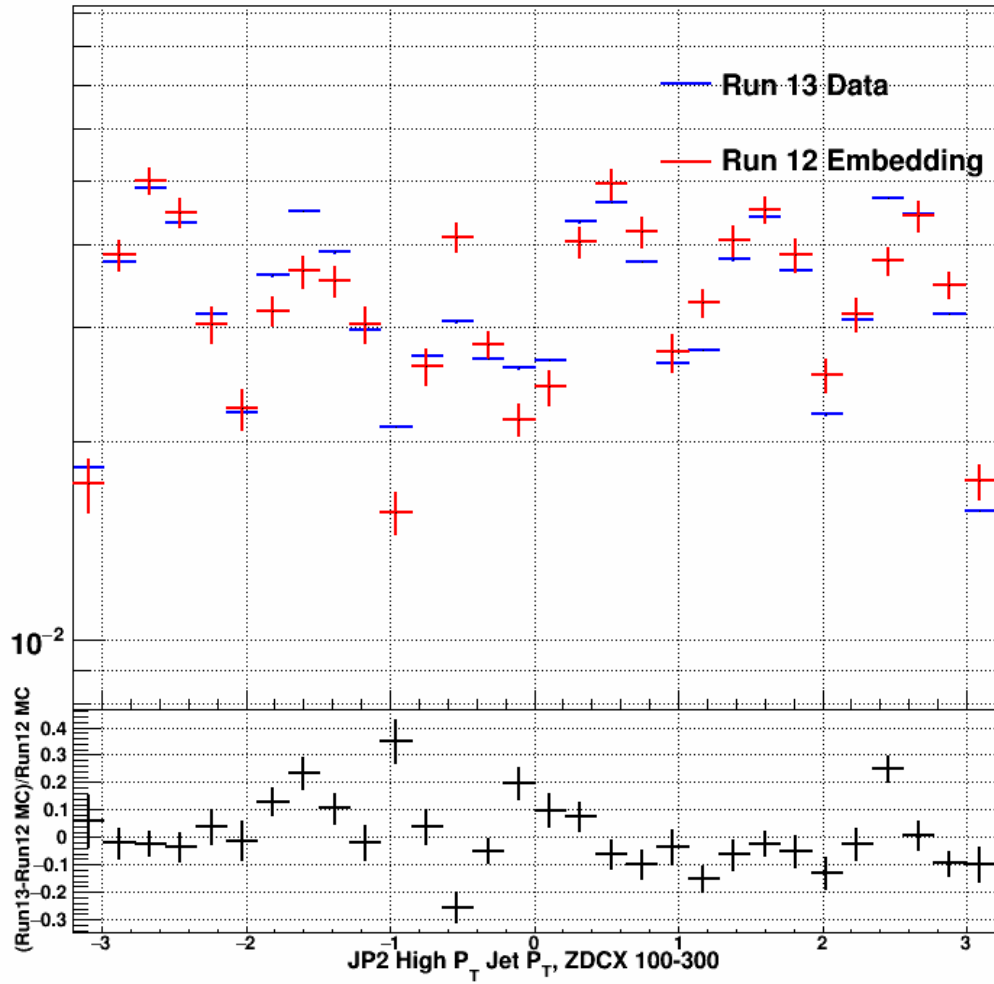


Figure A.2: High p_T jet ϕ distribution for the data (blue) and the embedding (red). The bottom of the plot shows the ratio of (data-embedding)/embedding.

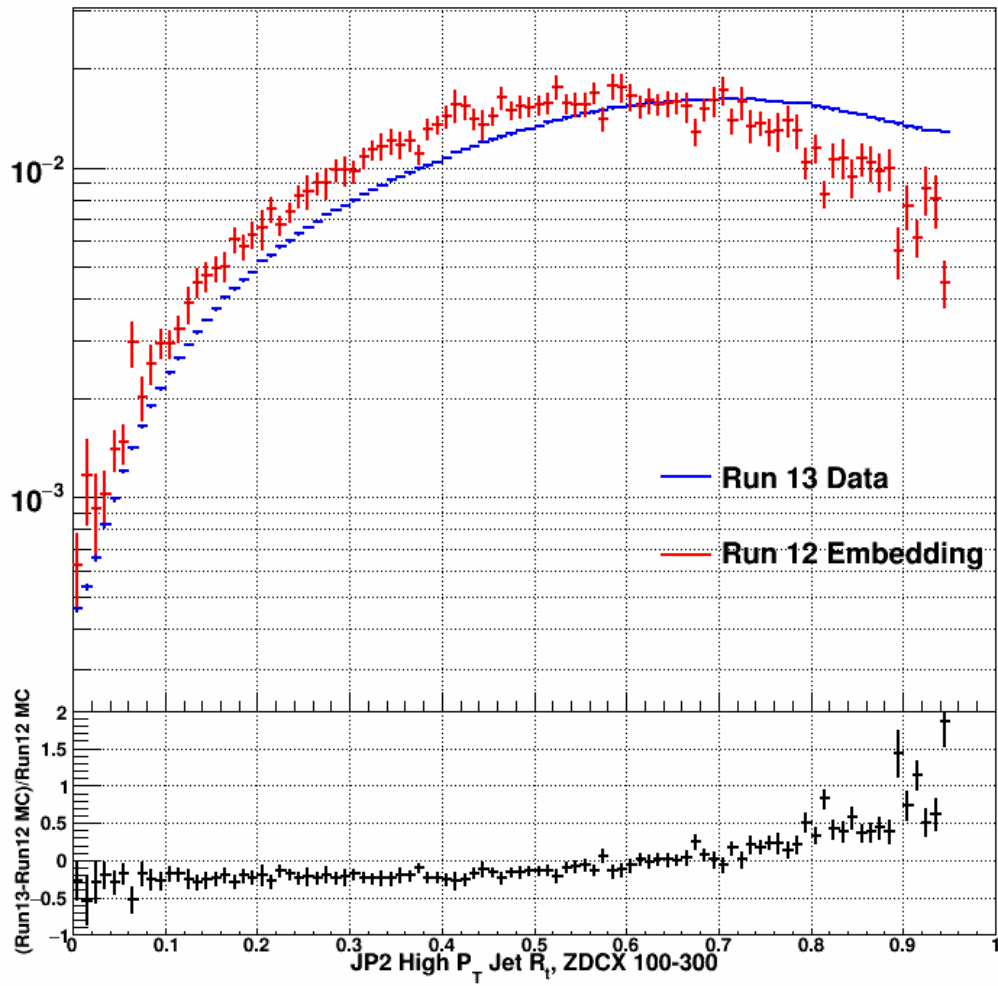


Figure A.3: High p_T jet R_t distribution for the data (blue) and the embedding (red). The bottom of the plot shows the ratio of (data-embedding)/embedding.

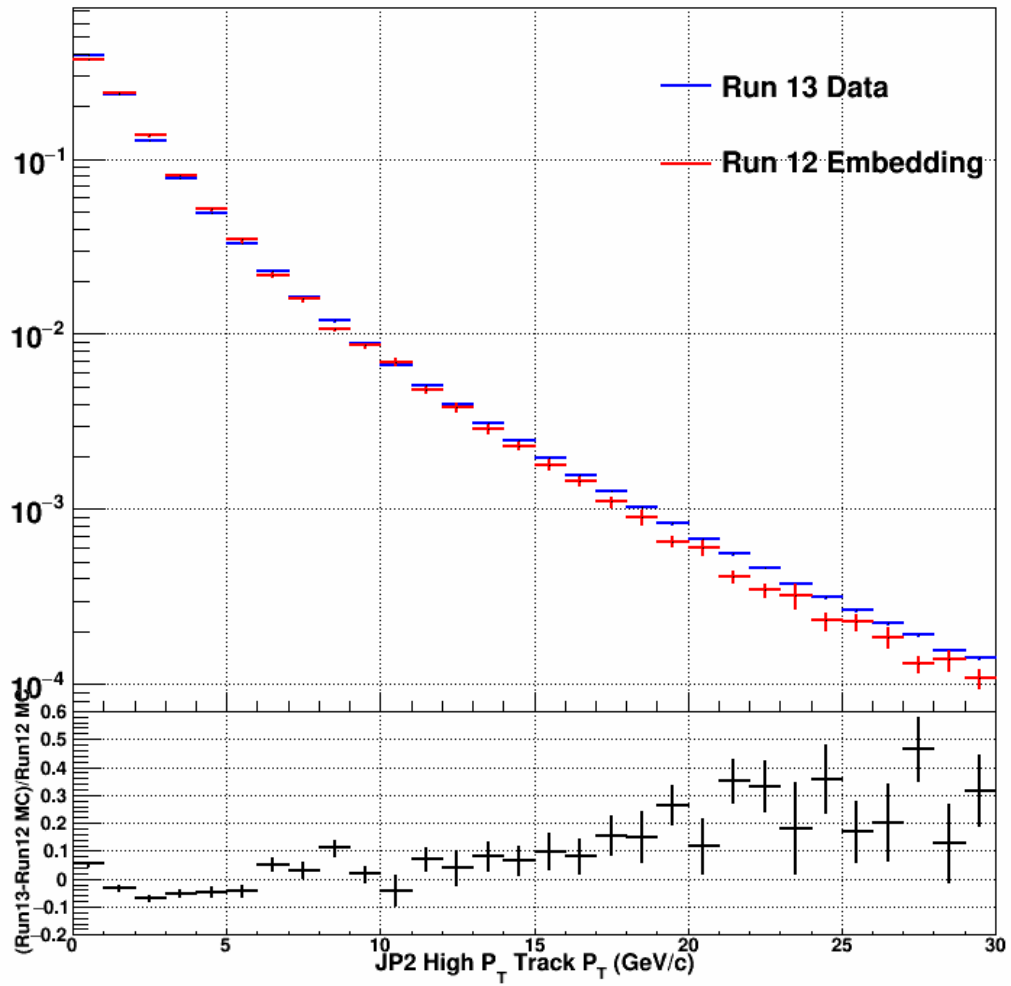


Figure A.4: High p_T jet track p_T distribution for the data (blue) and the embedding (red). The bottom of the plot shows the ratio of (data-embedding)/embedding.

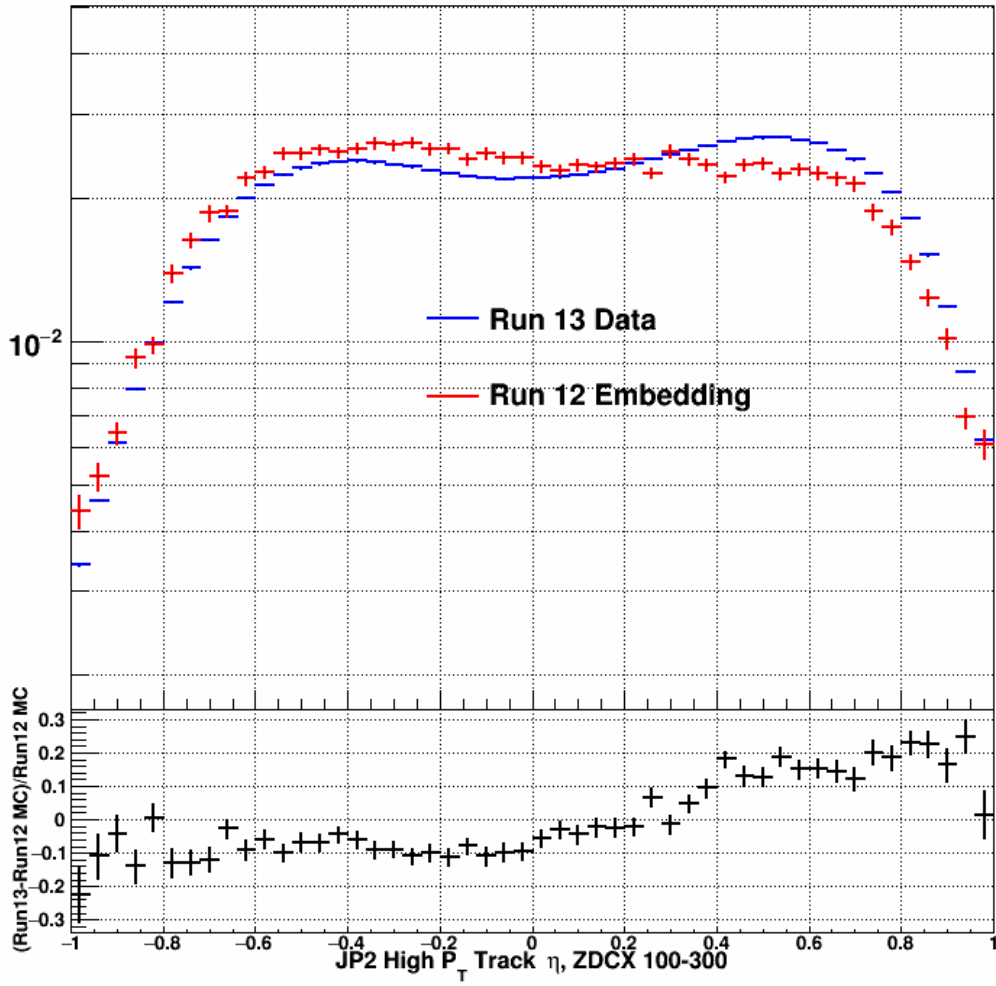


Figure A.5: High p_T jet track η distribution for the data (blue) and the embedding (red). The bottom of the plot shows the ratio of (data-embedding)/embedding.

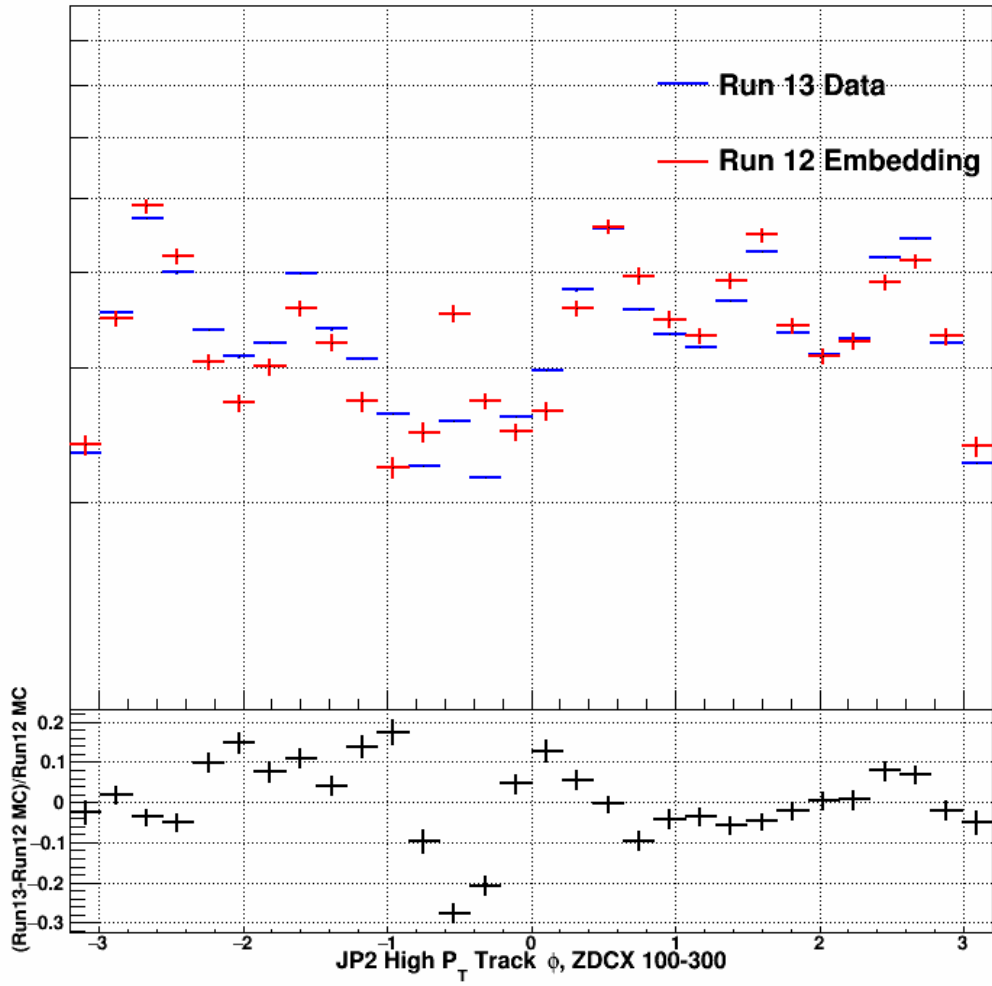


Figure A.6: High p_T jet track ϕ distribution for the data (blue) and the embedding (red). The bottom of the plot shows the ratio of (data-embedding)/embedding.

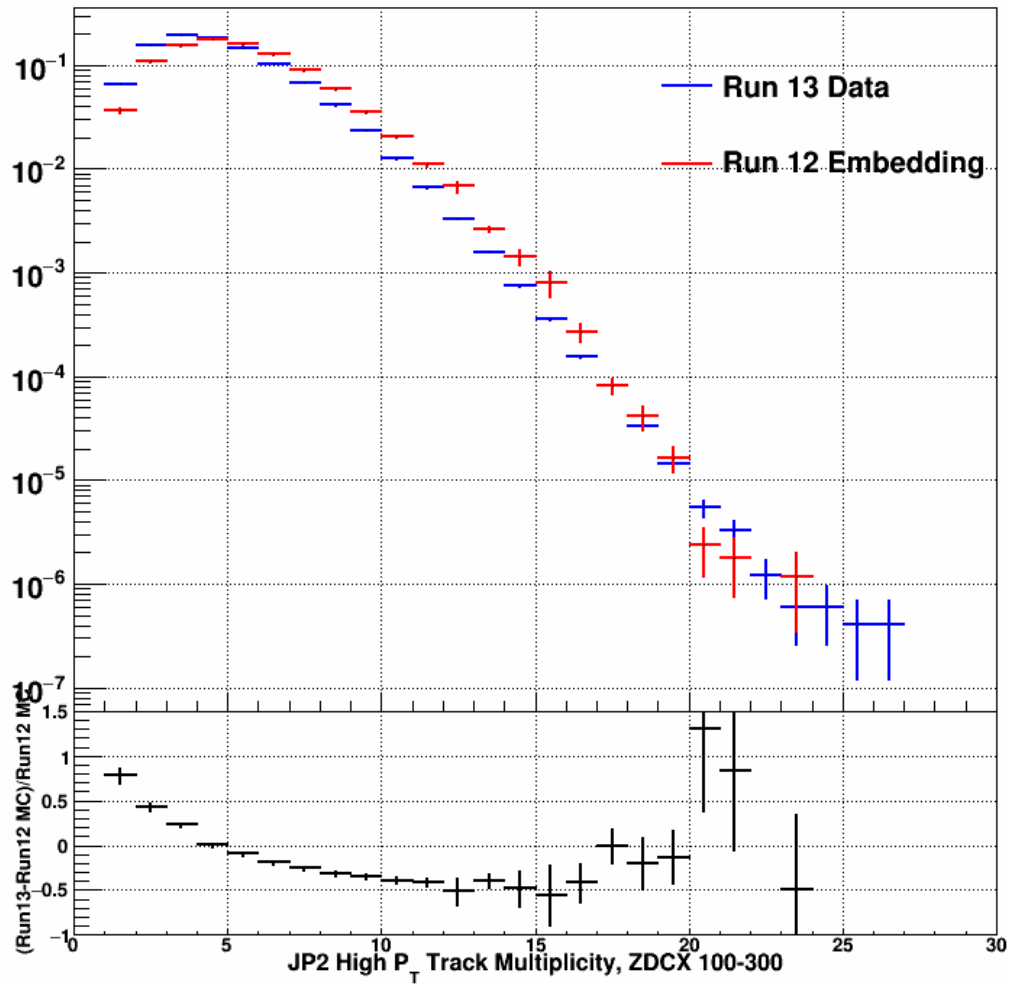


Figure A.7: High p_T jet track multiplicity distribution for the data (blue) and the embedding (red). The bottom of the plot shows the ratio of (data-embedding)/embedding.

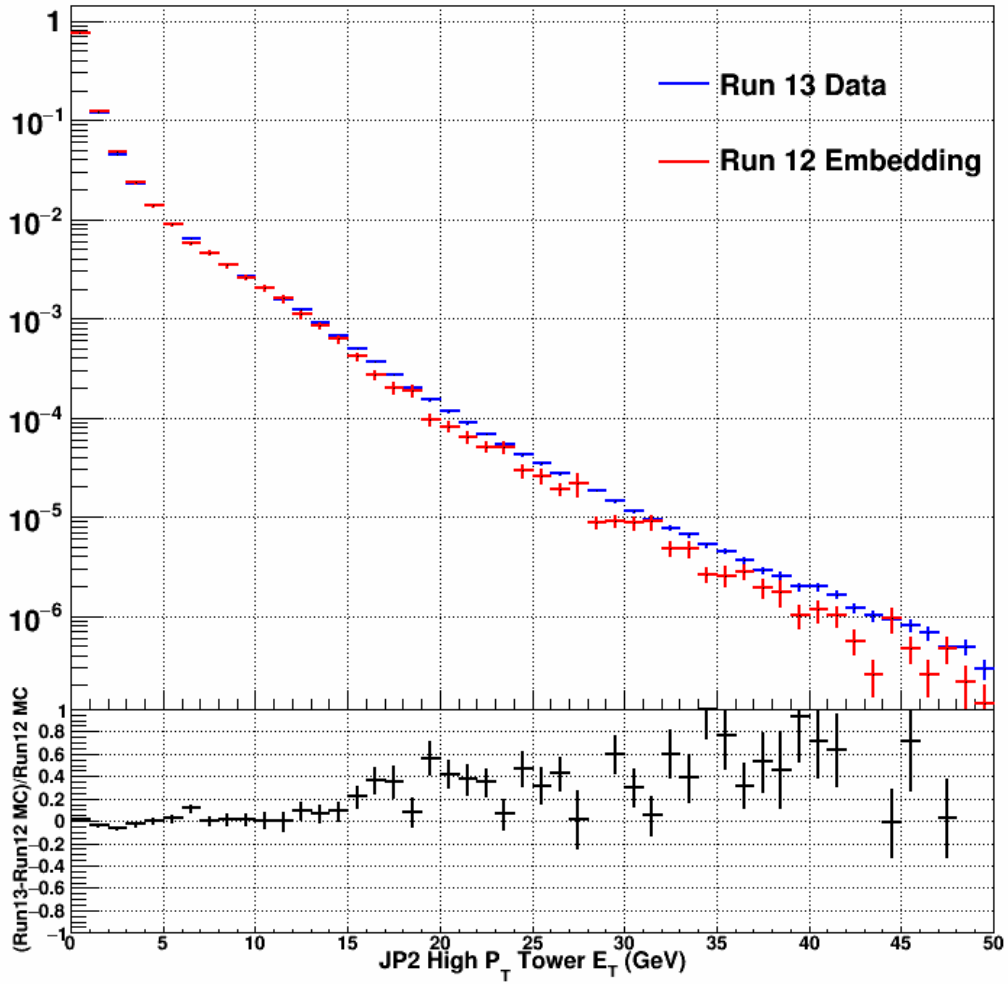


Figure A.8: High p_T jet tower E_T distribution for the data (blue) and the embedding (red). The bottom of the plot shows the ratio of (data-embedding)/embedding.

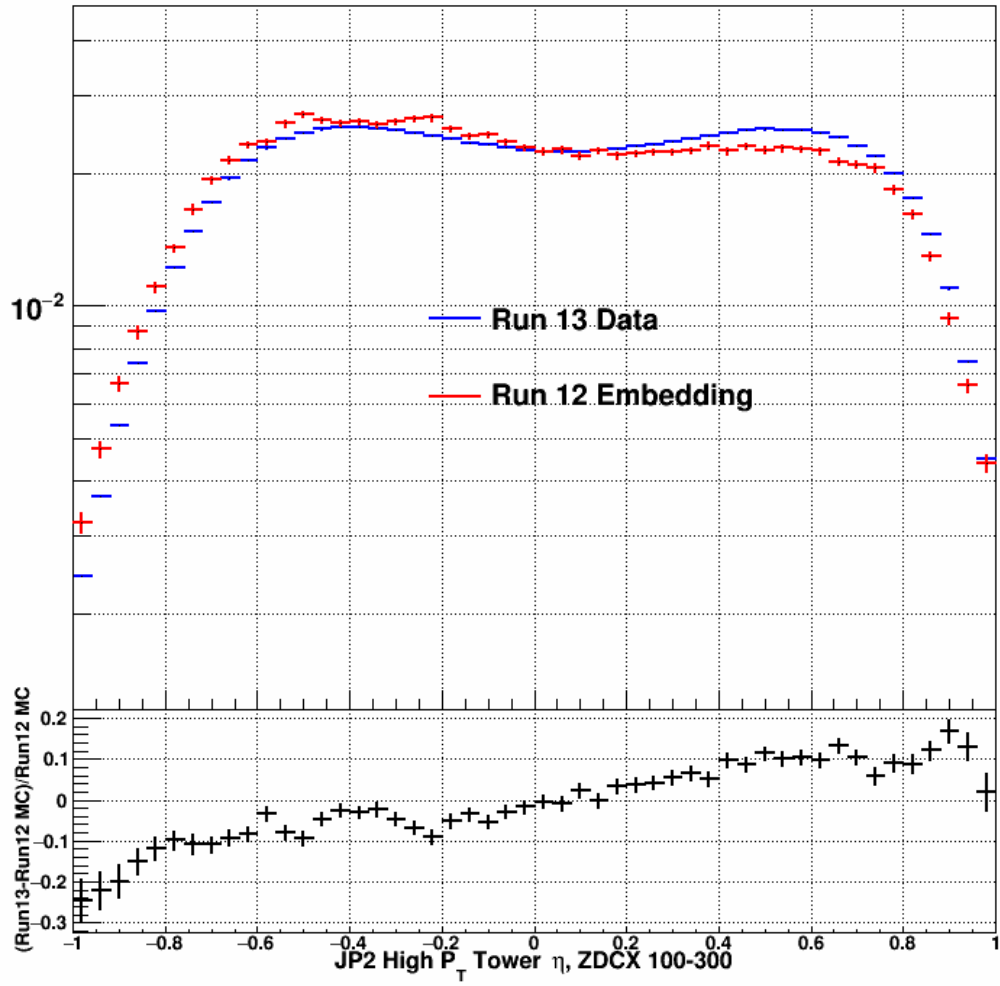


Figure A.9: High p_T jet tower η distribution for the data (blue) and the embedding (red). The bottom of the plot shows the ratio of (data-embedding)/embedding.

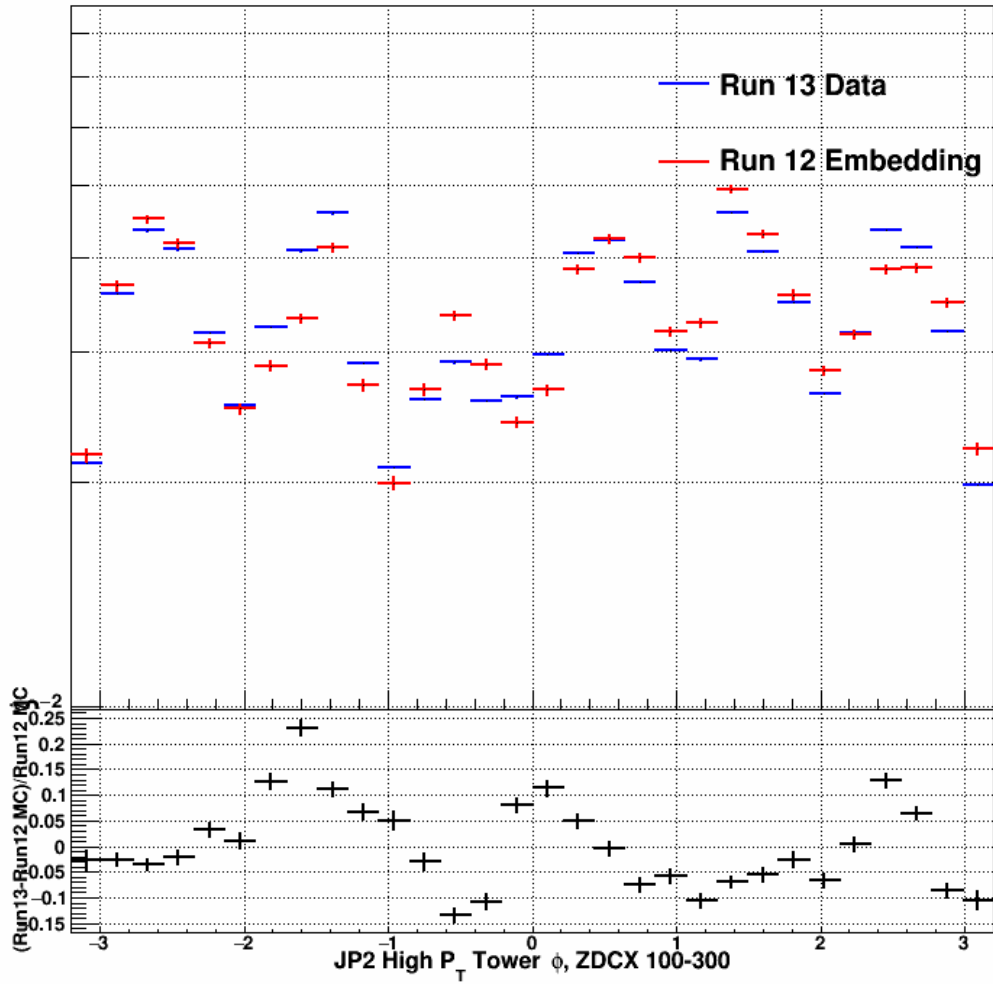


Figure A.10: High p_T jet tower ϕ distribution for the data (blue) and the embedding (red). The bottom of the plot shows the ratio of (data-embedding)/embedding.

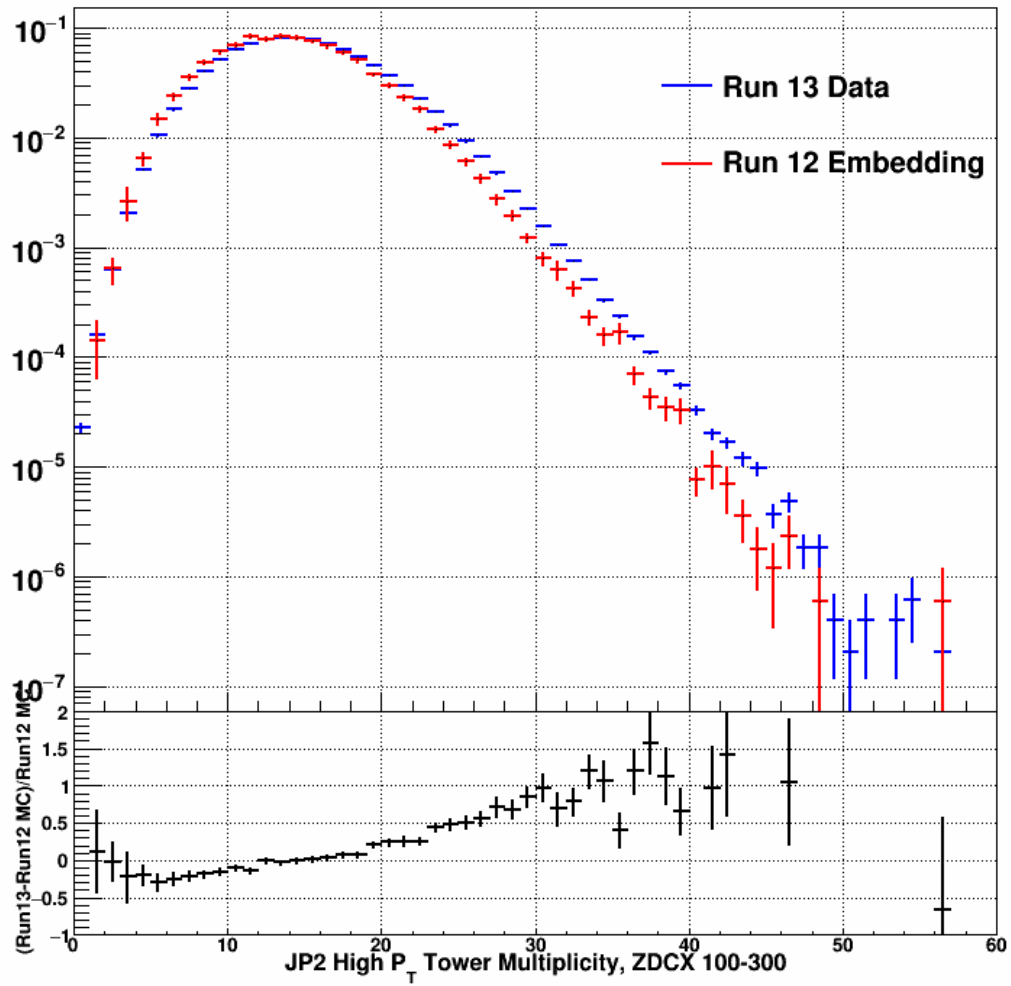


Figure A.11: High p_T jet tower multiplicity distribution for the data (blue) and the embedding (red). The bottom of the plot shows the ratio of (data-embedding)/embedding.

APPENDIX B

INVARIANT MASS DERIVATION

For the dijet double spin asymmetry analysis, the final values were plotted against the invariant mass of the two outgoing particles: $M^2 \equiv (P_3 + P_4)^2 = P_3^2 + P_4^2 + 2P_3 \cdot P_4$. The 4-momentum P_i was expressed in terms of the transverse mass ($m_T = \sqrt{m^2 + p_x^2 + p_y^2}$), rapidity ($y = \frac{1}{2} \ln \left(\frac{E + p_z}{E - p_z} \right)$), and azimuthal angle (ϕ).

$$P_i = \begin{pmatrix} m_{Ti} \cosh y_i \\ p_{Ti} \cos \phi_i \\ p_{Ti} \sin \phi_i \\ m_{Ti} \sinh y_i \end{pmatrix} \quad (\text{B.1})$$

Where i is either 3 or 4 referring to the outgoing particles.

From equation B.1 one can see that $E = m_T \cosh y$, and $p_z = m_T \sinh y$. To obtain the invariant mass it was advantageous to define P^2 .

$$\begin{aligned}
P^2 &= m_T^2 \cosh^2 y - p_T^2 \cos^2 \phi - p_T^2 \sin^2 \phi - m_T^2 \sinh^2 y \\
&= m_T^2 (\cosh^2 y - \sinh^2 y) - p_T^2 (\cos^2 \phi + \sin^2 \phi) \\
&= m^2 + p_T^2 - p_T^2 \\
&= m^2
\end{aligned} \tag{B.2}$$

And $2P_3 \cdot P_4$

$$\begin{aligned}
2P_3 \cdot P_4 &= 2[m_{T3}m_{T4}(\cosh y_3 \cosh y_4 - \sinh y_3 \sinh y_4) - p_{T3}p_{T4}(\cos \phi_3 \cos \phi_4 + \sin \phi_3 \sin \phi_4)] \\
&= 2[m_{T3}m_{T4} \cosh(y_3 - y_4) - p_{T3}p_{T4} \cos(\phi_3 - \phi_4)] \\
&= 2\left[\sqrt{(m_3^2 + p_{T3}^2)}\sqrt{(m_4^2 + p_{T4}^2)} \cosh(y_3 - y_4) - p_{T3}p_{T4} \cos(\phi_3 - \phi_4)\right]
\end{aligned} \tag{B.3}$$

Gathering all the terms together the invariant mass squared could be defined.

$$M^2 = m_3^2 + m_4^2 + 2\left[\sqrt{(m_3^2 + p_{T3}^2)}\sqrt{(m_4^2 + p_{T4}^2)} \cosh(y_3 - y_4) - p_{T3}p_{T4} \cos(\phi_3 - \phi_4)\right] \tag{B.4}$$

Define the 4-momenta of the incoming particles.

$$P_1 = \frac{\sqrt{s}}{2} \begin{pmatrix} x_1 \\ 0 \\ 0 \\ x_1 \end{pmatrix} \quad P_2 = \frac{\sqrt{s}}{2} \begin{pmatrix} x_2 \\ 0 \\ 0 \\ -x_2 \end{pmatrix} \tag{B.5}$$

The 2-body system had momentum $q \equiv P_1 + P_2$.

$$q = \frac{\sqrt{s}}{2} \begin{pmatrix} x_1 + x_2 \\ 0 \\ 0 \\ x_1 - x_2 \end{pmatrix} \quad (\text{B.6})$$

The invariant mass was simply the square root of the momentum.

$$\begin{aligned} M \equiv \sqrt{q^2} &= \sqrt{\frac{s}{4} [(x_1 + x_2)^2 - (x_1 - x_2)^2]} \\ &= \sqrt{s} \sqrt{x_1 x_2} \end{aligned} \quad (\text{B.7})$$

APPENDIX C

2012 EMBEDDING RUN LIST

13077067 13077068 13077073 13077075 13077076 13077078 13077081 13078011 13078012
13078014 13078035 13078036 13078039 13078040 13078042 13078045 13078050 13078051
13078052 13078054 13078055 13078057 13078058 13078063 13078070 13079038 13079073
13079074 13079075 13079076 13079077 13079079 13080001 13080002 13080003 13080004
13080005 13080011 13080013 13080014 13080015 13080090 13080091 13080092 13080093
13080094 13080095 13080096 13080097 13080098 13080099 13081001 13081004 13081005
13081007 13082001 13082003 13082004 13082005 13082006 13082007 13082008 13082009
13082010 13082011 13083068 13083070 13083073 13083074 13083076 13083081 13083082
13083084 13084001 13084007 13084008 13084024 13084027 13084028 13084032 13084034
13084035 13084036 13084037 13084038 13084039 13084040 13084041 13085004 13085005
13085006 13085008 13085009 13085010 13085011 13085030 13085033 13085047 13086070
13086071 13086072 13086073 13086078 13086079 13086080 13086081 13086082 13086083
13086085 13086087 13086088 13087012 13087013 13090021 13090022 13090023 13090037
13090038 13090040 13090043 13090048 13090049 13091005 13091009 13091011 13091024
13091025 13091027 13091033 13091034 13091035 13091036 13091037 13091038 13091041
13091042 13091043 13091044 13091045 13092006 13092007 13092008 13092044 13092045
13092046 13093018 13093020 13093023 13093024 13093029 13093030 13093034 13093035

13093036 13093037 13093038 13093046 13094001 13094003 13094004 13094005 13094007
13094008 13094009 13094011 13094013 13094014 13094015 13094016 13094017 13094018
13094045 13094050 13094052 13094054 13094089 13095001 13095002 13095003 13095004
13095008 13095009 13095012 13095013 13095014 13095015 13095016 13095017 13095049
13096001 13096002 13096003 13096004 13096005 13096006 13096062 13096063 13096064
13096065 13096066 13096069 13096070 13097001 13097002 13097003 13097004 13097005
13097006 13097007 13097023 13097024 13097026 13097027 13097028 13097029 13097032
13097033 13097034 13097035 13097036 13097037 13097038 13097039 13100004 13100005
13100006 13100008 13100010 13100011 13100012 13100013 13100014 13100015 13100027
13100029 13100030 13100031 13100032 13100033 13100034 13100035 13100037 13100038
13100040 13100042 13100054 13100055 13100056 13100057 13100059 13100060 13101001
13101002 13101003 13101004 13101005 13101006 13101007 13101013 13101015 13101021
13101024 13101026 13101027 13101040 13101041 13101042 13101043 13101044 13101045
13101046 13101047 13101048 13101049 13101050 13103011 13103013 13103014 13103015
13103016 13103017 13104003 13104004 13104008 13104011 13104012 13104013 13104014
13104019 13104044 13104054 13104056 13104057 13104058 13104059 13104060 13104061
13104062 13105006 13105007 13105008 13105009 13105010 13105011 13105012 13105014
13105015 13105016 13105017 13105018 13105022 13105040 13105041 13106064 13106069
13106071 13106072 13106073 13106074 13106075 13106076 13107001 13107002 13107003
13107017 13107019 13107024 13107025 13107026 13107027 13107028 13107029 13107030
13107032 13107033 13107059 13107060 13107062 13108001 13108008 13108009 13108011
13108012 13108013 13108026 13108028 13108029 13108031 13108033 13108040 13108050
13108079 13109015 13109016 13109025 13109026 13109027

APPENDIX D

2013 RUN LIST

14081005 14081006 14081007 14081009 14081010 14081013 14082029 14082030 14082031
14082033 14082034 14082037 14083005 14083006 14083007 14083008 14083009 14083019
14083020 14083021 14083022 14083036 14083038 14083039 14083041 14083043 14083044
14083045 14083047 14083051 14083055 14083056 14083057 14084005 14084008 14084009
14084010 14084013 14084014 14084018 14084019 14084020 14084021 14084057 14084058
14084059 14084061 14084062 14085006 14085007 14085008 14085009 14085012 14085016
14085017 14085018 14085019 14085022 14085023 14085024 14085034 14085035 14086013
14086016 14086018 14086019 14086020 14086022 14087022 14087024 14087033 14087035
14087036 14087037 14088007 14088009 14088010 14088027 14088105 14088108 14088140
14088141 14088142 14089001 14089002 14089003 14089004 14089008 14089010 14089011
14089012 14089014 14089015 14089034 14089035 14089036 14089037 14089044 14090005
14090006 14090007 14090008 14090013 14090040 14090041 14090042 14090045 14090046
14090047 14090049 14090050 14090051 14090052 14090053 14091003 14091004 14091005
14091006 14091008 14091013 14091020 14091021 14091022 14091023 14091026 14091027
14091028 14091029 14091030 14091033 14091034 14092002 14092004 14092005 14092010
14092011 14092015 14092024 14092030 14092057 14092058 14092061 14092062 14092063
14092065 14092067 14092068 14092071 14092091 14092092 14092093 14092097 14092098

14092099 14092100 14092101 14092104 14092105 14092106 14092107 14092108 14092109
14092110 14093001 14093005 14093006 14093007 14093008 14093009 14093010 14093013
14093014 14093015 14093016 14093017 14093018 14093019 14093020 14093021 14094005
14094006 14094007 14094008 14094020 14094022 14094024 14095019 14095020 14095022
14095023 14095024 14095025 14095027 14095029 14096010 14096011 14096013 14096014
14096077 14096078 14096082 14096083 14096085 14096098 14096099 14096100 14096101
14096102 14096104 14096105 14096106 14096108 14097006 14097018 14097019 14097020
14097021 14097022 14097023 14097026 14097028 14097030 14097033 14097036 14097037
14097038 14097039 14097065 14097066 14097067 14097068 14097070 14098004 14098015
14098016 14098017 14098026 14098027 14098028 14098029 14098031 14098032 14098033
14098039 14098046 14098047 14099013 14099014 14099015 14099016 14099017 14099018
14099020 14099024 14099025 14099027 14099029 14099030 14099031 14099032 14099033
14099090 14100018 14100021 14100022 14101061 14101062 14101063 14101064 14101065
14101066 14101067 14101068 14102034 14102035 14102036 14102037 14102041 14102042
14102043 14104025 14104026 14104052 14104053 14105002 14105006 14105007 14105008
14105009 14105011 14105013 14105014 14105015 14105016 14105031 14105032 14105033
14105034 14105036 14105037 14105038 14105039 14106036 14106037 14106041 14106042
14106043 14108007 14108013 14108014 14108015 14108017 14108019 14108078 14108080
14108081 14108083 14108084 14108085 14108091 14108092 14108093 14108095 14108096
14108097 14110024 14110053 14110054 14110055 14110056 14110058 14110059 14110060
14110061 14110062 14110064 14110065 14111038 14111058 14111060 14111062 14111063
14111064 14111066 14111067 14111070 14111071 14112001 14112035 14112038 14112040
14112041 14112042 14112044 14113010 14113011 14113012 14113015 14113016 14113017
14113018 14113019 14113076 14113078 14114007 14114008 14114011 14114012 14114013
14114014 14114015 14114016 14114018 14114019 14115015 14115017 14115018 14115019
14115020 14115022 14115023 14115024 14115075 14116001 14116002 14116014 14116015
14116016 14116019 14116020 14116057 14116059 14116060 14116065 14117002 14117024

14117025 14117026 14117027 14117028 14117064 14117069 14118033 14118034 14118035
14118064 14119022 14119024 14119026 14119027 14120018 14120019 14120025 14120026
14122021 14122024 14122025 14123035 14123037 14123038 14123039 14123040 14123060
14123061 14124016 14124017 14124018 14124019 14124030 14124033 14124034 14124035
14124036 14124037 14124038 14126013 14126014 14126015